DISLOCATION-PIPE DIFFUSION IN SODIUM CHLORIDE

By

YUEN KIT HO

A thesis submitted for the degree of

Doctor of Philosophy

of the University of London

Department of Metallurgy and Materials Science,

Imperial College of Science and Technology,

London, SW7 2BP.

November, 1981

ABSTRACT

The transport properties of NaCl single crystals have been investigated using material with a cation impurity content ∿1 ppm. The dislocation density of the specimens used was 10^3 - 10^4 cm^{-2}.

The conductivity has been measured over the temperature range 356 - 638°C, and has revealed the interesting feature of stages II' and II in the extrinsic region, with corresponding activation energies of 1.25 eV and 0.71 eV, respectively. Evidence has been obtained which suggests that stage II is a combination of lattice and dislocation contributions. A theoretical estimation has suggested that stage II' is masked when specimens have a dislocation density ≥ 2 x 10^4 cm^{-2}.

Tracer diffusion has been carried out over the temperature range 374 - 505°C. The general expression for the process is represented as

$$D = 1.77 \times 10^{-3} \exp\left[-\frac{1.25 \pm 0.02}{kT}\right] \quad cm^2\ sec^{-1}$$

"Tails" in the diffusion profiles have been identified as an isolated-dislocation diffusion effect. The enhanced diffusion in these dislocation paths is represented as

$$a^2 D_d = 5.35 \times 10^{-2} \exp\left[-\frac{0.57 \pm 0.04}{kT}\right] \quad cm^4\ sec^{-1}$$

The mechanism for the fast transport of tracer in the dislocation paths is by jumping of the tracer into the excess cation vacancies in the space-charge cloud which surrounds dislocation-pipes. The radius of the space-charge cloud has been calculated as ∿260Å.

ACKNOWLEDGEMENTS

I wish to acknowledge gratefully the guidance and help received from my supervisor, Professor P.L. Pratt throughout the progress of this work, and express my gratitude to Professor A.D. LeClaire from Harwell for the many helpful discussions that he has contributed.

I am also indebted to Mr. H. Haddow and Mr. L. Dutton for their technical assistance, and Dr. B. Dalgleish for the compilation of this thesis.

Finally, I would like to thank Harwell for the financial support of this project.

CONTENTS

	Page
Abstract	2
Acknowledgements	3
Contents	4
List of tables	7
List of Figures	8
Chapter One: Introduction .	11
Chapter Two: Crystal Structure and Atomic Migration.	13
2.1. Structure of sodium chloride	14
2.1.1. Perfect crystal lattice	14
2.1.2. Point defects	17
2.1.3. Line defects	17
2.1.4. Planar defects	20
2.2. Basic concepts of atomic migration	21
2.3. Concentration of vacancies	23
2.4. Theoretical calculation of diffusion coefficient	28
Chapter Three: Review of Previous Literature.	33
3.1. Solutions of grain boundary diffusion	34
3.2. Solutions of isolated dislocation diffusion	44
3.3. Results of dislocation enhanced diffusion	61
Chapter Four: Experimental Techniques.	67
4.1. Crystal growth	68
4.1.1. Purification of starting material	68
4.1.2. Growth of crystals	69
4.2. Bending and polygonisation	72
4.2.1. Preparation of specimens	72
4.2.2. Four-point bending	73

Page

4.2.3. Polygonisation of bent specimens 77

4.3. Chemical etching and dislocation density counting 79

4.4. Radiation works 80

4.4.1. Use of tracer 80

4.4.2. Vacuum evaporation of tracer 81

4.4.3. Diffusion annealing 85

4.4.4. Use of scintillator and radiation counter 86

4.5. Microtome sectioning 87

4.6. Determination of section thickness by weighing 94

Chapter Five: Results and Discussion. 96

5.1. Precision and limits of the sectioning technique 97

5.2. Cleavage damage and dislocation-etch pit 99

5.3. Bending and polygonisation 103

5.4. Analysis of the chemical contents of specimens 114

5.4.1. Spectroscopic determination of divalent cation and hydroxyl anion impurity contents 114

5.4.2. Determination of divalent cation impurity contents using the conductivity technique 115

5.5. Diffusion and conductivity 118

5.5.1. Lattice diffusion 124

5.5.2. Isolated-dislocation diffusion 132

5.5.3. Space-charge effects on dislocation diffusion 139

5.5.4. Comparison of conductivity and diffusion results with previous literature 144

Chapter Six: Conclusions and Suggestions for Further Work. 164

References 168

Appendix I: Theoretical calculation of efficiency of vacuum evaporation technique in relation to geometry of source and specimen. 182

Page

Appendix II: Calibration of radioactivity counting efficiency. 182

Appendix III: Calibration of microtoming. 184

Appendix IV: Determination of tracer layer thickness on specimen surface. 186

Appendix V: Conductivity data. 188

Appendix VI: Diffusion data. 189

LIST OF TABLES

Table No.		Page
I	Theoretical weighing errors in percentage in relation to the area and thickness of the specimen section.	95
II	Spectroscopic analysis of calcium and magnesium impurity contents in sodium chloride specimens of Run 1 - 5.	114
III	Values of the parameters calculated from the diffusion profiles at different temperatures.	135
IV	Values of degree of association, p, and radius of the space-charge cloud, a, at different temperatures.	143
V	Enthalpy of migration of cation vacancy in NaCl measured from conductivity.	145
VI	Values of D_o and H_m measured from the extrinsic region of self-diffusion of NaCl.	146
VII	Values of the different parameters in Hart's equation of the present work.	150
VIII	Measured and calculated values of $\log(\sigma T)$ at different temperatures.	151
IX	Values of the Haven ratio of dislocations contribution to conductivity at different temperatures.	152
X	Comparison of the lattice and dislocation diffusion parameters of NaCl crystal.	161

LIST OF FIGURES

Figure No.		Page
2.1.	Unit cell of sodium chloride.	15
2.2.	Direct interchange mechanism for self-diffusion.	16
2.3.	Four-ring mechanism for self-diffusion.	16
2.4.	Point defects in ionic crystal.	18
2.5.	Edge dislocation in sodium chloride crystal.	19
2.6.	Vacancy migration in sodium chloride crystal.	22
2.7.	Motion of a positive ion interstitial in the sodium chloride structure.	24
2.8.	Interstitialcy jumps in ionic crystal.	25
3.1.	Coordinate system for diffusion outside a semi-infinite slab of high diffusivity material imbedded in a semi-infinite solid.	35
3.2.	Concentration contours in a solid having a single grain boundary.	40
3.3.	Comparison of Fisher's, Whipple's and Suzuoka's solution to grain boundary diffusion.	40
3.4.	Slope of Ln $\bar{c} \sim \eta\beta^{-\frac{1}{2}}$ and ln $\bar{c} \sim (\eta\beta^{-\frac{1}{2}})^{6/5}$ plots.	43
3.5.	Relative concentration in the grain boundary as a function of $\eta\beta^{-\frac{1}{2}}$.	45
3.6.	Concentration contour resulting from diffusion down and out from a dislocation-pipe.	49
3.7.	Plot of log Q^{I} versus η.	54
3.8.	Plot of log Q^{II} versus η.	55
3.9.	The quantity A of Eqn. 3.35 plotted as a function of α for various $\alpha\beta$.	57
3.10.	Plot of log Q^{I}_{ex} versus α.	58
3.11.	Plot of log Q^{II}_{ex} versus α.	59

Figure No.		Page
4.1.	Crystal growing apparatus.	70
4.2.	Schematic diagram of the crystal growing apparatus.	71
4.3.	Schematic diagram of a beam undergoing four-point bending.	74
4.4.	Typical applied load versus displacement curve of four-point bending of NaCl crystal.	76
4.5.	Recovery behaviour of bent crystal.	78
4.6.	Edward-306 vacuum coater.	82
4.7.	Close up view of the radioactive tracer evaporating unit.	84
4.8.	Relative positions of the microtome and auto-collimator.	85
4.9.	Close up view of the sectioning unit of the microtome.	89
4.10.	Schematic drawing of microtome.	90
4.11.	Microtome calibration plot.	92
5.1.	Surface of a well annealed NaCl specimen.	100
5.2.	Surface of a freshly cleaved NaCl specimen.	100
5.3.(a)-(c)	Etched-surface of a NaCl specimen showing the damage of successive cleaving.	101
5.4.	Etched {100} surface of NaCl specimen loaded to 0.3% strain and polygonised at 650°C for 1 hour.	106
5.5.	Same as Fig. 5.4. but ε = 0.2%, T = 600°C and t = 2 hours.	106
5.6.	Same as Fig. 5.4. but ε = 0.2%, T = 650°C and t = 2 hours.	108
5.7.	Same as Fig. 5.4. but ε = 0.1%, T = 650°C and t = 2 hours.	108
5.8.	Same as Fig. 5.4. but ε = 0.1%, T = 700°C and t = 2 hours.	110
5.9.	Same as Fig. 5.4. but ε = 0.05%, T = 700°C and t = 2 hours.	110

Figure No.		Page
5.10.(a)-(c)	Etched-surface of different areas of a non-deformed NaCl specimen.	112
5.11.	Arrhenius conductivity plot of a pure NaCl crystal.	117
5.12.	Diffusion profile of Run 1.	119
5.13.	Diffusion profile of Run 2.	120
5.14.	Diffusion profile of Run 3.	121
5.15.	Diffusion profile of Run 4.	122
5.16.	Diffusion profile of Run 5.	123
5.17.	Lattice diffusion profile of Run 1.	125
5.18.	Lattice diffusion profile of Run 2.	126
5.19.	Lattice diffusion profile of Run 3.	127
5.20.	Lattice diffusion profile of Run 4.	128
5.21.	Lattice diffusion profile of Run 5.	129
5.22.	Arrhenius lattice diffusion plot of NaCl crystal.	131
5.23.	Arrhenius dislocation diffusion plot of NaCl crystal.	137
5.24.	Comparison of the diffusion profiles of Run 4 and 5.	138
5.25.	Logarithmic plot of concentration of cation vacancies versus 1/kT.	140
5.26.	Observation of isoelectric temperature in NaCl crystals with free cation vacancy concentration.	140
5.27.	Lattice and dislocation contribution to conductivity.	153
5.28.	Theoretical estimation of the dislocation contribution to conductivity as a function of dislocation density.	156

CHAPTER ONE

INTRODUCTION

The existence of dislocation enhanced diffusion in metals has long been established beyond doubt. However, in the past years many controversial reports have been made about such fast diffusion properties in alkali halide crystals. It must be recognised that the mass transport mechanism in alkali halides will differ from that in metals owing to the presence of factors peculiar to the ionic lattice: electrically charged defects and the marked influence of trace divalent impurity ions at low temperatures. The contribution of pipe diffusion to total matter transport is usually inferred from experimental data by adopting the idealised low-angle model which regards a tilt boundary as an array of equally spaced edge dislocations. It is the aim of this work to employ a solution for dislocation-pipe diffusion for the investigation of such enhanced diffusion behaviour using high purity sodium chloride single crystal.

A four-point bending technique will be used to introduce a desired amount of strain into the crystal, and polygonised so as to give a stable microstructure which will not change in the subsequent diffusion anneal. The inter-dislocation distance of the polygonised boundaries will be measured from the micrographs of the chemically etched specimens. In order to ensure that the dislocations are isolated and independent in their diffusion behaviour, the non-deformed single crystals, which have a much wider inter-dislocation spacing, might be used in the eventual diffusion annealing. The relationship between diffusion time and the gradient of the 'tail' in the diffusion profile will be investigated to confirm that any enhanced diffusion is a consequence of the presence of isolated dislocations rather than overlapping dislocations.

Diffusion studies shall be carried out in the extrinsic temperature range of 374°C - 505°C. This will be incorporated with conductivity measurement in the hope of identifying the transport mechanisms in the crystal.

CHAPTER TWO

CRYSTAL STRUCTURE AND ATOMIC MIGRATION

2.1. Structure of Sodium Chloride

2.1.1. Perfect crystal lattice

The sodium chloride structure consists of two interpenetrating face centred cubic lattices, the one being composed of the sodium ions, and the other of the chloride ions. The unit cell for the perfect lattice is shown on Figure 2.1. The bonding in alkali halides is almost entirely ionic, which results in a strong electrostatic attraction between anions and cations. The transport of matter is associated with the transport of charge arising from the charged nature of the diffusing species. The large gap between the energies of the valence and conductance bands precludes any major contribution to charge transport from electron motion.

In the perfect lattice the transport of mass could occur if two adjacent ions exchanged places, as shown in Figure 2.2. However, to do this a considerable dilation of the lattice would be required, and the ions would need to be squeezed past each other through a position of very high electrostatic repulsion. Furthermore, the exchange can occur only between species of the same polarity, as the repulsive forces prohibit an exchange into the sublattice of the opposite charge. Thus atomic migration in ionic crystals via the direct exchange mechanism is unfavourable because of the activation energy and the close-packed nature of the crystal structure. The ring mechanism is an alternative which is sometimes employed to describe the self-diffusion of a metal, e.g. sodium, suffers from the low probability of a cooperative action in which all members of the ring move at once, as shown in Figure 2.3. The transport of ions in sodium chloride can be explained clearly in terms of ions moving in a defect structure, which requires the movement of the defects themselves. The different types of defects present in the lattice will be briefly described in the following sections.

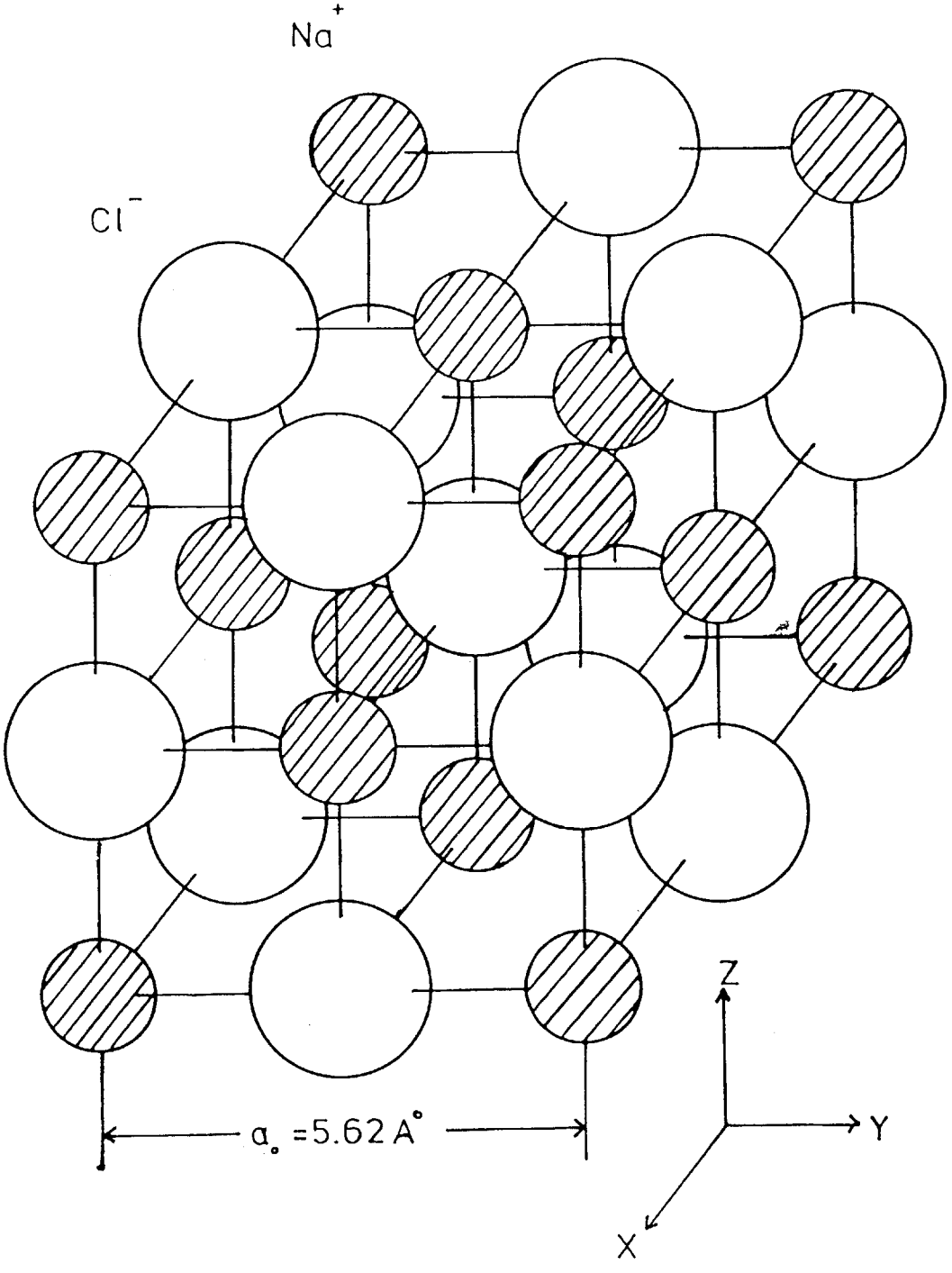


Fig. 2.1. Unit cell of sodium chloride.

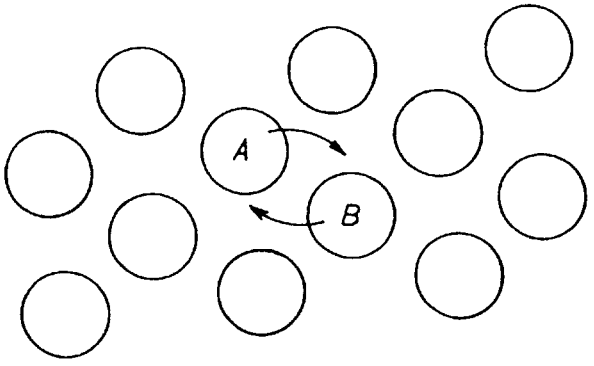


Fig.2.2. Direct interchange mechanism for self-diffusion.

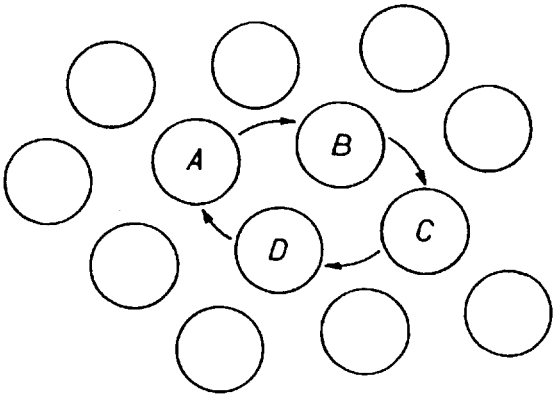


Fig.2.3. Four-ring mechanism for self-diffusion.

2.1.2. Point defects

There are two types of point defects. The first type, the Frenkel defect, consists of a vacancy on a lattice site associated with an interstitial ion. The second type, the Schottky defect, consists of a separated pair of anion and cation vacancies. These defects are shown in Figure 2.4. At equilibrium, a fraction of these vacancies, of opposite sign, combine to form divacancies. Larger vacancy aggregates, are fairly immobile and are considered unimportant in the unit diffusion process. A divacancy is electrically neutral and may be thought of as a degenerate type of Schottky defect, which contributes to transfer of mass but not charge. In sodium chloride, the Schottky defect predominates over the Frenkel defect due to its lower formation energy. The concentration of vacancies in an alkali halide crystal will be dealt with in subsequent sections.

2.1.3. Line defects

Dislocations in ionic crystals, edge and screw types, are classed as line defects which perturb the regular pattern of positive and negative ions and may themselves be charged due to the ionic nature of the material. An edge dislocation in an ionic crystal of the NaCl type is shown in Figure 2.5. The plane shown is a (100) plane and the electrical charges alternate on successive (100) planes. The slip plane is a $(0\bar{1}1)$ plane with a slip direction $\langle 011 \rangle$. The dislocations are formed by insertion of the two extra atomic half-planes enclosed by dotted lines. Beyond the edges of these half-planes there is an expansion of the lattice. The stress in this region may be relieved by the presence of interstitial ions or vacancies, which have a positive volume change associated with them. Thus, the creation of such point defects in this region requires a lower activation energy. The activation energy for mobility along the dislocation is also lowered due to the dilation of the lattice.

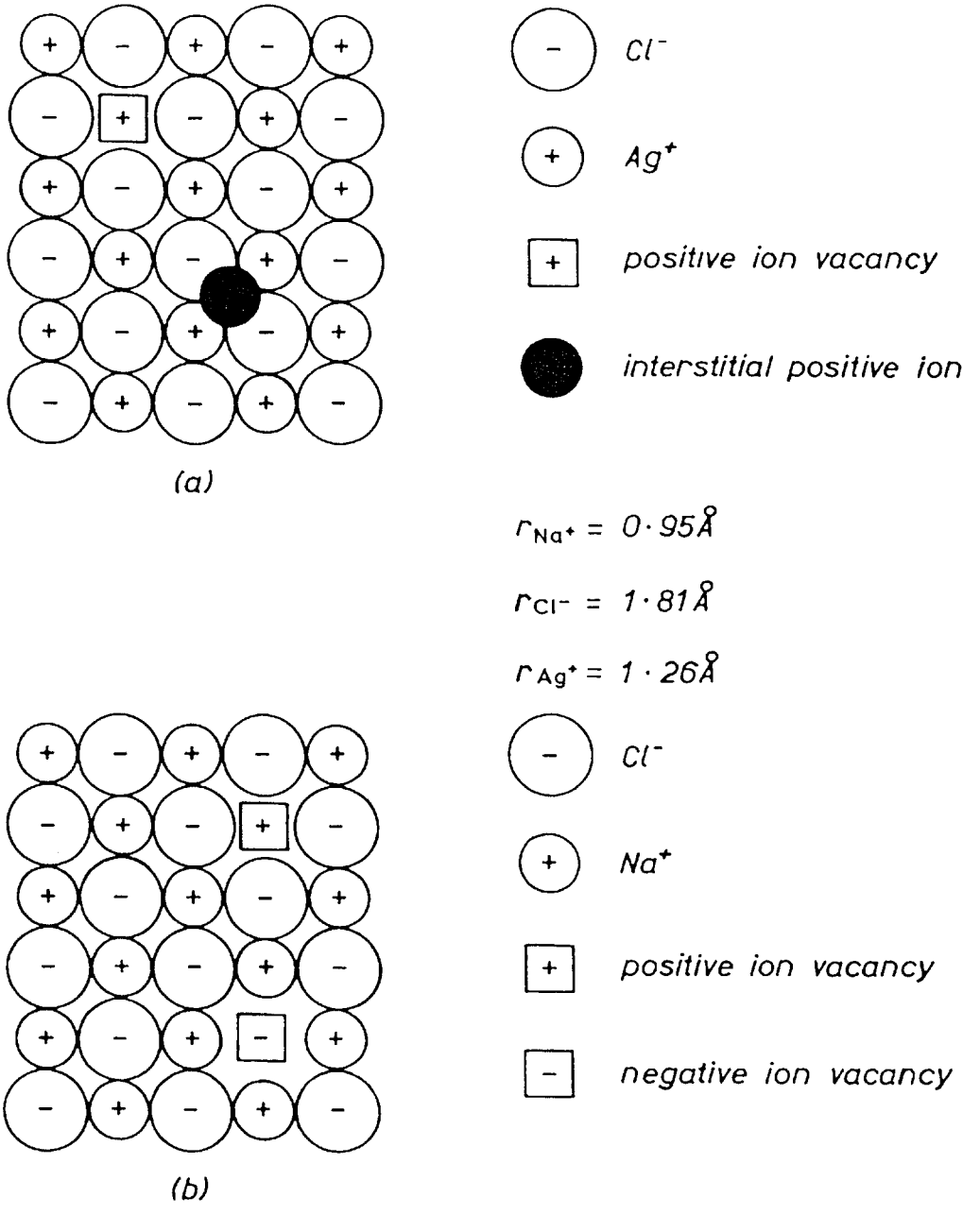


Fig. 2.4. Defects in ionic crystals: (a) Frenkel defect in silver chloride, (b) Schottky defect in sodium chloride.

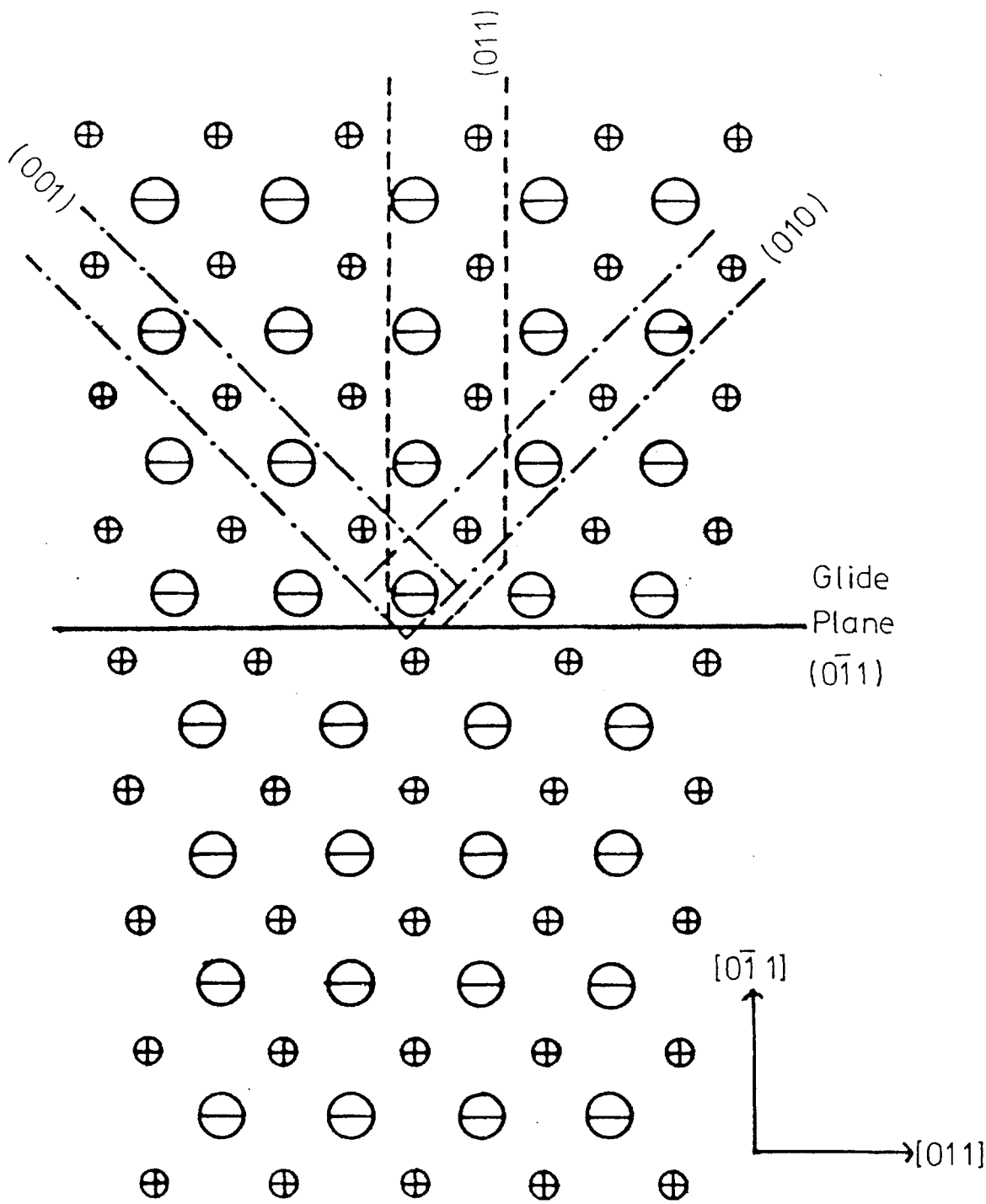


Fig. 2.5. Edge dislocation in NaCl.

2.1.4. Planar defects

Grain boundaries and free surfaces can be considered as imperfections because they disrupt the periodicity of the crystal. Many grain boundary models have been proposed by different workers in the past, and they fall into two basic types. Mott (101) has suggested a model consisting of 'islands' of good atomic matching surrounded by areas of mismatch. Burgers (22) described low-angle boundaries as arrays of edge and screw dislocations, which give rise to tilt and twist boundaries respectively. The limiting angle of mismatch between two grains, forming a boundary which can be analysed in terms of a dislocation model, will depend to a large extent on the crystalline structure and the impurities present. Usually the angle will be of the order of 15 to 30 degrees, High-angle boundaries, are best understood as 'slabs' of dislocation cores sandwiched between ordered regions. The tensile and compressive strain fields of dislocations in grain boundaries attract impurity ions of larger and smaller size, respectively. However, because of the charged nature of dislocations, a grain boundary can serve as a barrier to dislocation motion by applying a repulsive force.

2.2. Basic Concepts of Atomic Migration

Atomic migration in alkali halides is basically achieved by (a) vacancy, (b) interstitial, and (c) interstitialcy mechanisms.

(a) Vacancy mechanism

Figure 2.6 illustrates the Vacancy mechanism and shows an ion adjacent to the vacancy moving along a straight line that joins the original position of the ion with the vacancy on its ionic sublattice. The moving ion meets the strong repulsive force of two ions of opposite sign due to electron overlap. Energy, from the thermal vibrations of the ion, must be transferred to the ion to activate it sufficiently to overcome the energy barrier before it reaches the vacant site. While vacancies do move in a random fashion, a jump by a particular ion, e.g. a tracer ion in a diffusion experiment, is correlated with the jump immediately preceding it. Since a vacancy has an equal probability of exchanging with any of its neighbours, a tracer ion which has jumped to a vacant site has a finite possibility of a jump in the reverse direction. Thus not all tracer ion jumps will necessarily contribute to the general diffusion direction. This effect is accounted for by using a correlation factor, F, where

$$F = \frac{D_t}{D} \qquad 2.1.$$

D_t is the tracer diffusion coefficient and D is the true diffusion coefficient. The correlation factor is dependent on the lattice structure and the diffusion mechanism. From a more detailed study of diffusion using the random walk theory it can be shown that the correlation factor is given by

$$F = (1 + \overline{\cos\theta})/(1 - \overline{\cos\theta}) \qquad 2.2.$$

where $\overline{\cos\theta}$ is the average value of the cosine of the angle θ between successive jumps. Thus for purely random jumps which are statistically

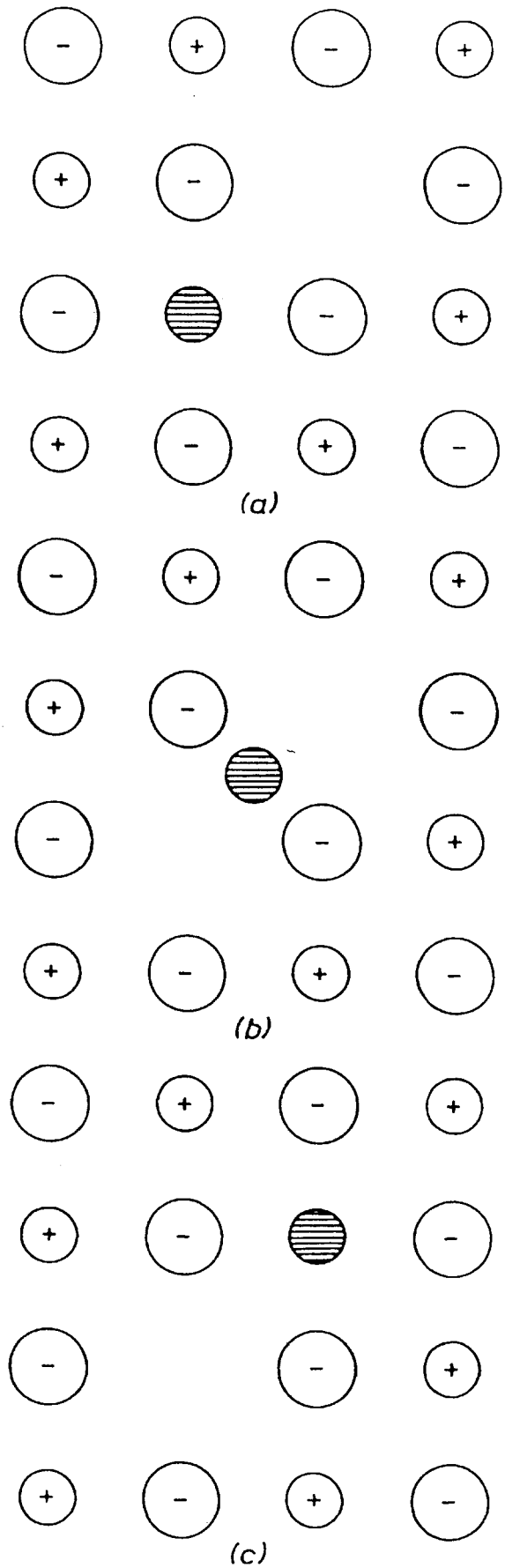


Fig.2.6. Vacancy migration in a sodium chloride crystal (a) initial normal position, (b) activated position, (c) final normal position.

independent $\overline{\cos\theta}$ approaches zero, and f approaches unity. For the opposite extreme, in which all jumps are followed by one in the reverse direction, then $\overline{\cos\theta} = -1$ and $f = 0$, and there is no net atomic displacement. In reality the correlation factors for the mechanisms that are responsible for diffusion generally fall between the two extremes. For the sodium chloride lattice, where diffusion proceeds mainly via jumps into vacant lattice sites, $f = 0.7815$.

(b) Interstitial mechanisms

Figure 2.7 illustrates the interstitial mechanism and the consecutive positions of the interstitials, with movement of an ion being in a random walk. However, this mechanism is not favoured in most alkali halides as the activation energy for such movement is too high.

(c) Interstitialcy mechanism

Figure 2.8 illustrates the interstitialcy mechanism in which a positive ion interstitial moves into a normal site by pushing the occupant positive ion into an adjacent cage. This can be achieved in a collinear and noncollinear manner. It has been shown that diffusion in the silver halides is via such a mechanism.

2.3. Concentration of vacancies

The surface of a crystal is irregular on an atomic scale, and provides an infinite source of vacancies. These vacancies can migrate through the crystal as described above. Vacancies can also migrate in the reverse direction from the bulk to the surface and be lost. Thus the crystal surface also serves as an infinite vacancy sink. In real crystals, the grain boundaries and dislocations are also efficient vacancy sources and sinks. At equilibrium, the rate at which vacancies are formed is equal to the rate at which they are lost. In this dynamic equilibrium, the vacancy concentration is determined by a compromise in the enthalpy - entropy relationship. The ideal state of minimum enthalpy is achieved by the most stable atomic configuration in

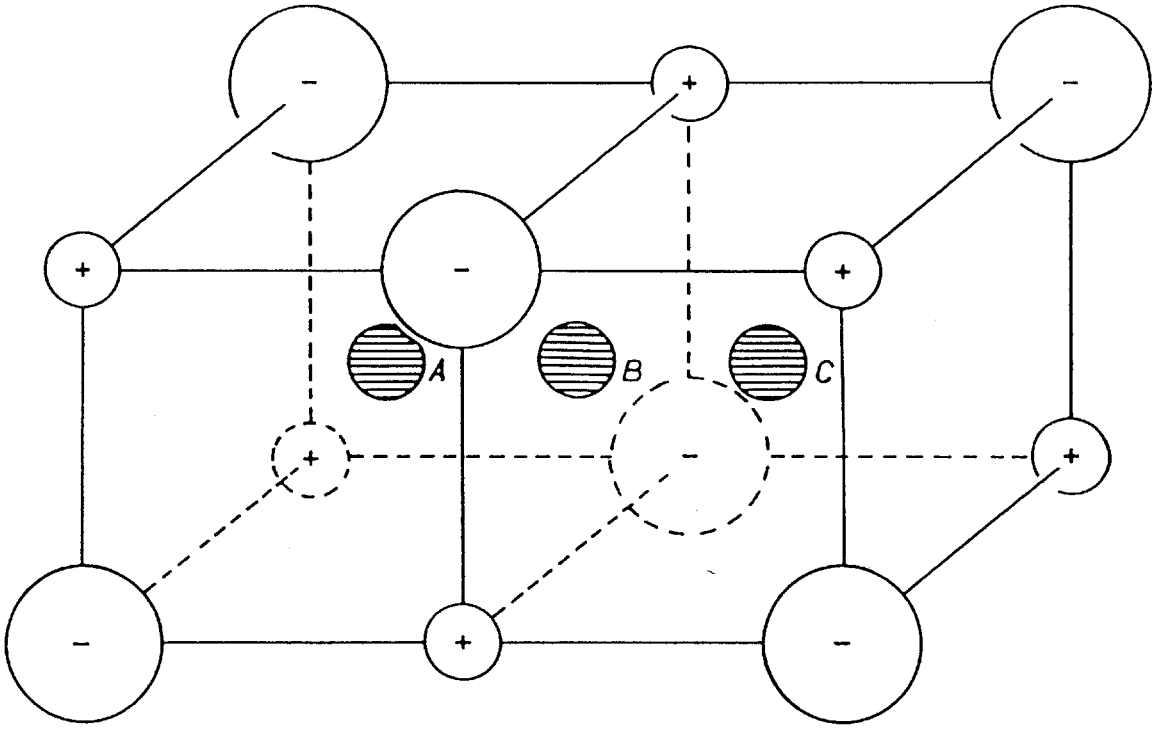
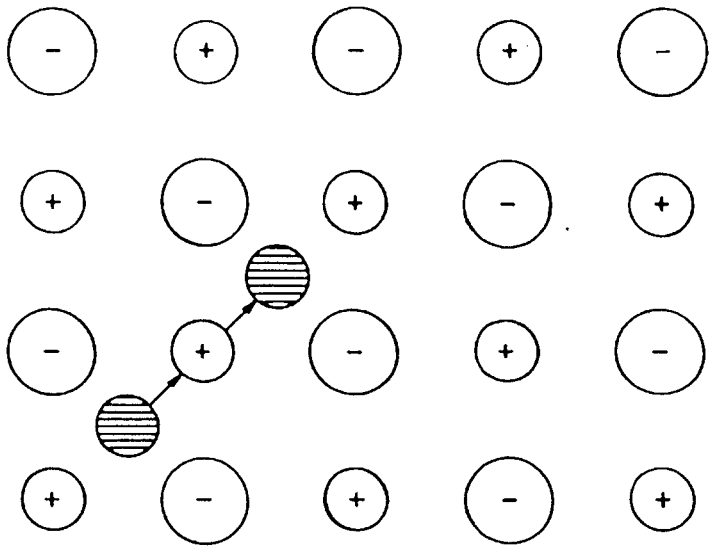
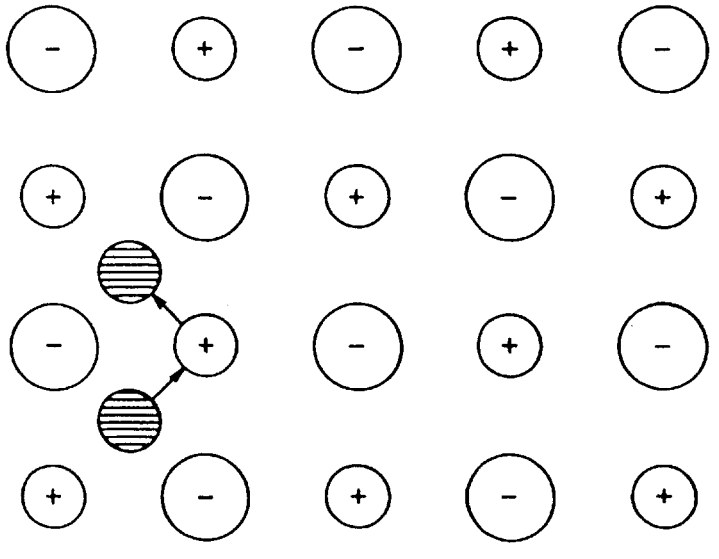


Fig.2.7. Motion of a positive ion interstitial in the sodium chloride structure: (a) positive ion in initial normal interstitial position, (b) positive ion in activated position, (c) positive ion in final interstitial position.



(a)



(b)

Fig.2.8. Interstitialcy jumps in ionic crystals: (a) collinear jump, (b) noncollinear jump.

which all atoms remain motionless in their regular positions. To attain maximum entropy all atoms are placed at random positions with no regularity at all. In an alkali halide crystal, this relationship is represented as

$$X_a X_c = \exp(\frac{\Delta S_f}{k}) \exp(-\frac{\Delta H_f}{kT}) \qquad 2.3.$$

where X_a and X_c are the mole fractions of anion and cation vacancies, T is the absolute temperature, k is the Boltzmann constant, and ΔS_f and ΔH_f are the entropy and enthalpy changes which occur in the formation of a Schottky pair of vacancies. The exponential term of minimum enthalpy change is a probability term that expresses the chances that a crystal, having thermal energy kT, will produce atomic vibrations sufficient to provide the energy for formation of a Schottky pair of vacancies. Equation 2.3. is sometimes written as

$$X_a X_c = \exp(-\frac{\Delta G_f}{kT}) \qquad 2.4.$$

where $\Delta G_f = \Delta H_f - T\Delta S_f$ 2.5.

ΔG_f is the free energy required to form a positive ion vacancy and a negative ion vacancy. The product relationship of Equation 2.4. is found to hold in thermal equilibrium, since it is derived from the need to maintain the crystal structure and charge neutrality. Thus, the concentration of either type of vacancy is the square root of Equation 2.4., i.e.,

$$X_a = X_c = \exp(-\frac{\Delta G_f}{2kT}) \qquad 2.6.$$

However, the product relationship of Equation 2.4. does not take into consideration the interaction between defects which result from long range Coulombic forces. Such interaction causes the distribution of anion and cation vacancies throughout the crystal to be non-random. The result of this is to lower the effective formation energy at high defect concentrations and temperatures.

Another type of point defect in alkali halides is an impurity ion, which can exist in 'pure' as well as in doped crystals (58). Monovalent cationic impurities do not affect the overall defect properties of the crystal, but aliovalent ions affect the host crystal significantly. These are generally situated in lattice sites, as they are too large to fit into the interstitial sites of alkali halides. If a divalent cation impurity is considered (a frequent impurity in NaCl), one can see intuitively that for overall charge balance, either a second cation vacancy must be created, or an anion must enter an interstitial site. As the former process is known to occur, due to the more favourable free energy change, the relationship between the atomic fraction of impurities and vacancies, can be written as

$$C + X_a = X_c, \qquad 2.7.$$

where C is the atom fraction of cationic sites occupied by divalent impurities. Combining Equations 2.4. and 2.7. gives the expression

$$X_c(X_c - C) = \exp(-\frac{\Delta G}{kT}) = X_o^2 \qquad 2.8.$$

and solving the quadratic equation for the positive root gives

$$X_c = \frac{C}{2}[1 + (1 + \frac{4X_o^2}{C^2})^{\frac{1}{2}}] \qquad 2.9.$$

When $X_o >> C$, then $X_c = X_o$, as in the case for pure Schottky disorder, but when $C >> X_o$, then $X_c = C$, which means that the concentration of defects is controlled by the amount of dopant added. The concentration of anion vacancies is similarly given by

$$X_a = \frac{C}{2}[(1 + \frac{4X_o^2}{C^2})^{\frac{1}{2}} - 1] \qquad 2.10.$$

It should be noted from Equation 2.4. that an increase in the cation vacancy concentration must be accompanied by a corresponding decrease in the anion vacancy concentration such that their product remains constant at any particular temperature. At high temperatures, the number of

cation vacancies varies exponentially with temperature in the intrinsic stage. As the temperature is decreased this number becomes fixed by the ever-present cation impurities in the extrinsic stage. As the temperature is further reduced and the impurity concentration is high, the divalent impurities associate with cationic vacancies as a result of electrostatic attraction, to form neutral dipoles. This species, similar to the divacancy pair, contributes to mass transfer, but not to charge transfer. In the lowest temperature range, defects may precipitate or segregate to other imperfections, and thus not contribute to either mass or charge transfer at all.

2.4. Theoretical Calculation of Diffusion Coefficient

Fick's First Law of Diffusion was developed from a consideration of unidirectional mass flow in a solid, assuming that the concentration, C, at a point, is independent of time, t. The derivation of this law can be found in a number of key textbooks, so that only the result will be given here. The flux J, of material passing through unit area of a plane, in unit time t, is given by

$$J = - D \frac{dc}{dx} \qquad 2.11.$$

where x is the distance in the diffusion direction, $\frac{dc}{dx}$ is the concentration gradient, and D is the diffusion coefficient. In the Random Walk Theory, which considers the random motion of a large number of particles moving without mutual or external influence, the value of the diffusion coefficient is given by the equation

$$D = \frac{1}{6} \Gamma \bar{r}^2 \qquad 2.12.$$

Where $\bar{r}^2$ is the mean square displacement of the particles, which undergo an average of Γ jumps per unit time. The jump distance is always the nearest neighbour distance. In the sodium chloride lattice, the distance

is $\frac{a_o}{\sqrt{2}}$, where a_o is the unit cell parameter. Rewriting Equation 2.12 gives

$$D = \frac{a_o^2}{12} \Gamma \qquad 2.13.$$

It has been shown that the cation is the mobile species in sodium chloride crystals and its diffusion is by the vacancy mechanism. For the sodium chloride structure, Γ is a probability factor which depends on (i) X_c, (ii) the number of cations surrounding a cation vacancy, i.e. the co-ordination number Z, and (iii) the jumping frequency ω,

i.e.

$$D = \frac{a_o^2}{12} X_c \; Z \; \omega \qquad 2.14.$$

The motion of a vacancy, and thus the probability of its motion ω, is a thermally activated process, and

$$\omega = \nu \exp - \frac{\Delta G_m}{kT}$$

$$= \nu \exp - \frac{\Delta H_m}{kT} \exp \frac{\Delta S_m}{k} \qquad 2.15.$$

where ν is the atomic vibration frequency which, as an approximation, is generally taken as the Debye frequency, ΔH_m and ΔS_m are, respectively, the migration enthalpy and vibration entropy of a ~~Schottky pair of~~ CATION vacancies. As the co-ordination number Z is 12 in the sodium chloride lattice, and X_c is given in Equation 2.6., Equation 2.14 becomes

$$D = a_o^2 \nu \exp \frac{\Delta S_f/2 + \Delta S_m}{k} \exp - \frac{\Delta H_f/2 + \Delta H_m}{kT} \qquad 2.16.$$

The more general form of the above equation is

$$D = D_o \exp - \frac{Q}{kT} \qquad 2.17.$$

where

$$D_o = a_o^2 \nu \exp \frac{\Delta S_f/2 + \Delta S_m}{k} \qquad 2.18.$$

and

$$Q = \Delta H_f/2 + \Delta H_m \qquad 2.19.$$

The frequency factor D_o in Equation 2.18. and the activation energy for diffusion Q in Equation 2.19. may be dependent on composition, but are independent of temperature. Equation 2.17 is of the Arrhenius type, and D varies exponentially with temperature. Thus a plot of ln D against 1/T for experimentally measured D values, at various temperatures, should give a straight line of slope Q/k and intercept D_o. Equation 2.19. applies only to diffusion taking place within the intrinsic temperature range where the vacancy concentration is thermally induced and decreases rapidly with a decrease in temperature. In the extrinsic temperature range, the vacancy concentration is constant, independent of temperature, and proportional to the divalent impurity concentration. The activation energy of diffusion, Q, in this range is the migration ~~energy~~ enthalpy only, and Equation 2.19 will not hold true.

Fick's First Law cannot be used to calculate the concentration profile as a function of time. For diffusion under such a non-steady state, Fick's Second Law is used, and is given by

$$\frac{dC}{dt} = D \frac{d^2C}{dx^2} \qquad 2.20.$$

Integrating Equation 2.20 under the boundary condition of thin initial source, and of an infinite diffusion front with respect to the depth of penetration, gives

$$C = \frac{C_o}{(\pi Dt)^{\frac{1}{2}}} \exp - \frac{x^2}{4Dt} \qquad 2.21.$$

In this equation C_o is the initial concentration at t = 0, and x = 0. Taking the natural logarithms of both sides of Equation 2.21, it becomes

$$\ln \frac{C}{C_o} = \ln \frac{1}{(\pi Dt)^{\frac{1}{2}}} - \frac{x^2}{4Dt} \qquad 2.22.$$

This equation is used in many diffusion experiments using the radioactive tracer sectioning technique, and a plot of $\ln \frac{C}{C_o}$ against x^2 will give a straight line with a negative slope of $(4Dt)^{-1}$

In a constant source condition, the diffusion equation is represented as

$$C = C_o \text{ erfc } \left(\frac{x}{2(Dt)^{\frac{1}{2}}} \right) \qquad 2.23.$$

where erfc is the complimentary error function. A plot of $\text{erfc}^{-1}(\frac{C}{C_o})$ versus x will give a slope of $1/2(Dt)^{\frac{1}{2}}$. Knowing t, D can then be calculated.

The application of Fick's Law to the grain boundary diffusion problem is best understood by visualising the grain boundary model as in Figure 3.1. The boundary is assumed to be a uniform slab of width δ, within which the diffusion coefficient, D', is larger than the value D in the rest of the specimen and thus diffusion occurs according to Fick's Laws. Tracer material is deposited on the free surface of the specimen and diffuses into it in the y direction. At a given distance from the surface, the tracer concentration is larger in the boundary than in the bulk. As a result of this concentration difference, the radioactive tracer will flow laterally from the grain boundary into the adjacent grains. For the region outside the boundary, Fick's Second Law gives

$$\frac{dC}{dt} = D \left(\frac{d^2C}{dx^2} + \frac{d^2C}{dy^2} \right) \qquad 2.24.$$

Within the grain boundary, however, it becomes

$$\frac{dC}{dt} = D' \frac{d^2C}{dy^2} - \frac{2}{\delta} J_x \qquad 2.25.$$

The first term in Equation 2.25 is the usual Fick's Law expression for a uni-dimensional flow. The second term arises because of the lateral leakage from the boundary, where J_x is the flux in the x direction at the boundary surface. According to Fick's First Law,

$$J_x = -D \left(\frac{dC}{dx} \right)_{\delta/2} \qquad 2.26.$$

where the derivative is evaluated at the grain boundary surface. Substituting Equation 2.26 into 2.25 gives

$$\frac{dC}{dt} = D' \frac{d^2C}{dy^2} + \frac{2D}{\delta} \left(\frac{dC}{dx}\right)_{\delta/2} \qquad 2.27.$$

The problem is therefore one of simultaneously solving Equations 2.24 and 2.27, subject to reasonable boundary conditions. Methods involving varying degrees of mathematical rigour have been applied by many workers to obtain the solution to this problem. These methods will be discussed in the next chapter.

CHAPTER THREE

REVIEW OF PREVIOUS LITERATURE

3.1. Solutions of Grain Boundary Diffusion

The possibility of preferential diffusion in grain boundaries was suggested for the first time in 1924 by Dushman and Koller, and interpreted ten years later by Langmuir (79). In 1928, Montel (100) published the first direct proof of grain boundary diffusion with the aid of radioactive isotopes (polonium in lead). However, it was not until 1951 that Fisher (37) published his solution of the grain boundary diffusion problem.

Fisher's solution was in a form which was very simple to apply to experimental results, but the derivation was very approximate. He assumed that diffusion along a thin layer of high diffusivity material, sandwiched between a large volume of low diffusivity material, is in a manner analogous to the diffusion of heat along a copper foil embedded in cork, as illustrated in Figure 3.1. Radioactive material, used as a tracer, was deposited on the free surface. For his diffusion mode, Fisher chose the boundary condition of zero initial concentration in the solid, with the surface maintained at a fixed concentration from zero time onward, i.e.

$$C(x,y,t) = Co \qquad t \geq 0 \quad y = 0 \qquad 3.1.$$

This intuitive picture of grain boundary diffusion, and its boundary conditions, was subsequently used by many workers in their analysis of boundary diffusion.

Diffusion occurred, according to Fick's Laws within a grain boundary "slab" of width, δ, and a diffusion coefficient D' much greater than the diffusion coefficient of the bulk D. D' and D were assumed to be independent of the source concentration. It was assumed that the slab was very thin and isotropic, and that concentration variations across its width were negligible. The instantaneous concentration in the slab was a function of y only, and varied according to Equation 2.28, the first term of which

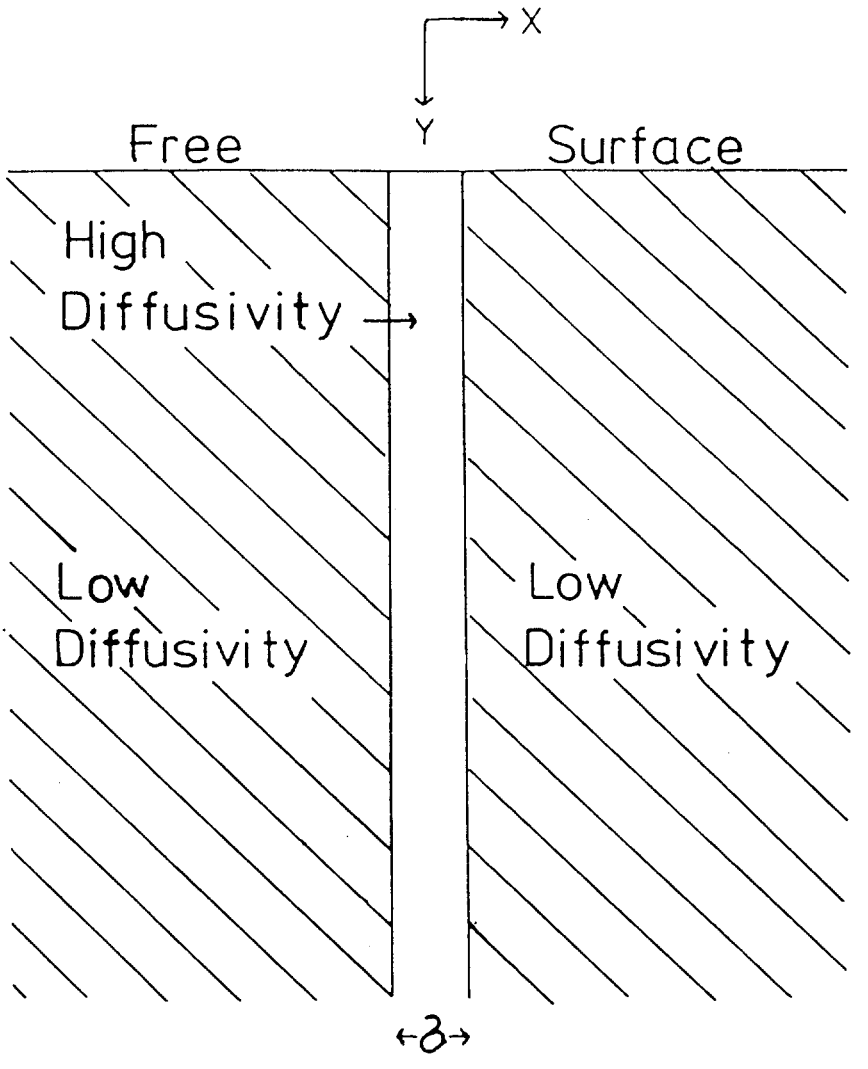


Fig.3.1. Coordinate system for diffusion outside a semi-infinite slab of high diffusivity material embedded in a semi-infinite solid.

represents the concentration change associated with the diffusion of material along the slab, and the second term, the change associated with the loss of material from the two sides of the slab. For a region outside the slab, Fisher assumed,

$$\frac{dC}{dt} = D\,\frac{d^2C}{dx^2} \qquad 3.2.$$

For Fick's equations given above, Fisher provided the following solution:

$$\frac{C}{C_o} = \exp(-\pi^{-1/4}\eta\beta^{-1/2})\,\mathrm{erfc}\,\frac{\xi}{2} \qquad 3.3.$$

where

$$\eta = y/(Dt)^{1/2} \qquad 3.4.$$

$$\beta = (\Delta-1)\alpha \qquad 3.5.$$

$$\Delta = D'/D \qquad 3.6.$$

$$\alpha = \delta/2(Dt)^{1/2} \qquad 3.7.$$

$$\xi = (x - \delta/2)/(Dt)^{1/2} \qquad 3.8.$$

Thus in a sectioning experiment, a plot of the logarithm of the specific activity, a, at a penetration y, versus the depth of the penetration y, should yield a straight line of slope,

$$\frac{d\ \log\ a}{dy} = -\left(\frac{2D}{D'\delta}\right)^{1/2}\frac{1}{(\pi Dt)^{1/4}} \qquad 3.9.$$

The value of $D'\delta$ can then be obtained if the value of D and t are known.

In 1954, Whipple (128) published his solution of the grain boundary diffusion problem. It is exact within the framework of the model on which it is based, but being in integral form, it is by no means convenient for ready application to experimental results. The conditions he chose for the free surface were the same as those of Fisher. Using a Fourier-Laplace Transformation, Whipple suggested the following solution,

$$\frac{C}{C_o} = \mathrm{erfc}\,\frac{\eta}{2} + \frac{\eta}{2\pi^{1/2}}\int_1^{\Delta}\frac{d\sigma}{\sigma^{3/2}}\exp\left(\frac{-\eta^2}{4\sigma}\right)\mathrm{erfc}\left[\left(\frac{\Delta-1}{\Delta-\sigma}\right)^{1/2}\left(\frac{\xi}{2}+\frac{\sigma-1}{2\beta}\right)\right] \qquad 3.10.$$

where C_o is the initial concentration on the free surface. The first term gives the contribution to C from direct volume diffusion, the second that

from grain boundary diffusion. When $\eta >> \beta^{\frac{1}{2}}$ and ξ was small, Whipple used the 'method of steepest decent' to give the asymptotic form of the above equation.

$$\frac{C}{C_o} = 1.159(\eta\beta^{-\frac{1}{2}})^{-2/3}\exp -[0.473(\eta\beta^{-\frac{1}{2}})^{4/3} - \frac{0.396}{\beta}(\eta\beta^{-\frac{1}{2}})^{2/3}(1-\beta\xi) + O(\beta^{-2})] \qquad 3.11.$$

To the same degree of approximation, the gradient of the concentration contours given by Whipple is,

$$\cot \phi = (\frac{\eta\beta}{4})^{1/3} - \frac{1}{3}(\frac{1}{2\eta\beta})^{1/3} \qquad 3.12.$$

By using Equation 3.12, a series of isoconcentric contours in the ξ and η planes, for various values of β, can be obtained, and the history of a given system at different times can be easily followed as illustrated in Figure 3.2.

LeClaire (85) pointed out that as t increases, β decreases, and the contour angle ϕ becomes less acute. For β values less than about 10, the preferential penetration down the boundary is much less evident compared with volume diffusion. When β is large, so that ϕ is small, diffusion in the grains on either side of the boundary takes place predominantly along the x-direction. It may then be a fair assumption to ignore d^2C/dy^2 in Equation 2.24, as being very small, compared with d^2C/dx^2. However, a number of workers, including Fisher, have made this approximation from the start, so that their solutions should only be reasonably compared with the exact solution, when β is large.

The assumption has been made by many workers that D and D' are independent of the concentration of the source. However, atomic quantities, such as the jump frequency and vacancy concentration, are influenced by the composition of the atomic environment since they are sensitive to the nature of the interatomic forces. Thus, when the concentration of diffusing species is high, the diffusion coefficient will be concentration

dependent. Such enhancement has been observed experimentally by Austin and Richard (7,8), and Chemla (26). Wei and Wuensch (127) reported a numerical solution to the diffusion equation having a tracer diffusion coefficient exponentially dependent on source concentration, $D = D_o \exp(\beta C)$, and the increase in the diffusion coefficient value is as high as 20% in the extreme case of shallow tracer penetration and thick source. For low concentration of the source, the local environment of a diffusing atom is not disturbed by modest changes in concentration and the diffusion coefficient is independent of concentration (47).

Following the work of Fisher and Whipple, Borisov and Lyubov (17), Geguzin et al (40), Levine and MacCallum (88), and Mimkes and Wuttig (91) published solutions based on the same grain boundary model. However, the main features of their results seem to have been previously established in Whipple's solution.

In 1964, Suzuoka (121) presented his exact solution for grain boundary diffusion based on an 'infinite source' surface condition which was later adopted by most subsequent workers. The surface boundary conditions chosen were

$$C(x,y,t) = K\,dy \quad x = 0 \quad t = 0 \qquad 3.13.$$

and

$$\frac{dC}{dy} = 0 \quad y = 0 \quad t > 0 \qquad 3.14.$$

where K is the surface density of the planar surface at t = 0. As with Whipple's solution, Suzuoka's solution is the sum of two terms, i.e.

$$C_s(x,y,t) = \frac{K}{(\pi Dt)^{\frac{1}{2}}}\left[\exp\left(-\frac{\eta^2}{4}\right) + \frac{1}{4}\int_1^{\Delta}\left(\frac{\eta^2}{\sigma} - 2\right)\exp\left(-\frac{\eta^2}{4\sigma}\right)\right.$$
$$\left.\operatorname{erfc}\left\{\left(\frac{\Delta-1}{\Delta-\sigma}\right)^{\frac{1}{2}}\left(\frac{\xi}{2} + \frac{\sigma-1}{2\beta}\right)\right\}\frac{d\sigma}{\sigma^{3/2}}\right] \qquad 3.15.$$

It should be noted that the second term was simply obtained from the second term of Whipple's equation 3.10 by operating $d/dy = (Dt)^{\frac{1}{2}}\, d/d\eta$ and

replacing C_o with K. An interesting feature of Suzuoka's solution is the minimum concentration contour along the grain boundary near the surface, in contrast to the general prediction of maximum concentration in the case of a constant concentration source. These features are illustrated in Figure 3.2. This phenomenon results from the local depletion of the 'instantaneous source', because diffusion is more rapid in the grain boundary than elsewhere. This was similarly observed by Austin and Richard (8), using electron probe microanalysis in detecting the diffusion of gold in copper bicrystals with a thin source (0.5μ). However, there could be an effect of surface diffusion relaxing the local depletion of the thin source, a fact ignored by Suzuoka, and making his exact solution too ideal compared with the actual diffusion conditions.

A comparison of Fisher's and Whipple's constant concentration source solutions, and Suzuoka's infinite concentration source solution, to grain boundary diffusion, is shown graphically in Figure 3.3. The theoretical curves were compared using $\beta = 4$, since in Austin's data $\beta = 3 \sim 5$. It is observed that Austin's experimental curve is closer to C_{II} than to C_I, but there is an obvious effect from surface diffusion which acts as a secondary source to the boundary diffusion. The excess concentration caused is shown as the shaded area in Figure 3.3. Austin's data appears to underestimate the concentration in the region of $\eta = 3 \sim 5$. A possible explanation may be that the microprobe technique used is not sufficiently powerful for the detection of low concentration at such depths. It can be clearly seen that the constant and infinite concentration source solutions agree when $\eta > 5$, and thus $D'\delta$ should be determined in this range.

In the sectioning method for determining the grain boundary diffusion coefficient, a general relationship is derived from Equation 3.4 - 3.8 in the form:

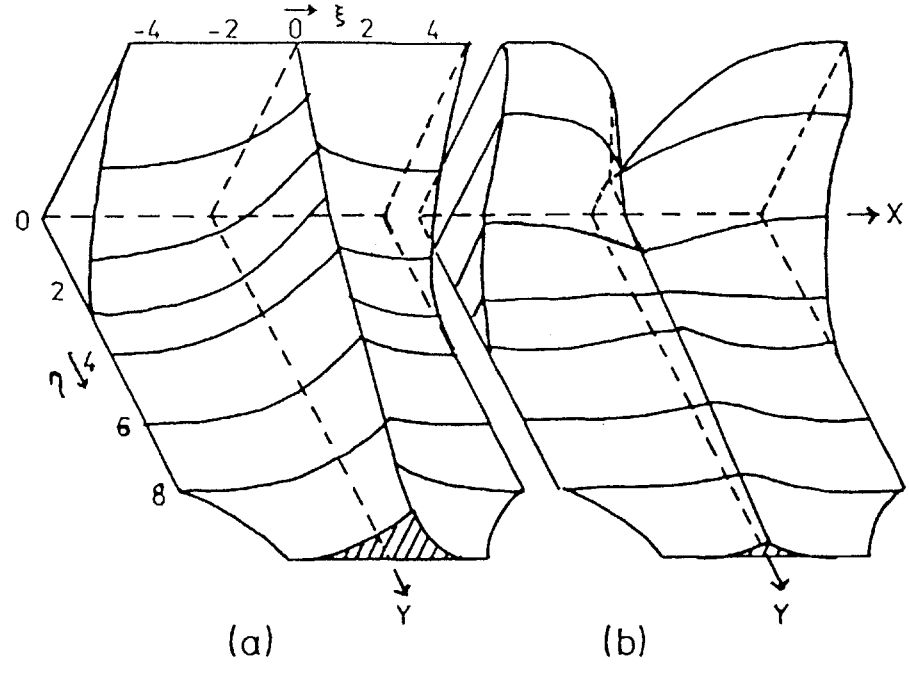


FIG.3.2 Concentration contours in a solid having a single grain boundary perpendicular to X-axis when $\beta = 50$. The surface is perpendicular to the Y-axis.

(a) C_I : constant concentration source

(b) C_{II} : instantaneous source

(after Suzuoka[121])

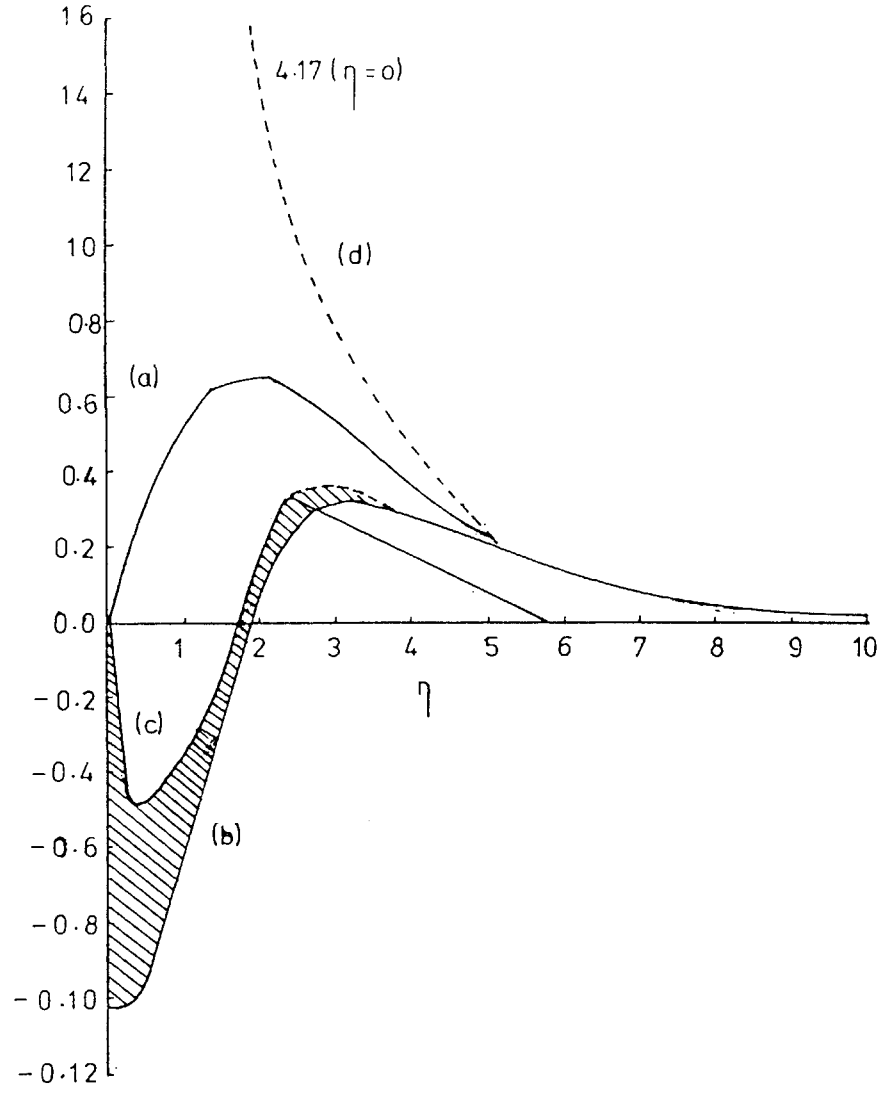


FIG.3.3 Average concentration for $\beta = 4$

(a) C_I : constant concentration source

(b) C_{II} : instantaneous source

(c) $(\bar{C}_{gb})_{obs}$: experimental curve obtained by Austin et al[8] on gold into a copper bicrystal for 10 hours at 760 °C

(d) Simple extrapolation from Fisher's solution (after Suzuoka[121])

$$D'\delta = \left(\frac{d \ln \bar{c}}{dy}\right)^{-2} \left(\frac{4D}{t}\right)^{\frac{1}{2}} \left[\frac{d \ln \bar{c}}{d(\eta\beta^{-\frac{1}{2}})}\right]^{2} \qquad 3.16.$$

Integration of Fisher's equation 3.3. with respect to ξ, gives the last term of the above equation a constant value of $\pi^{-\frac{1}{2}}$ which is independent of $\bar{c}$ or y. Thus $\ln\bar{c}$ varies linearly with y. LeClaire (85) showed that the value of $\frac{d \ln \bar{c}}{d\ \eta\beta^{-\frac{1}{2}}}$ or A, derived from Whipple's equation, depends on $\eta\beta^{-\frac{1}{2}}$, as shown in Figure 3.4. A varies from 1 to 1.5, but is comparatively insensitive to β when $\beta > 10$. Thus a plot of $\ln \bar{c}$ versus y should not be precisely linear. LeClaire noted that Whipple's asymptotic solution becomes a good approximation for A, only if the values of $\eta\beta^{-\frac{1}{2}}$ are larger than 9 or 10. When the solution is used outside its range, the values of $D'\delta$ obtained from Equation 3.16. will be too large. Levine and MacCallum (88) reported that the value $A^{6/5}$ is nearly independent of $\eta\beta^{-\frac{1}{2}}$ over much of the commonly used range of $\sim$ 2 to 10. Therefore, Equation 3.16. should be modified to give

$$D'\delta = \left(\frac{d \ln \bar{c}}{dy^{6/5}}\right)^{-5/3} \left(\frac{4D}{t}\right)^{1/2} \left[\frac{d \ln \bar{c}}{d(\eta\beta^{-1/2})^{6/5}}\right]^{5/3} \qquad 3.17.$$

The slope should then be determined from the plots of $\ln \bar{c}$ versus $y^{6/5}$, rather than $\ln \bar{c}$ versus y, and the value $D'\delta$ calculated using the constant value of $\frac{d \ln \bar{c}}{d(\eta\beta^{-1/2})^{6/5}} = 0.78$. Borisov and Lyubov (17) gave a solution which indicated A should be 0.99, but this value only applies for a limited range of low values of $\eta\beta^{-1/2}$. The value A = 0.78 suggested by Levine and MacCallum is in good agreement with those obtained by Suzuoka from his instantaneous source solution, which is given by

$$\frac{d \ln \bar{c}}{d(\eta\beta^{-1/2})^{6/5}} = 0.72\beta^{0.008} \qquad 3.18.$$

This gives 0.72 at $\beta = 1$ and 0.75 at $\beta = 100$. These values are at most 5% different from those of Levine and MacCallum, whose work was based on Whipple's constant concentration source condition. Such a variation is less than the possible experimental errors. For the sectioning technique

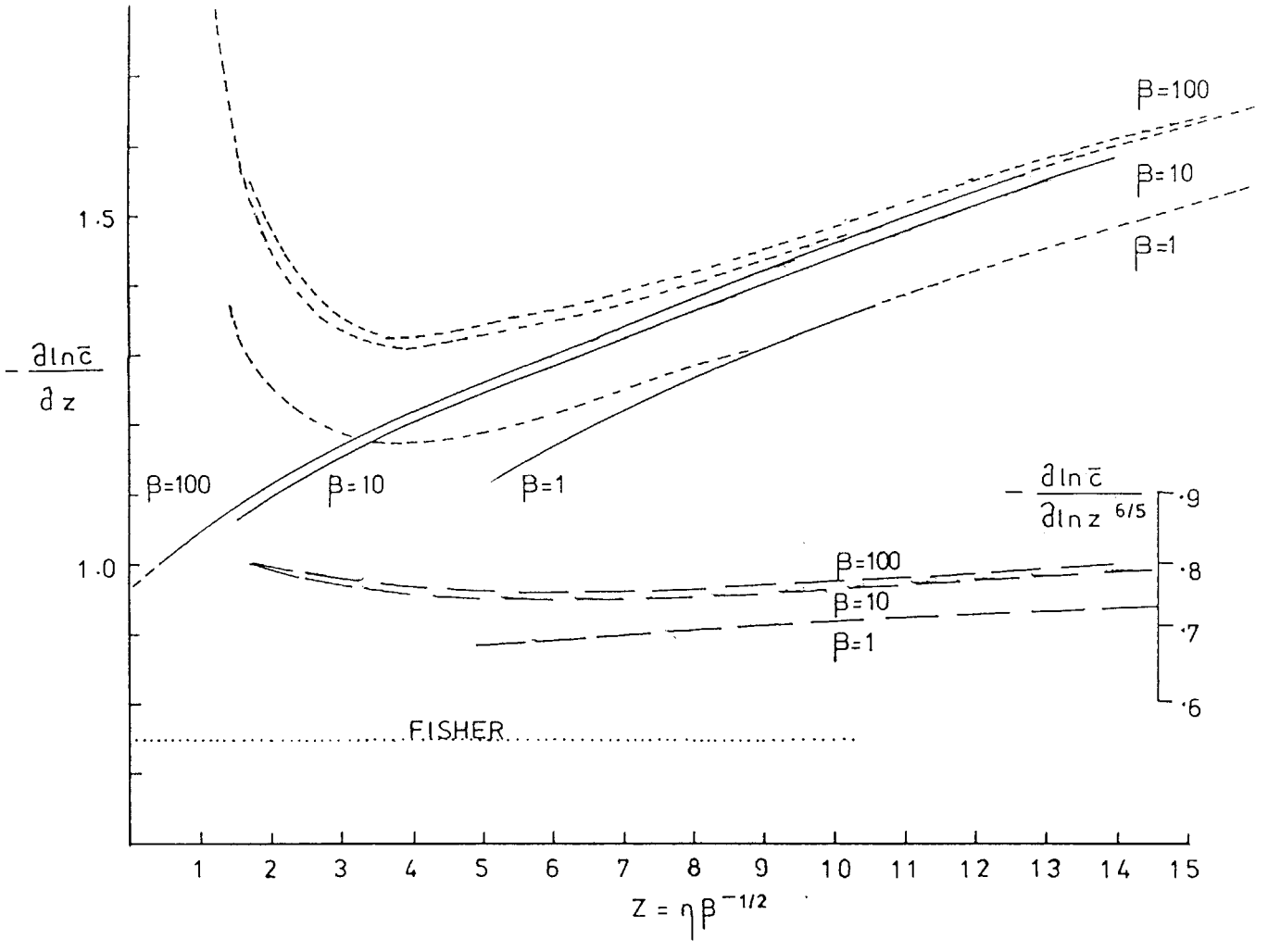


FIG.3.4 Slope of $\ln \bar{c} \sim \eta \beta^{-\frac{1}{2}}$ and $\ln \bar{c} \sim (\eta \beta^{-\frac{1}{2}})^{6/5}$ plots (after LeClaire[85])

then, and all practical purposes, Suzuoka's and Whipple's solutions give approximately the same value of $D'\delta$, which is not only independent of the mathematical conditions assumed for the surface source, but is also independent of the departure of the experimental surface condition from the ideal. Thus, the use of the sectioning method has a distinct advantage over the others in the study of grain boundary diffusion.

Figure 3.4. shows that Fisher's constant value of $d \ln \bar{c}/d(\eta\beta^{-1/2})$ is always smaller than that obtained by Whipple, and Levine and MacCallum. Thus the value of $D'\delta$ calculated from Equation 3.16. using Fisher's solution is always smaller than the true value, which leads to an anomalously high activation energy for boundary diffusion.

LeClaire showed that while β remains large, C is a function only of $\eta\beta^{-1/2}$, as illustrated in Figure 3.5., so that for the apex of a given concentration contour $\eta\beta^{-1/2}$ constant. Thus from Equations 3.4 - 3.8., the depth at which a given concentration is to be found varies with the time of anneal to the power one quarter, i.e. $y \propto t^{1/4}$. When β falls below 10, $\eta\beta^{-1/2}$ is no longer constant and y begins to increase at a more rapid rate than in proportion to $t^{1/4}$. This behaviour has also been observed by Yukawa and Sinnot (134).

3.2. Solution of Isolated Dislocation Diffusion

One of the more common manifestations of fast dislocation diffusion is in tracer diffusion experiments with single crystals using the conventional sectioning method. In the logarithmic plot of the concentration of diffused tracers, C, in a section versus the square of the distance y from the surface at which the section was cut, the plot is initially linear and the volume diffusion coefficient is calculated from the slope. However, measurements of the tracer concentration carried to sufficient depths reveal a tail, of much smaller average slope, often extending to considerable distances. In this 'tail' region, lnC is proportional to y,

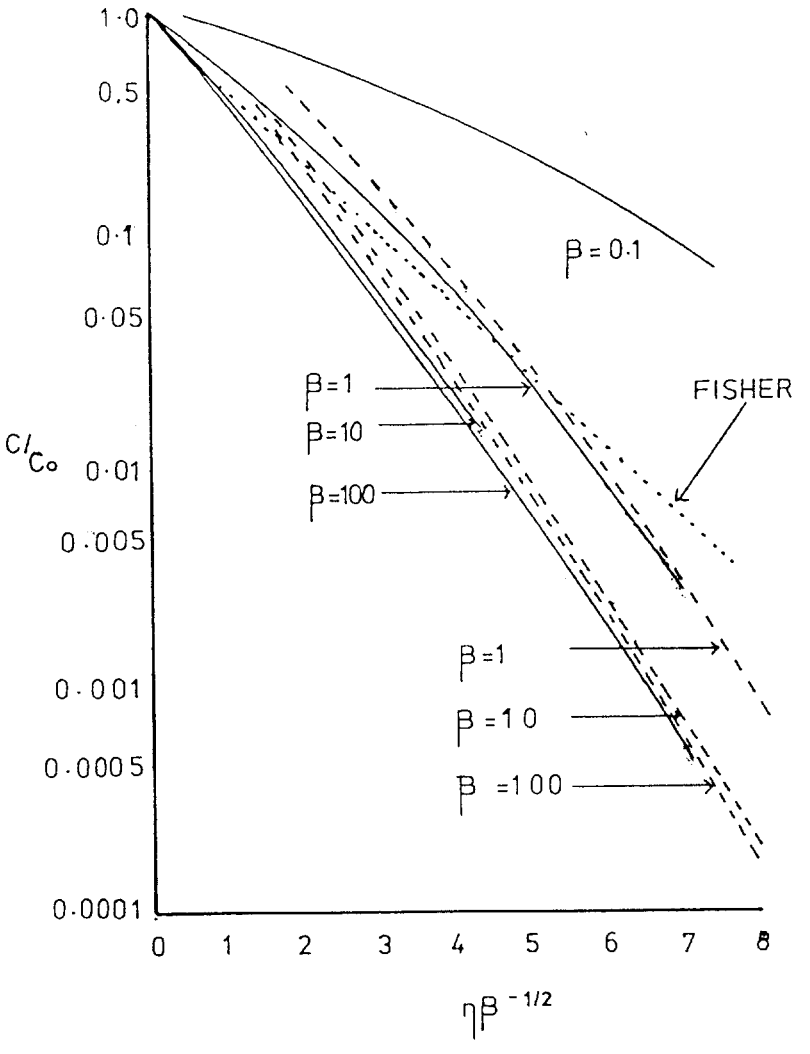


FIG.3.5 Relative concentration in the grain boundary as a function of $\eta\beta^{-\frac{1}{2}}$ (after LeClaire[85])

and diffusion is greatly enhanced by the presence of the dislocations. The kinetics of such diffusion has been extensively studied by Harrison (60) who described three types:

Type A: This is observed when $(Dt)^{1/2} >> d$ where d is the average distance between dislocations. It has been suggested that a less restrictive condition might apply (9, 50, 78), i.e. when $(Dt)^{1/2} \sim d$ provided that the penetration depth is less than $4(Dt)^{1/2}$. When this condition is satisfied, a tracer atom samples dislocations and the penetration profile can be characterised by a single diffusion coefficient D_{eff} where

$$D_{eff} = (1 - f)D + f D_d \qquad 3.19.$$

f being the fraction of atomic sites that are in the region of dislocations. This type of behaviour was first suggested by Hart (61) who analysed the situation using generalised 'random walk' consideration.

Type C: This is observed when $(Dt) << a$ where a is the radius of the dislocation pipe. This condition can be achieved by using a short diffusion time or short diffusion distance, or $D_d >> D$. In this case, diffusion from a dislocation pipe into the surrounding lattice can be neglected, and the tracer profile is again characterised by a single diffusion coefficient D_d. This has been experimentally demonstrated by Ghoshtagore (45) and Atkinson (6).

Type B: This is observed when the condition for neither type A nor type C is satisfied. Diffusion is now along dislocations and into the surrounding lattice. The penetration profile is thus composed of a near surface region dominated by D, and a penetrating 'tail' from which parameters describing the dislocation diffusion may be obtained.

Where the dislocation "tails" arise from dislocations aligned in arrays constituting low angle boundaries, they have been analysed by assuming that the transport down and out of the dislocations can be identified with the transport down and out of some equivalent homogeneous grain boundary (9, 123). This is a poor approximation, especially if the dislocations are as well separated as they need to be for the boundary structure to be represented in terms of dislocations. Nevertheless the approximation does allow the use of the Fisher or Whipple solutions for grain boundary diffusion in the derivation of an effective diffusion coefficient for the component dislocations.

The first study of diffusion down and out of an individual dislocation was made by Smoluchowski (115). He discussed diffusion from a plane surface into a semi-infinite crystal containing such a dislocation pipe running normal to the surface, and employing some rather gross approximations analogous to those Fisher used for treating the similar grain boundary problem. In 1965, Stark (118) attempted a solution of the dislocation diffusion problem which avoided the Fisher type approximation used by Smoluchowski, but his results are too incomplete to be of much use. Brebec (19) reported a near exact double integral expression for the tracer concentration as a function of penetration distance, the time and the radial distance from the dislocation, but this was not sufficiently developed in a useful form.

In 1970, Mimkes and Wuttig (92, 93) claimed an exact solution for the dislocation pipe diffusion for an instantaneous source. The solution is represented as

$$Q(\eta) = \frac{\gamma}{(\pi Dt)^{1/2}}\left[\exp\left(-\frac{\eta^2\xi^2}{4}\right) + \varepsilon^{1/2}\int_1^{\Delta}\int_{\varepsilon}^{1}\left(\frac{\eta^2\xi^2}{2\sigma} - 1\right)\exp\left(-\frac{\eta^2\xi^2}{4} - \frac{\sigma-1}{\Delta-1}\frac{k^2}{\varepsilon^2}\right)\right.$$

$$\left. \times\ \rho^{1/2}\, d\rho\ \mathrm{erfc}\left\{\left(\frac{\Delta-1}{\Delta-\sigma}\right)^{1/2}\left(\frac{\rho-\varepsilon}{2k} - \frac{\sigma-1}{\Delta-1}\frac{k}{\varepsilon}\right)\right\}\sigma^{-3/2}d\sigma\right] \qquad 3.20.$$

where $k = \left(\frac{Dt}{A}\right)^{1/2} = (\pi m Dt)^{1/2}$ 3.21.

$$\varepsilon = \frac{a}{A} = (\pi m a^2)^{1/2} \qquad 3.22.$$

a is the pipe radius, 2A is the mean distance between pipes and m is the dislocation density. The solution is similar to Suzuoka's solution of grain boundary diffusion for an instantaneous source. LeClaire and Rabinovitch (86) suggested that substantial errors arise using the above solution because of an unjustified mathematical approximation made to simplify the reduction of an integral. Also, the double integrals of the Mimkes solution were not systematically evaluated. The general features of the solution are therefore not clear and direct application to the analysis of experimental data is not possible without tiresome numerical integration in each case.

In 1981, LeClaire and Rabinovitch (86) presented a mathematical description of dislocation diffusion which avoided the approximations employed by previous authors. In their dislocation diffusion model, diffusion occurs from a plane surface, $y = 0$, into a semi-infinite solid containing an isolated and straight dislocation 'pipe' ending in the surface and at right angles to it. Well away from the pipe, where $x >> a$, a being the pipe radius, diffusion occurs normal to the surface with the coefficient D. Down the pipe there is rapid diffusion of material at a rate determined by D_d, with loss from the sides at a rate governed by D. The contours of constant concentration will therefore look in section like that depicted in Figure 3.6. The only, assumptions made are that the concentration within the pipe is uniform radially (because $D_d >> D$), and equal to the concentration outside at $x = a$, and D_d and D are independent of concentration of the source.

If C and C' represent the concentration of diffusant outside and inside the pipe respectively, the equations to be solved are

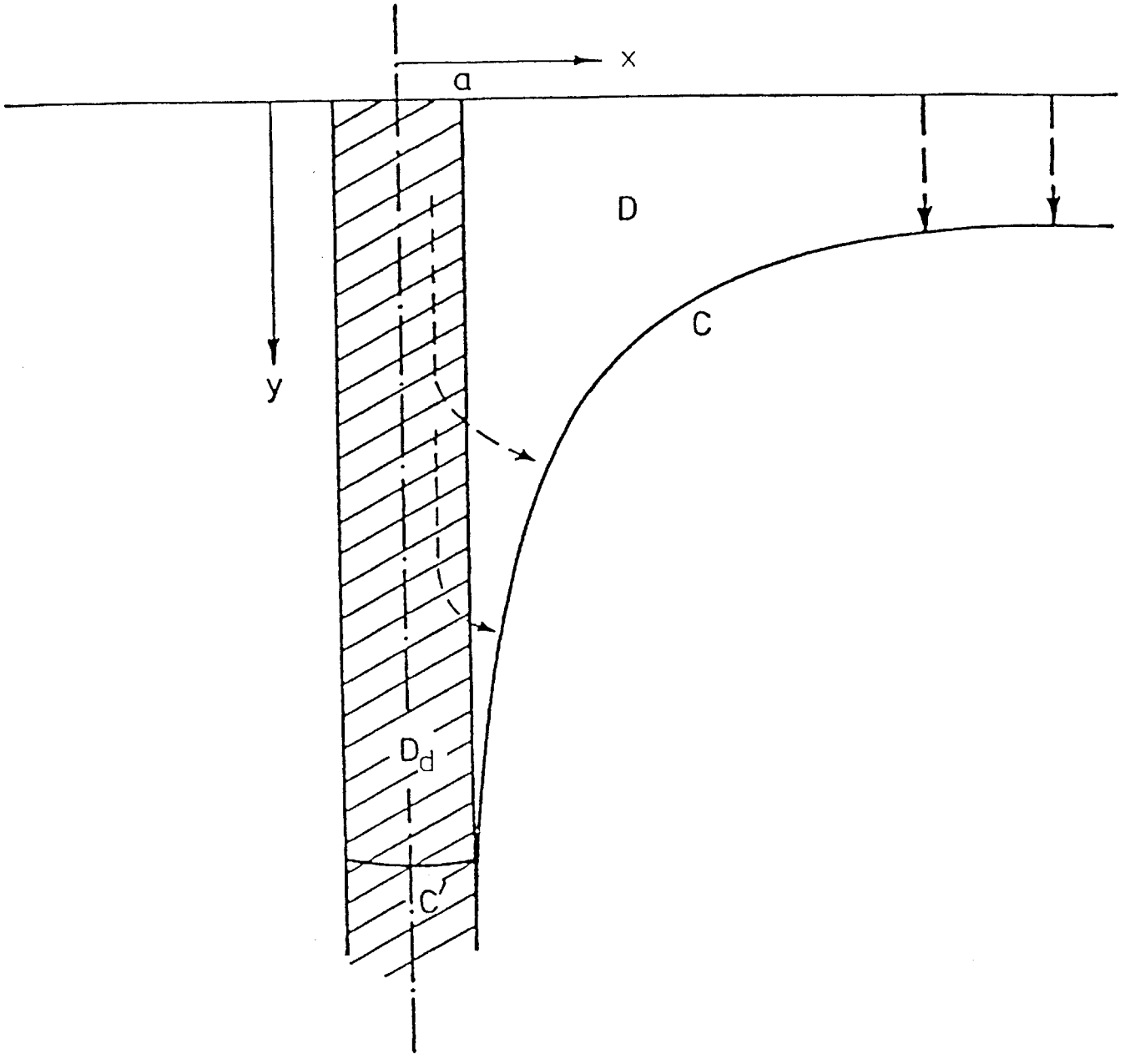


Fig. 3.6. A concentration contour resulting from diffusion down and out from a dislocation pipe. [after LeClaire and Rabinovitch[86]]

$$\frac{dC}{dt} = D\{\frac{1}{x} \cdot \frac{d}{dx}(x \frac{dC}{dx}) + \frac{d^2C}{dy^2}\} \qquad 3.23.$$

outside the pipe ($x \geq a$) and

$$\frac{dC'}{dt} = D_d \{\frac{1}{x} \cdot \frac{d}{dx}(x \cdot \frac{dC'}{dx}) + \frac{d^2C'}{dy^2}\} \qquad 3.24.$$

inside the pipe ($x < a$), subject to the boundary conditions that at $x = a$ there must be continuity of flux and of concentration, i.e.

$$(D \frac{dC}{dx})_{x=a^+} = (D_d \frac{dC'}{dx})_{x=a^-} \qquad 3.25.$$

and

$$C_{(x=a^+)} = C'_{(x=a^-)} \qquad 3.26.$$

Two cases were considered according to the condition at the surface $y = 0$. In case I the concentration at the surface is maintained constant at a value C_o for all $t > 0$,

$$\text{I} \quad C_{(y=0,\ r,t)} = C_o \qquad 3.27.$$

In case II, a very thin layer of diffusant, of quantity γ per unit area, is deposited on the surface at $t = 0$. The concentration at $t = 0$ can be written in terms of the Dirac δ function as

$$\text{II} \quad C_{(t=0)} = 2\gamma\delta(y) \qquad 3.28.$$

The factor 2 is a normalising constant that makes $\int_0^\infty C.dy = \gamma$.
Case II is intended to simulate the conditions of a conventional 'thin film' tracer diffusion measurement. However, it is only fully appropriate if there is, in practice, no rapid diffusion along the surface towards the dislocation to compensate for the loss near $x = 0$ due to rapid diffusion down the dislocation. By tending to maintain the concentration near $x = 0$ such diffusion introduces an element of the case I condition. In fact, case I may be the more appropriate if only very little of the deposited layer diffuses into the sample, e.g. when there is only a very small solubility of diffusant, or when the time is

short or the temperature low. In practice, neither cases may exactly represent the situation prevailing at the surface, although they probably do represent the limits which encompass unlikely experimental condition.

In the sectioning experiment, slices cut from real samples, contain many dislocations, assumed to be unlinked at a depth y below the surface. The mean concentration of diffusant is the sum of two terms, i.e. C_1, the concentration in the absence of any dislocation, plus C_2 the contribution outside a dislocation, or C_2' inside, due to $D_d >> D$. Thus,

$$C_{(y)} = C_{1(y)} + \rho q_{(y)} \qquad 3.29.$$

where ρ is the dislocation density (number per cm^2) and $q_{(y)}$, the additional contribution from one dislocation, assumed the same for each, is

$$q_{(y)} = \int_o^a 2\pi x C_2'(x,y)dx + \int_a^\infty 2\pi x C_2(x,y)dx \qquad 3.30.$$

$$= q_i + q_x$$

The upper limit on the second integral can be taken as ∞, rather than as some sample dimension L, because $C_2(x,y)$ will become negligible at a distance $x << L$, viz. at $x \simeq$ few $(Dt)^{1/2}$. C_2 and C_2' are obtained from the solution of Equations 3.23 and 3.24 for a single isolated dislocation, i.e. from solutions such that C_2 and $dC_2/dx \to 0$ as $x \to \infty$. Thus, the dislocations are assumed to act independently, in the sense that no significant amount of material that has diffused down and out of one dislocation ever reaches another. The condition that C_2 becomes negligible within a distance $x \simeq \rho^{-1/2}$, i.e. $(Dt)^{1/2} << \rho^{-1/2}$, would ensure this, but it may be too strong a condition: other dislocations only occupy small and separated regions comprising a small fraction of the total volume available for the diffusion of material out of one dislocation. This situation differs from that for grain boundaries where the flux out of one boundary is perturbed over its whole front by adjacent boundaries. Using the isolated dislocation solution for C_2 in

Equation 3.30 may offer a good approximation for higher dislocation densities than those indicated by the above condition. This may be especially so for large values of y because as y increases so the spread of material from the dislocation is reduced.

A more rigorous treatment of the problem would calculate the concentration arising from diffusion down and out of some assumed array of dislocations, seeking solutions such that $dC/dx = 0$ midway between nearest neighbour dislocations. The upper limit of the C_2-integral in Equation 3.30 would then be this midway distance. Mimkes and Wuttig actually use such an upper limit in their C_2-integral while still employing their isolated dislocation solution for C_2 with $dC_2/dx \to 0$ as $x \to \infty$. This seems an inconsistency that must lead to q being underestimated. The tail concentrations calculated from the Mimkes and Wuttig approximation are one to several orders of magnitude smaller than the values calculated using the solution of LeClaire and Rabinovitch.

Equations 3.23 and 3.24 are solved via a Fourier Laplace transformation. The rigorous mathematics of which has been reported by LeClaire and Rabinovitch (86). Only the results are quoted here.

$$\text{Case I, } C_{(\eta)}{}^{I} = Co\{\operatorname{erfc} \frac{\eta}{2} + \varepsilon^2 Q^I\} \qquad 3.31.$$

where ε^2 is the fraction of atom sites that are in the dislocation pipes, and is written as $\pi a^2 \rho$, and

$$Q^I = \frac{16\beta^2}{\pi^3 \alpha^2} \int_o^\infty x^3 \exp -x^2 \sin \eta x dx \int_o^\infty \frac{(1-\exp -z^2)dz}{(\Theta^2 + \phi^2)z^3} \qquad 3.32.$$

In the above equations,

$$\alpha = a/(Dt)^{1/2}$$

$$\beta = (\Delta - 1)\alpha$$

$$\eta = y/(Dt)^{1/2}$$

$$\Theta = 2zY_1(z\alpha) + (x^2\beta - z^2\alpha)Y_o(z\alpha)$$

$$\phi = 2zJ_1(z\alpha) + (x^2\beta - z^2\alpha)J_o(z\alpha)$$

J_o and Y_o are zero order Bessel functions of the first and second kind, respectively, as are J_1, Y_1, of order one.

$$\text{Case II,} \quad C_{(\eta)}^{II} = \frac{\gamma}{(\pi Dt)^{1/2}} \{\exp - \frac{\eta^2}{4} + \varepsilon^2 Q^{II}\} \qquad 3.33.$$

where

$$Q^{II} = - \frac{16\beta^2}{\pi^{5/2}\alpha^2} \int_o^\infty x^4 \exp - x^2 \cos \eta x dx \int_o^\infty \frac{(1-\exp-z^2)dz}{(\theta^2+\phi^2)z^3} \qquad 3.34.$$

LeClaire and Rabinovitch, using numerical integration, computed values of Q^I and Q^{II} for a range of α and β values. Their graphical representations are shown in Figures 3.7 and 3.8.

In Figures 3.7 and 3.8, it can be seen that beyond $\eta = 4$ or 5, the slopes are effectively linear for $\alpha \lesssim 1$. These regions correspond to the 'tail' feature in the dislocation diffusion plots observed experimentally at η values large enough for the volume diffusion contribution to become negligible. As α increases much above 1 the plots become non-linear, with a negative curvature. For very large α values, which implies very little diffusion other than within the pipe, $\log_{10} Q^{II}$ become proportional to $- \eta^2/4\Delta$ and Q^I proportional to erfc $(\eta/2\Delta^{1/2})$.

Q^I passed through a maximum and decreases rapidly for $\eta \lesssim 2$, and becomes zero at $\eta = 0$. Q^{II} also passes through a maximum, at slightly higher values of η, and decreases rapidly to change sign before reaching a finite negative value at $\eta = 0$. Negative values of Q^{II} are expected for small η values because the finite amount of material deposited will be rapidly depleted from around the pipe by the rapid diffusion down it.

For given α and $\alpha\beta$ values the gradients of these linear regions are exactly the same for Q^I and for Q^{II}. The advantage that this feature has in not being influenced by any uncertainty about the surface conditions is fully exploited in solving the dislocation diffusion problem. The gradient which depends strongly on $\alpha\beta$, but only weakly on α, can be conveniently represented as

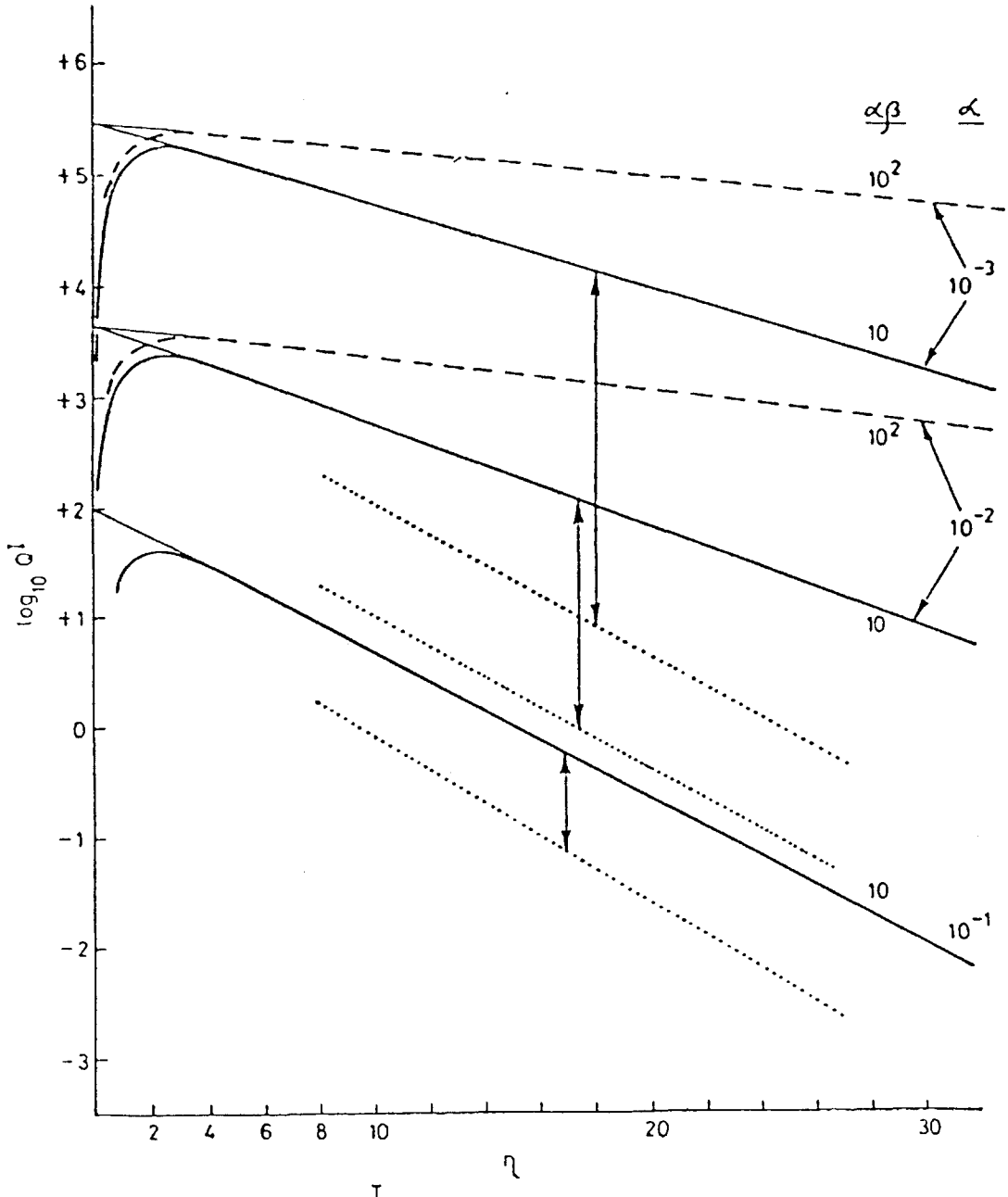


Fig.3.7. Plot of $\log_{10} Q^I$ versus η. [after LeClaire and Rabinovitch (86)]

Full lines Eqn.3.32 $\propto \beta = 10; \propto = 10^{-3}, 10^{-2}, 10^{-1}$.

Dashed lines Eqn.3.32. $\propto \beta = 10^2; \propto = 10^{-3}, 10^{-2}$.

Dotted lines (Mimkes and Wuttig) $\propto \beta = 10, \quad = 10^{-3}, 10^{-2}, 10^{-1}$.

Vertical arrows connect corresponding solutions of Eqn.3.32. and Mimkes and Wuttig's solution.

$Q^I = 0$ at $\eta = 0$.

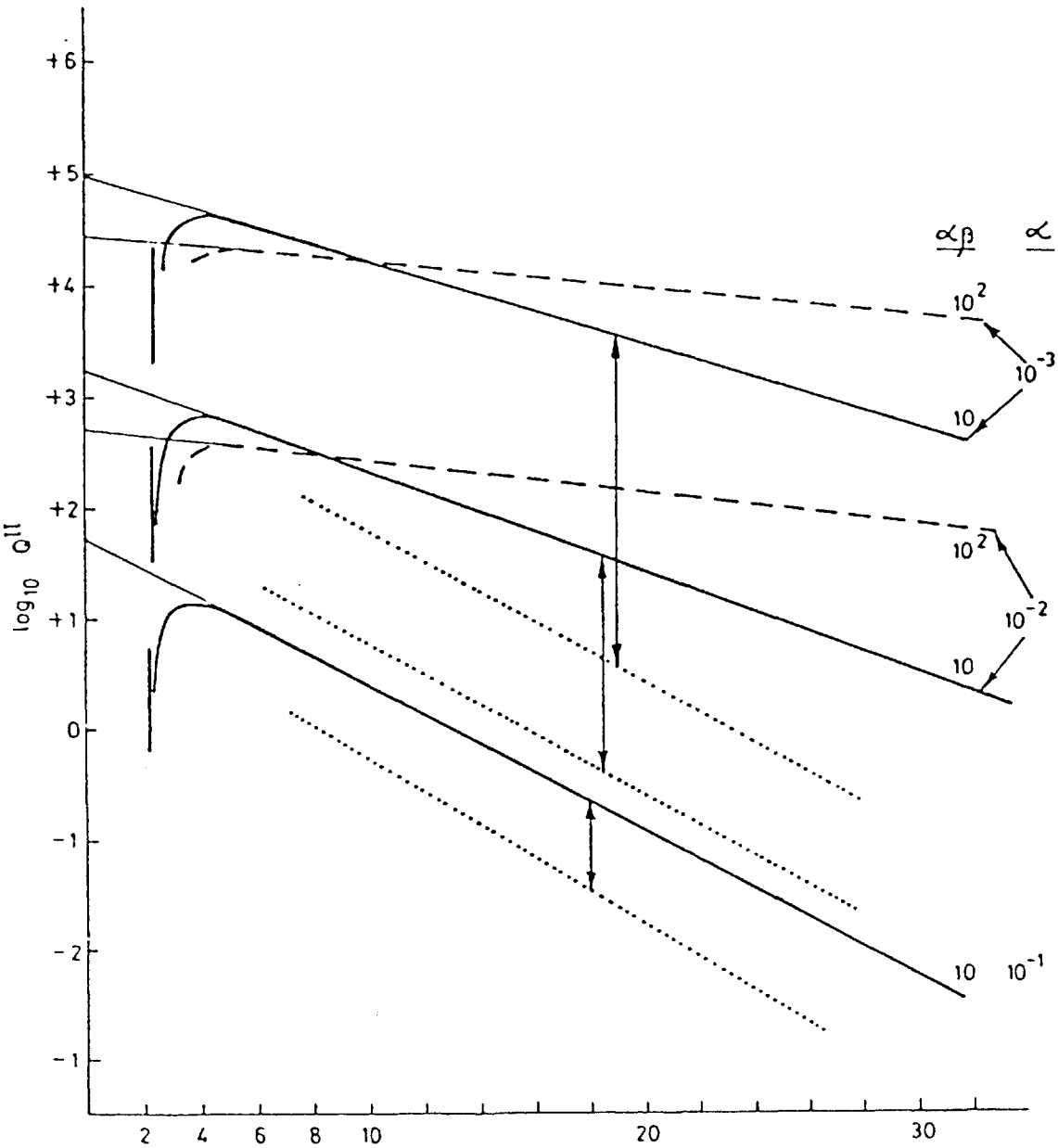


Fig.3.8. Plot of $\log_{10} Q^{II}$ versus η. [after LeClaire and Rabinovith [86]]

Full lines Eqn.3.34. $\alpha\beta=10$; $\alpha=10^{-3}, 10^{-2}, 10^{-1}$.

Dashed lines Eqn.3.34. $\alpha\beta=10^2$; $\alpha=10^{-3}, 10^{-2}$.

Dotted lines (Mimkes and Wuttig) $\alpha\beta=10$; $\alpha=10^{-3}, 10^{-2}, 10^{-1}$.

Vertical arrows connect corresponding solutions of Eqn.3.34.and Mimkes and Wuttig's solution.

Q^{II} changes sign at the values of η indicated by short vertical lines at the left of the curves.

$$\frac{d \ln Q^{I}}{d\eta} = \frac{d \ln Q^{II}}{d\eta} = - \frac{A}{(\alpha\beta)^{1/2}} \qquad 3.35.$$

A, which is of the order unity, is a slowly varying function of α with a very weak dependence on $\alpha\beta$. This is illustrated in Figure 3.9 which shows A plotted versus α. The approximations of Smoluchowski, and Mimkes and Wuttig, yield linear tails with slopes given by Equation 3.35, but with quite different values of A. The Smoluchowski values were quite close to the true values, especially at low values of α. The Mimkes and Wuttig values of A differ considerably from the true values, except for $\alpha \geq 1$.

Extrapolation back to $\eta = 0$ the linear portions of the plot in Figure 3.7 intersect the ordinate at values of $\log_{10} Q^{I}_{ex}$, which decrease rapidly with increasing α, but which are nearly independent of $\alpha\beta$ for a given α value. This is illustrated in Figure 3.10 which shows $\log_{10} Q^{I}_{ex}$ plotted versus α. For $\alpha \leq 0.1$, Q^{I}_{ex} is quite well represented by

$$Q^{I}_{ex} = \alpha^{-1.84} \qquad 3.36.$$

As shown in Figure 3.8, the same extrapolation of the Q^{II} plot yields intercepts of $\log_{10} Q^{II}_{ex}$, that depend on both α and $\alpha\beta$. The dependence of $\log_{10} Q^{II}_{ex}$ on α and $\alpha\beta$ is shown in Figure 3.11. Q^{I}_{ex} and Q^{II}_{ex} are connected by the relation

$$Q^{II}_{ex} = \frac{\pi^{1/2} A}{(\alpha\beta)^{1/2}} Q^{I}_{ex} \qquad 3.37.$$

This can be used to obtain Q^{II}_{ex} from values of Q^{I}_{ex} read from Figure 3.10, and values of $A/(\alpha\beta)^{1/2}$ deduced from the tail slope.

Since A is only a weakly dependent function of α, and therefore even more weakly dependent on time, the slopes of dislocation tails, calculated by Equation 3.35, are almost independent of the annealing time. This is in marked contrast with the similar tails, due to fast diffusion down grain boundaries, the slopes of which are proportional to $t^{-1/4}$ (85).

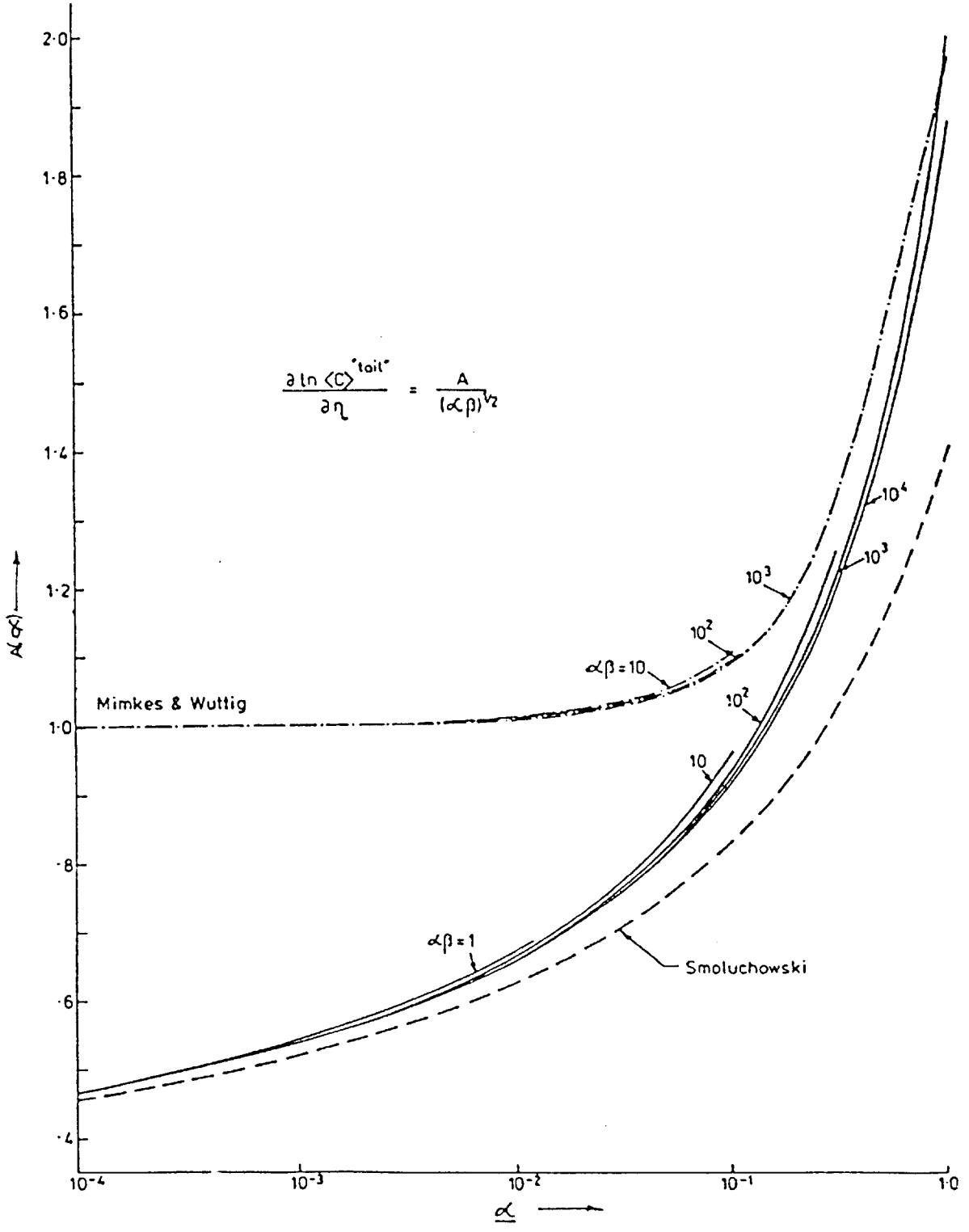


Fig. *3.9.* The quantity A of Eqn. *3.35.* plotted as a function of α for various $\alpha\beta$. [after LeClaire and Rabinovitch [86]]

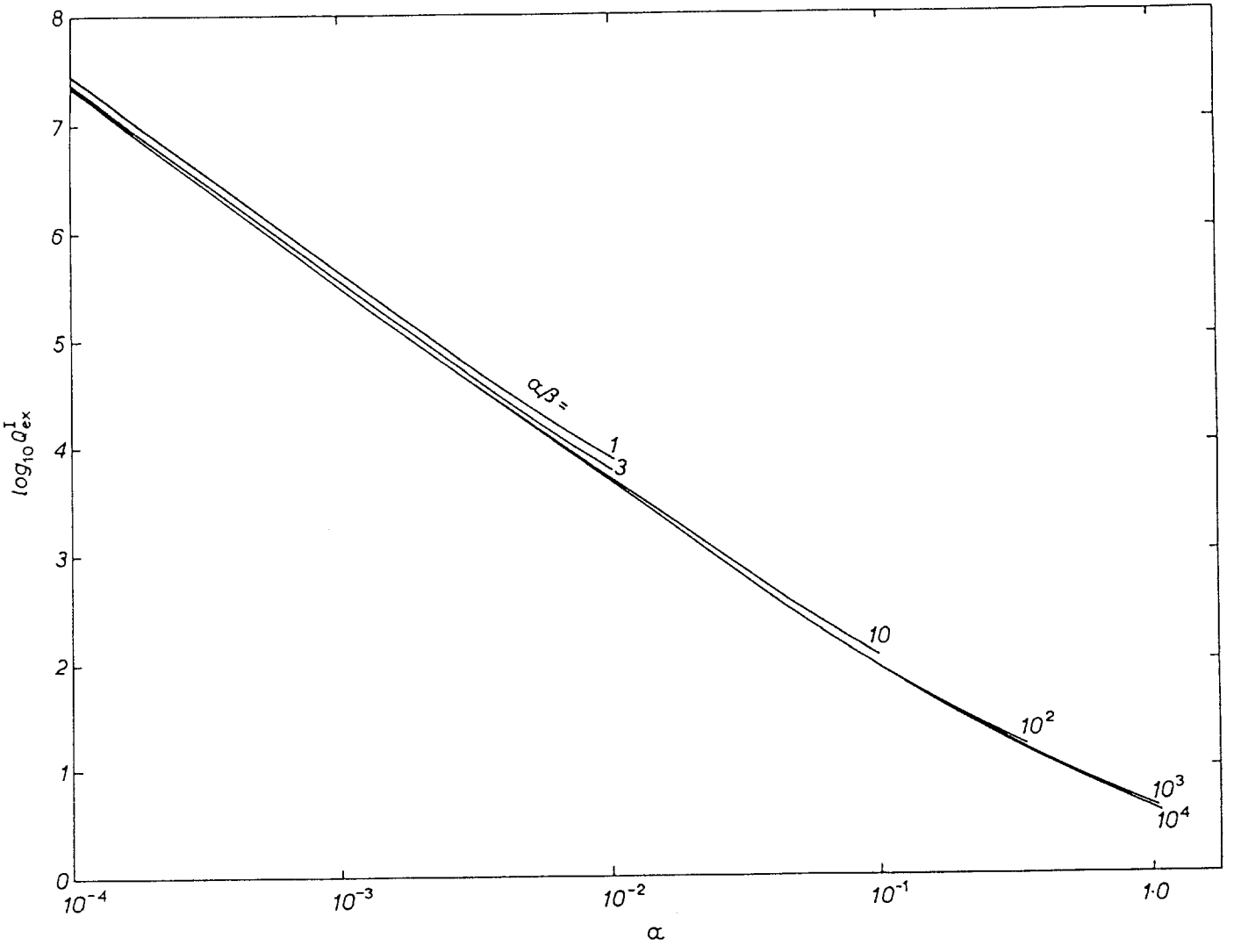


Fig.3.10.The intercept with the ordinate ($\eta = 0$) of the backward extrapolation of the linear tail of $\log_{10} Q^I$ versus η [after LeClaire and Rabinovitch[86]]

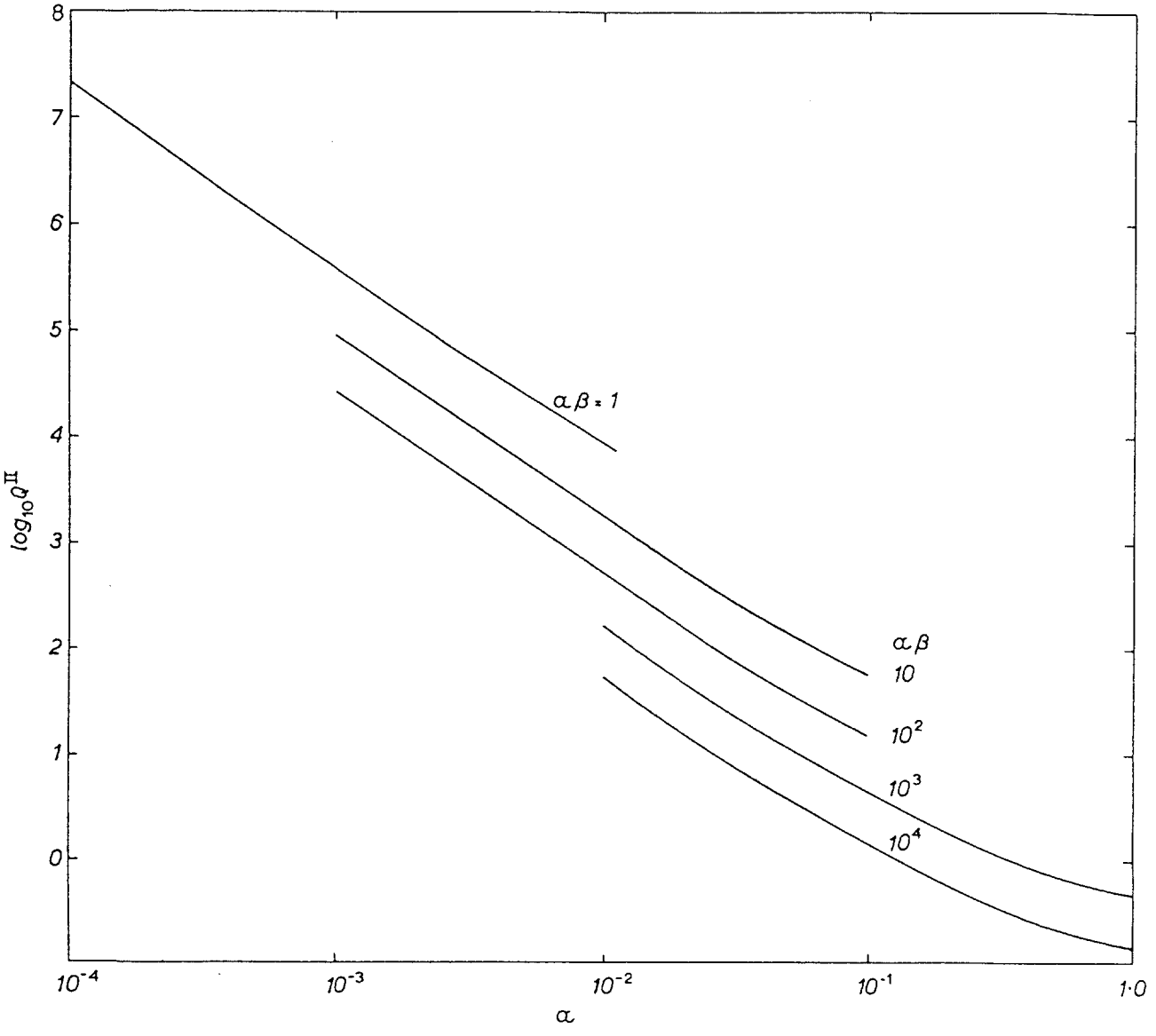


Fig.3.11. The intercept with the ordinate ($\eta = 0$) of the backward extrapolation of the linear tail of $\log_{10} Q^{II}$ versus η [after LeClaire and Rabinovitch[86]]

Thus, measurements of the slope as a function of time provide a means of distinguishing experimentally between tails due to diffusion down isolated and independently acting dislocations, and tails due to diffusion down dislocations closely arrayed into boundaries or walls. The $t^{-1/4}$ dependence for boundary tails has been observed (119). There is no reported evidence as yet that the slopes of tails due to isolated dislocations are time independent.

Δ is determined from the slope of the tail once a is known, but obviously the result depends strongly on what value is used for a. However, since A depends only weakly on a, the quantity $(\Delta-1)a^2$ or $(\alpha\beta)^{1/2}$ in Equation 3.35 can be determined with much less uncertainty than Δ alone, e.g. an uncertainty of 10^2 in α about a mean value of 10^{-3} provides an uncertainty factor of only ~ 2 in $(\Delta-1)a^2$.

In principle, a could be determined from the intercept with the ordinate of the back-extrapolated tail, provided the dislocation density is known. LeClaire and Rabinovitch (86) have demonstrated the fact, using Equation 3.31

$$\text{I} \quad C^{I}_{int} = C(0)\ \varepsilon^2\ Q^{I}_{ex} \qquad 3.38.$$

where $C(0)$ $(= C_o)$ is the measured concentration at $y = 0$. Using Equation 3.36 and recalling that $\varepsilon^2 = \pi a^2 \rho$

$$a^{I} = \left[\frac{C^{I}_{int}/C(0)}{\pi\rho(Dt)^{.92}}\right]^{6.25} \qquad 3.39.$$

Similarly, $$\text{II} \quad C^{II}_{int} = C(0)\ \varepsilon^2\ Q^{II}_{ex} \qquad 3.40.$$

and

$$a^{II} = \left[\frac{C^{II}_{int}/C(0)}{\pi^{3/2}\ \rho(Dt)^{1.42}(d\ln C/dy)_{tail}}\right]^{6.25} \qquad 3.41.$$

where now $C(0) = \gamma/(\pi Dt)^{1/2}$

Obviously, because of the 6.25 index in Equations 3.39 and 3.41, a is very sensitive to errors in the parameters from which it is calculated.

The concentration ratio, the tail gradient and Dt can all, in favourable circumstances, be determined to within a few per cent, so that errors may not be too important. However, equally reliable values for dislocation densities are more difficult to obtain. An underestimated ρ will give rise to an overestimated a, and this effect can be pronounced. For example, if ρ is underestimated by a factor of 3 because of etching inefficiency, the deduced value of a would be nearly 10^3 times larger than the true value.

Rearranging Equation 3.39 in case I, provides an estimate of ρ which will be relatively insensitive to the value assumed for a. This is represented as

$$\rho^I = \frac{C^I_{int}/C(0)}{\pi a^{0.16}(Dt)^{0.92}} \qquad 3.42.$$

Even a 10^2 uncertainty in a of Equation 3.42 makes ρ uncertain by only a factor of 2. The same conclusions follow from a similar relation for ρ^{II} obtained from Equation 3.41.

3.3. Results of Dislocations Enhanced Diffusions

A large number of experiments have established beyond doubt the existence of enhanced diffusion along grain boundaries in metals. However, various authors have reached different conclusions using similar experiments on alkali halides. Isolated dislocation pipe diffusion has not been the subject of much study.

Klotsman et al (77) reported that there was no evidence of preferential grain boundary diffusion of cations and anions in alkali halide crystals. Barr and his co-workers (10) observed that there was enhancement of anion grain boundary diffusion, and that a decrease in the dislocation density reduces the anion diffusion coefficient but increases its apparent activation energy. These systems behaved as if they were homogeneous and the diffusion followed the kinetics of simple bulk diffusion as in Hart's model. This boundary diffusion enhancement was also noted by Cabane (24,25)

in his work on polycrystals, but only in the presence of hydroxyl ions. No enhanced cation grain boundary diffusion was detected in alkali halides by Hoodless (64) and Laurent and Benard (80, 81). Riggs and Wuttig (108) observed a distinct enhancement of cation grain boundary diffusion in the presence of hydroxyl ions from NaOH. They suggested that the hydroxyl ions which diffused rapidly down the boundary might change the structure, and/or the potential of the boundary thus facilitating cation diffusion. Tucker et al (122) claimed to demonstrate the existence of dislocation pipe diffusion, based on the extra conductivity produced by Na^+ ions injected by an electric field into LiF in the vicinity of the dislocations. They reported the activation energy for such fast transport was 0.31 eV and suggested that the rapid diffusion was aided by a complex mush of cation vacancies with interesting charge effects at the dislocation cores. Moment (99) later observed fast Na^+ motion in LiF grain boundaries over a similar extrinsic temperature range. He reported that the activation energy of the process was 0.32 eV and was independent of the grain misorientations from 4° - 53°. The activation energy value was in good agreement with Tucker. The independence of the activation energy from the angle of misorientation in the range of 9° - 28° was also previously observed by Turnbull and Hoffman (123) in their study of enhanced self-diffusion of silver in bicrystal of the element. Yukawa (134) and Upthegrove (124), however, reported in their similar study that there was a marked increase in Q' for lower values of θ. Fisher's equation was used to obtain these results. However, further analysis of these results in terms of Whipple's solution would lead to a value of Q' less than those reported, which, in all probability, would produce Q's comparatively independent of θ.

Harris (57) studied Na^+ diffusion along grain boundaries in sodium chloride at various diffusion times but at a fixed temperature of 360°C .

He observed that the enhancement of the cation diffusion down the boundaries was not due to the hydroxyl ions as suggested by Riggs and Wuttig (108), but because of compositional inhomogeneities resulting from crystal growth. These inhomogeneities exist in pure crystals, and are difficult to remove even with prolonged annealing near the melting point (2). The impurities would, in general, be attracted by the boundaries in the crystals. Harris suggested that diffusion was promoted in broad regions containing precipitate-matrix interfaces, by local phase change disorder. He indicated that such enhancement would be observed provided the condition $(Dt)^{1/2} << \delta$ is satisfied, where δ is the average distance of these regions. The diffusion features would then follow the kinetics of the type C of Harrison's model (60). When $(Dt)^{1/2} \sim \delta$, or the diffusion time is long the lattice contribution is sizeable and these fast substructure components would be far less obvious. Using light-scattering method, Harris (58) supported his suggestion of the presence of microscopic impurities in the crystal boundaries. However, a careful study of this work shows that the diffusion temperature of 360°C is much higher than the impurity dissolution temperature of the system, which suggests that the observed boundary diffusion enhancement was not due to any residual impurities.

Geguzin and Dobrovinskaya (42) studied the self-diffusion of Na^+ along edge and screw dislocations in plastically deformed sodium chloride single crystals at 200 - 540°C. The models of Hart and Smoluchowski were separately applied to analyse the results and similar activation energies of fast diffusion were obtained, i.e. 0.61 eV and 1.1 eV, for edge and screw dislocation diffusion, compared to a corresponding activation energy of 1.8 eV for bulk diffusion. Geguzin and Dobrovinskaya suggested that the low activation energy for edge type dislocation diffusion compared with screw, is due to the dislocation tubes being more deformed in the former case. In later experiments (43), they found that

the activation energy of Na^+ diffusion along the grain boundaries of a NaCl bicrystal was 0.62 eV which compares well with the corresponding energy for edge dislocation diffusion. They concluded that the fundamental diffusion processes were similar and involved the jumping of atoms into adjacent vacant sites. Schlederer (112) revealed that the activation energy of Na^+ diffusion along dislocations in NaCl was 0.4 eV with a corresponding bulk diffusion energy of 1.23 eV. However, there is not sufficient information from his work to enable a comparison of his results with other literature.

Mimkes (94) reported the conditions for the observation of cation diffusion along an isolated dislocation pipe in the form of:

$$To = \frac{H_f}{S_f - K \ln n} \qquad 3.43.$$

where n is the concentration of vacancies due to aliovalent cation impurities. T_o is the temperature above which only intrinsic diffusion is observed. In order to observe enhanced cation dislocation diffusion in the intrinsic range, the lower boundary of the normalised intrinsic range

$$1 = Tm/Tm \geq T/Tm \geq To/Tm$$

must be as low as possible where Tm is the melting temperature of the ionic crystal. In alkali halides, To is about 70% of Tm and thus enhanced diffusion of cations along dislocations in the intrinsic range will most probably be obscured by extrinsic diffusion. In order to observe an enhanced dislocation pipe diffusion, he suggested that a very low temperature in the extrinsic range of pure crystals, $n < 1$ ppm, has to be chosen. In this temperature range, impurity-vacancy dipoles are formed, yielding a higher activation enthalpy of diffusion than in the impurity-controlled range. Since anion diffusion is not affected in the same way as cationic diffusion by the presence of aliovalent cation impurities, enhanced diffusion of anions along dislocations may be more readily observed.

In the proposed solutions for grain boundary and isolated dislocation diffusion, the values of the corresponding diffusion coefficient, D' and D_d, and the width of their fast diffusion path, δ and a, are inseparable, and only the value of the products $D'\delta$ and $D_d a^2$ are obtained. In order to obtain the values of D' and D_d, it is necessary to estimate the dimension of their diffusion paths. It is generally accepted that δ in metals is around 5Å. However, the dimension of δ in ionic crystals is still a matter of dispute.

In recent years, many papers have discussed solute segregation at, and in the viscinity of, grain boundaries and dislocations, which in turn, should lead to a space-charge or defect layer similar to that proposed by Lehovec (87) at the surface of alkali halide crystals due to their ionic nature. Eshelby et al (34) also proposed that grain boundaries and dislocations should be charged, and surrounded by a balancing layer of charge. Therefore, an effective grain boundary width, or isolated dislocation path for diffusion includes both the area of misfit at this disordered region plus the space-charge region around it. In alkali halides, the space-charge layer may extend, to a significant distance, into the 'good' lattice and decrease rapidly with temperature, and decrease with the addition of aliovalent impurities.

In their diffusion studies of sodium chloride, Barr et al (10) suggested that the effective radius of the dislocation core at 440°C was 200Å. However, Harrison (65) believed that a was underestimated, and that the space charge should be more than 200Å if the type A diffusion conditions set for the experiment were to be valid. In their boundary diffusion studies of MgO, Wuensch and Vasilos (132) suggested that δ was of the orders of microns. Mistler and Coble (96) in their studies of sodium chloride at 700°C reported a diffusion boundary width of 1 μm which is in close agreement with the value reported by Harris (57). In 1977, Yan et al (133) made an extensive study of the space charge

effect of grain boundary diffusion. The reported values of δ for sodium chloride were around 80Å at 900°K and 2000Å at 600°K. They further suggested that the value of $\delta \sim 1$ μm at 600°K was valid only when the divalent impurity concentration < 0.01 ppm which is practically unlikely to happen.

CHAPTER FOUR

EXPERIMENTAL TECHNIQUES

4.1. Crystal Growth

4.1.1. Purification of starting material

The transport properties of sodium chloride depend sensitively on impurities. Thus high purity single crystals are required so as to reduce the extrinsic effects of impurity.

The starting material for crystal growth in this project was an ultra-pure grade of sodium chloride obtained from Hopkins and Williams Chemical Ltd. This starting material contained a variety of aliovalent cation and anion impurities, and the overall impurity level varied slightly from batch to batch. The most common divalent cation impurities in sodium chloride are calcium and magnesium. A total cation impurity content of < 5 ppm was claimed by the manufacturer for the as-received sodium chloride used in this study. Various methods of cation purification were considered, but subsequently rejected. For example, zone-refining cannot be used effectively to remove calcium ions, as the partition coefficient between the solid and melt for Ca^{++} is close to unity. Ion exchange and solvent extraction techniques were rejected, since contamination occurs during the complex handling procedures employed. Thus, there was no purification of the as-received sodium chloride. However, replicas of specimens taken from the grown crystals used in diffusion experiments were eventually analysed for Ca^{++} and Mg^{++} contents. Atomic absorption spectroscopy was employed, having a detection limit of < 0.1 ppm for favourable elements. A conductivity method was also used to determine the total aliovalent cation impurity level. The results of these analysis will be presented in the next chapter.

The major source of anion impurity in sodium chloride is the hydroxyl ion which hydrolyses the salt at high temperatures. To reverse the hydrolysis, Butler et al (23) bubbled chlorine, hydrogen chloride, or phosgene gas through the melt. However, the use of any one of these

corrosive gases combined with the molten salt required elaborate safety precautions and complex apparatus. Argarwal and Kulshreshtta (5) found that the concentration of hydroxyl ions was effectively reduced by purging the melt with dry nitrogen gas. Further, Etzel and Patterson (36) have shown that crystals grown from a melt contained in a silica or quartz beaker had a reduced level of hydroxyl ions, compared with those grown in platinum or gold containers, which might imply some gettering action of the silica for hydroxyl ions. In the present work, silica beakers were used for crystal growth, the salt was preheated in a vacuum at 500°C for 12 hours prior to melting and the system was periodically flushed with dry nitrogen, in order to remove any water, and volatile impurities.

Just prior to being used for crystal growth, the silica beakers were treated with a mixture of 1 part HF/10 parts concentrate HNO_3 for half an hour, washed thoroughly with distilled water, and finally dried in an oven at 120°C for an hour.

4.1.2. Growth of crystals

Sodium chloride crystals were grown in a dry nitrogen atmosphere using the Kyropolos method which has been described by many previous workers.

Figure 4.1. shows the basic design of the rig employed for crystal growth, and Figure 4.2. illustrates by means of a schematic drawing, the modifications made for the present work. During crystal growth, sodium chloride vapour condenses on the walls of the transparent silica tubes that encloses the beaker of molten salt, and reduces visibility. The system was modified, to improve visibility by incorporating a viewing tube with an adjustable window, as shown in Figure 4.2. Crystals were grown in a system sealed by stainless steel and glass end plates against water-cooled 'O' ring seals. Hot sodium chloride fumes passed to a cooling jacket and subsequently to a bubbler containing liquid paraffin.

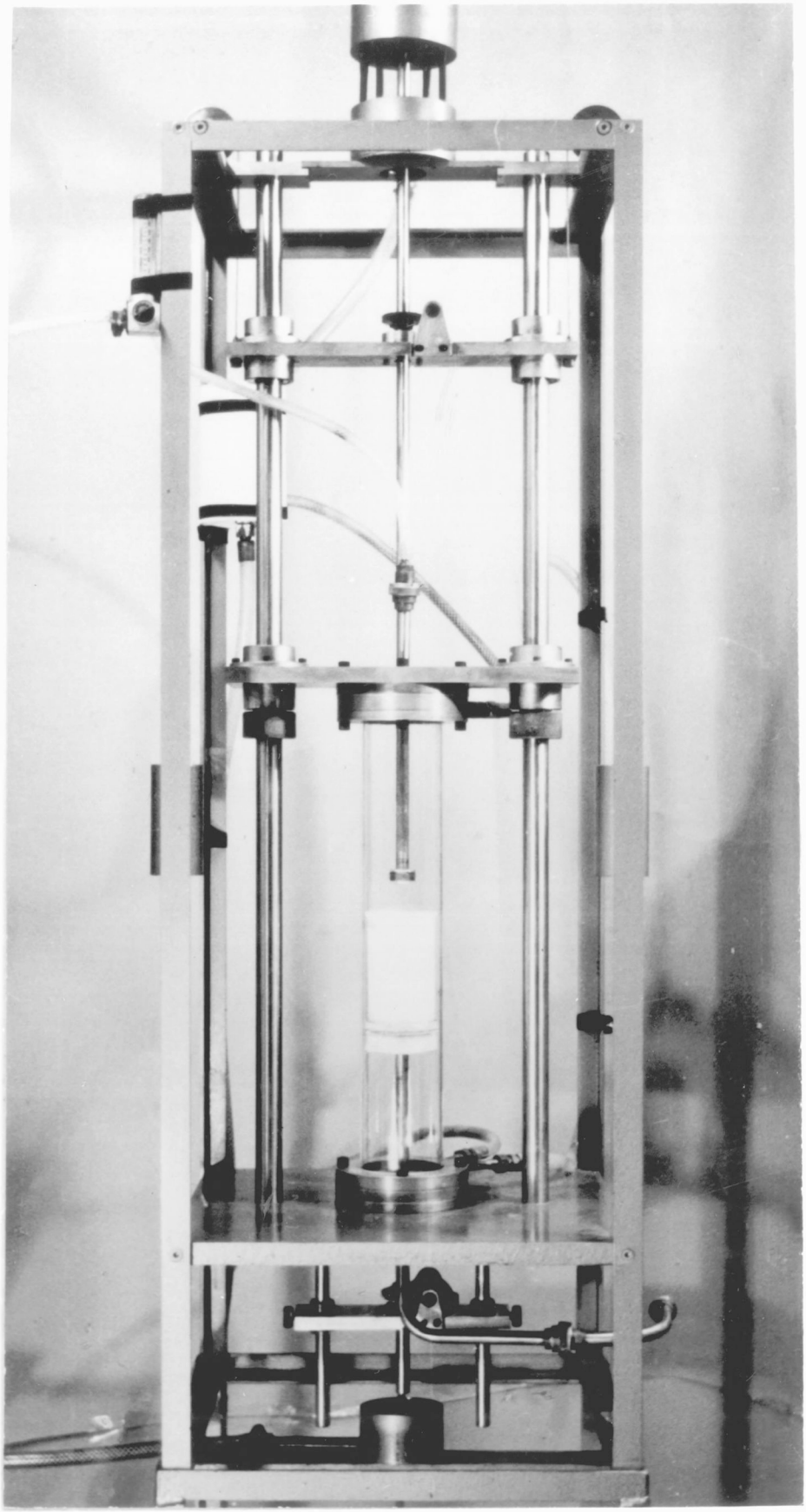


Fig. 4.1. Crystal growing apparatus.

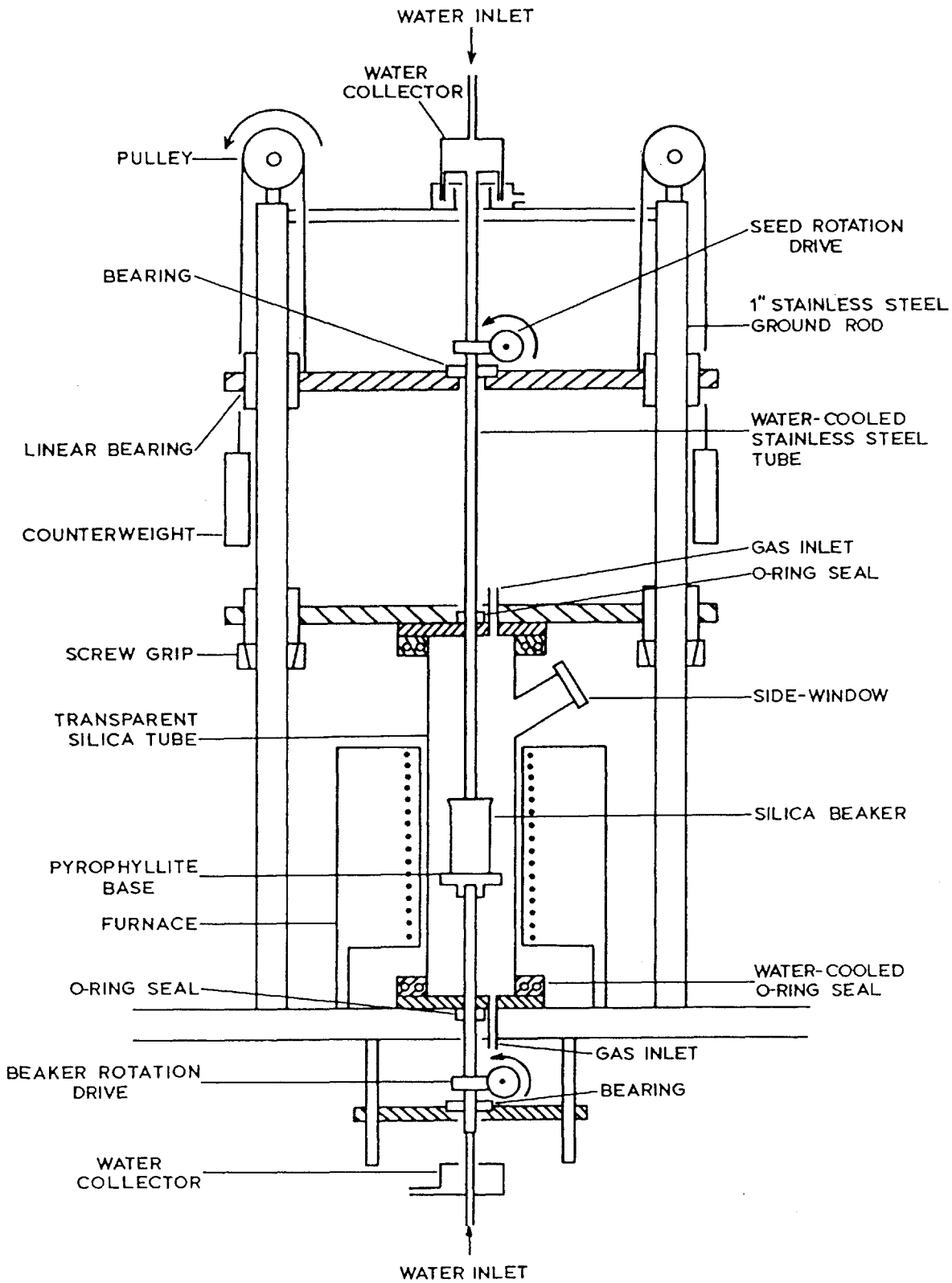


Fig.4.2. The crystal growing apparatus.

The extraction line was detachable so that sodium chloride condensed on the walls of the system could be readily removed.

The as-grown sodium chloride single-crystals were annealed at 650°C for 24 hours, and slowly cooled to room temperature at the rate of 15°C per hour, in a dry nitrogen atmosphere before being stored in vacuum-desiccators until required for use.

4.2. Bending and Polygonisation

Different dislocation densities were introduced into the well-annealed specimens using the four-point bending technique. Four-point bending was used in preference to three-point bending, because in the latter case, the maximum stress, and hence the initial slip, occurs in the region immediately below the central loading point. The specimens were then annealed at high temperature to align the dislocations into low angle boundaries, with a suitably wide-spacing between dislocations along the boundaries.

4.2.1. Preparation of specimens

Specimens were cleaved from the crystal boule along the (100) planes. The typical beam size used for 4-point bending was 6 x 1 x 1 cms, and was governed by the size requirement of the diffusion specimens subsequently obtained from the beams. Although limited in number, only the beams free of obvious surface flaws were used for subsequent experiments, the rest were rejected.

Sodium chloride crystals are brittle when surface microcracks are present, a feature common to most specimens. These microcracks or secondary cracks form normal to the main crack as it propagated through the crystal during cleavage. The number and size of the secondary cracks are dependent on cleavage velocity. When a load is applied to a micro-cracked specimen, stress concentrations produced at the tips of the cracks cause catastrophic failure before any gross plastic deformation

can take place. Stokes et al (120) noticed that the ductility of a crystal is increased if such surface flaws are removed by chemical polishing. Hobbs (63) has found that polar solvents with affinities for alkali halides in the range 0.5 to 1.5 g halide/100 g solvent, produce the best polishing at reasonable rates. In the present work, specimens were polished using a 50/50 mixture of methanol and ethanol, and immediately and thoroughly washed with dry diethyl ether. The latter appears to remove any surface deposit of alcohol saturated with sodium chloride, which may cause re-embrittlement of the specimens on drying. With efficient polishing and drying the specimen surfaces appeared almost featureless under the microscope. After polishing, the specimens were stored in vacuum-desiccators until required, remaining ductile for prolonged periods in dry air. Gloves were always used during specimen handling to avoid surface contamination from the hands.

4.2.2. Four-point bending

A standard Instron Model Testing Machine was used in bending the specimens by compression. A travelling microscope with cross polars was fixed to the cross-head of the Instron and adjusted until the development of the cross birefringence of the specimen during bending could be observed directly. A load of 20 kg and cross-head speed of 0.01 mm per minute was used for most of the bend tests, being conditions suitable for providing a slow enough strain rate to attain a desired amount of deformation.

The specimen was positioned in the four-point bending jig with its long axis perpendicular to the knife-edges. The system of rectangular co-ordinate axes was located so that the origin O was in the neutral axis of the beam midway between the inner knife-edges, (see Figure 4.3).

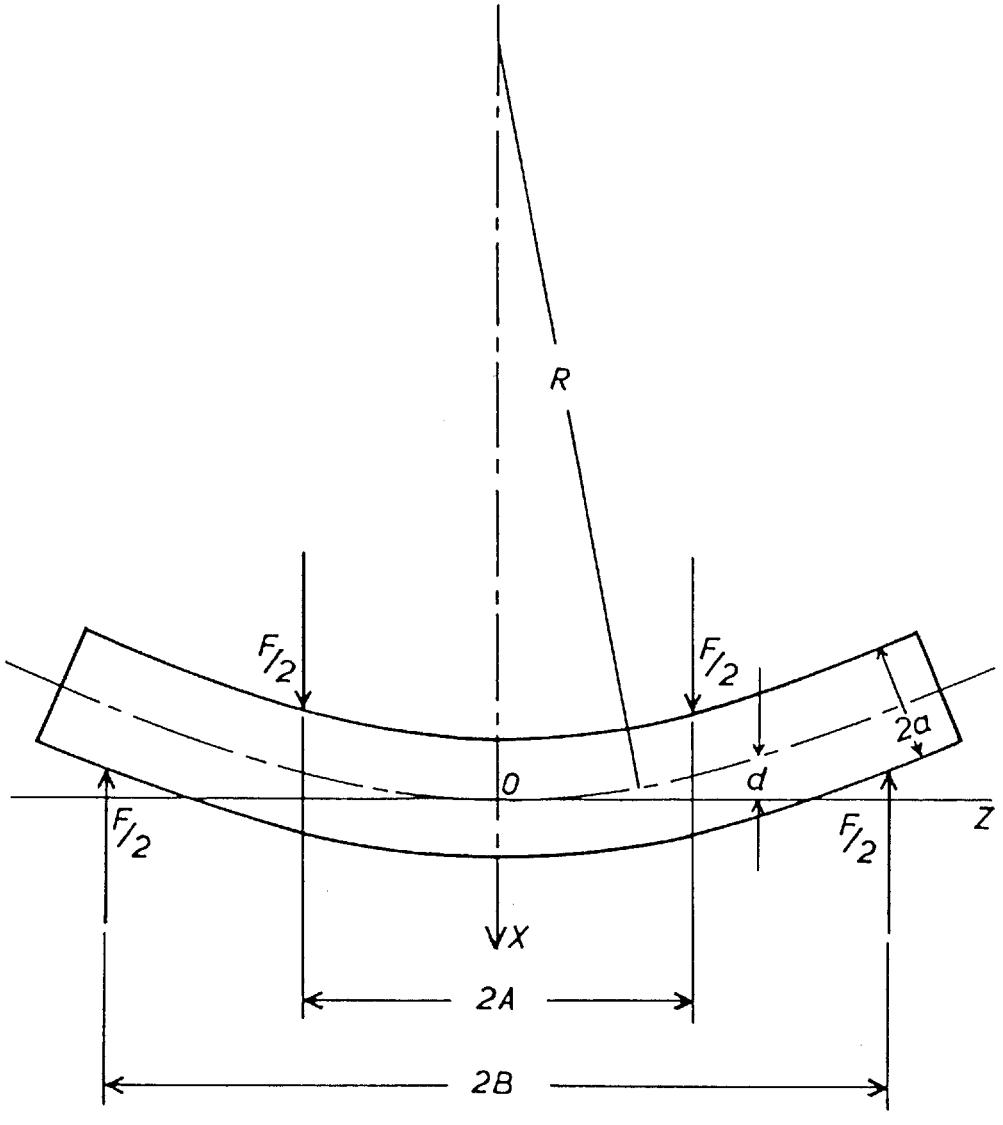


Fig.4.3. Schematic diagram of a beam undergoing four-point bending.

The distance between the two inner knife-edges, 2A, was 15 mm and the distance between the two outer edges, 2B was 50 mm. A maximum, even bending moment should be experienced over the region 2A.

The record produced by the Instron machine was a graph of applied load versus the displacement of the inner knife-edges is shown in Figure 4.4. The strain in the beam was calculated using the beam equations of Timoshenko shown below.

$$\varepsilon = a/R = \frac{a\,D}{[A(B-A) + (B-A)^2/3 + 4a^2/3]} \qquad 4.1.$$

where ε is the outer fibre strain, R is the radius of curvature of the central portion of the beam and D is the displacement of the inner knife-edges relative to the outer knife-edges. This equation becomes invalided once the beam starts to deform plastically since the stress at any point in the beam now becomes a more complicated function of both the load, and the stress necessary to nucleate and to move dislocations. At stresses above the flow stress, therefore, the bending curves should be recorded as plots of strain versus the ratio of applied load and the load at flow. However, reasonably accurate calculations of the outer fibre strain can be made, for strains < 5%, by applying the simple beam equation above. The error involved in such a low strain range proved to be insignificant.

During bending, the applied load should initially be in contact with all four knife-edges. A useful and convenient check on bend testing was to determine the Young's modulus, E, in the elastic region of the deformation.

Specimens in the present work were loaded to attain strains of 0.1%, 0.2% and 0.3%, and the portions of the specimens outside the two inner knife-edges were cleaved away. Stress birefringences in the remaining centre positions was observed under cross polaroids in the direction parallel to the bending axis X. The specimens were then stored for subsequent polygonisation.

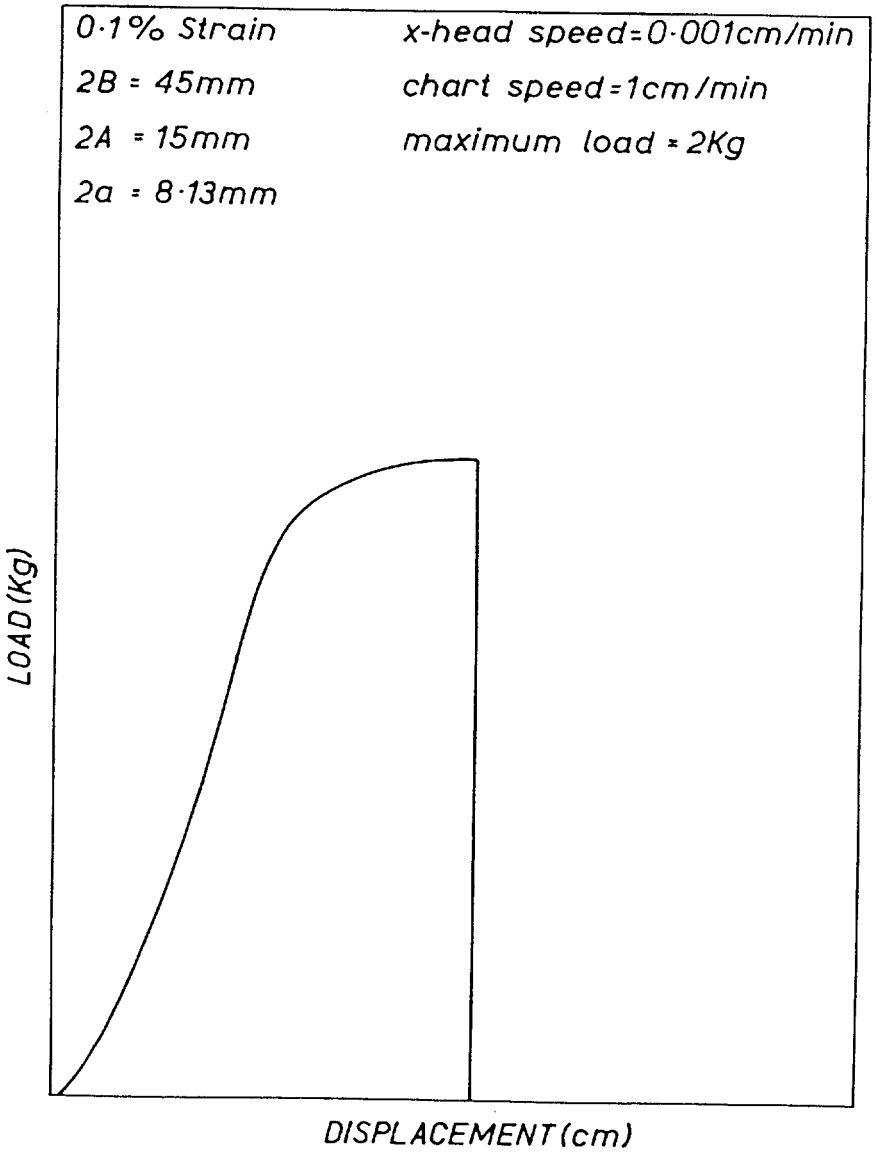


Fig.4.4. Typical load-displacement curve for NaCl in four-point bending.

4.2.3. Polygonisation of bent specimens

A plastically deformed specimen is under internal strain which can be observed by its birefringence pattern. Dislocations are mobile particularly at high temperature. The driving force for these movements comes from the strain energy of the dislocations. Dislocations of opposite sign tend to annihilate each other when they coincide. The remaining dislocations then rearrange themselves into groupings of minimum energy, taking the form of sub-boundaries within the crystal. This type of recovery behaviour is called polygonisation and is illustrated in Figure 4.5. Screw dislocations move by the mechanism of slip and cross-slip. Edge dislocations move by slip and climb, the latter being a diffusion controlled process which involves the movement of vacancies to or from the ends of the half planes. Thus, the rate of polygonisation increases rapidly with temperature. After the dislocations have dissociated themselves from the slip planes and become aligned in low angle boundaries, the next stage is a coalescence of the low-angle boundaries, as two or more boundaries combine to form a single boundary. As a result of this combination the dislocation density in each boundary immediately after coalescence is increased, and the polygon walls become more widely separated and approximately parallel. The slip planes in NaCl crystals are the (110) planes. When such a polygonised specimen is chemically etched, parallel dislocation walls lying at approximately 45° to the surface will be observed on the plane of the specimen perpendicular to the bending axis.

In the present work, specimens previously deformed by four-point bending were used for the polygonisation treatment. The typical size of such a specimen is 1 x 1 x 1 cm, and the polygonisation temperatures used were 600°C, 650°C and 700°C, with the polygonisation time ranging from 1 to 2 hours. The temperature and duration of polygonisation were selected so as to obtain a stable microstructure which would not change

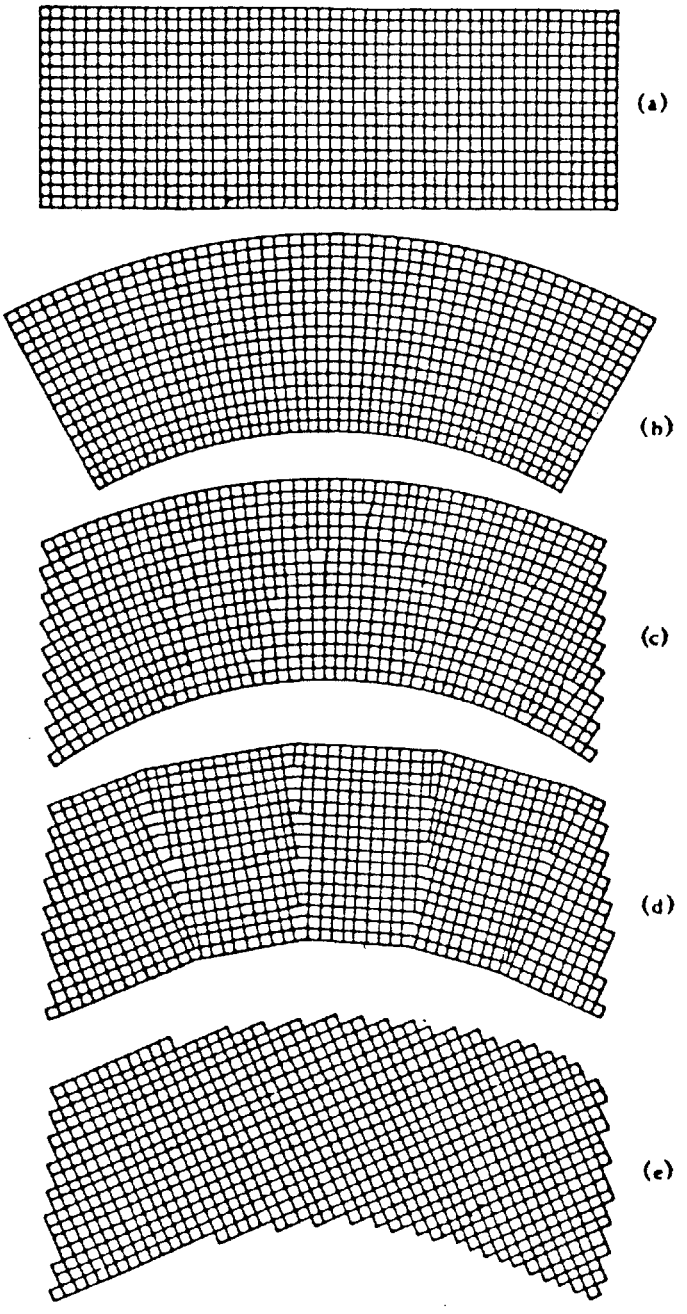


Fig.4.5. Five states of a single crystal. (a) Unstrained. (b) Elastically bent. (c) Plastically bent. (d) Polygonized. (e) Recrystallized.

in subsequent diffusion anneal. The furnace used for such heat treatment has a temperature gradient of not more than 1°C across the diameter of the furnace tube when the specimen was placed at the central region of the furnace. In the situation of short polygonisation time, it is essential for the specimen to attain its thermal equilibrium in the shortest period of time. It was noted that the temperature reached a steady value in less than 5 minutes. After polygonisation, the specimens were left to cool to room temperature in the furnace. The polygonised specimens were then stored in a vacuum desiccator and ready for its subsequent chemical etching.

4.3. Chemical Etching and Dislocation Density Counting

If a crystal containing dislocations is subjected to an environment which removes atoms from the surface, the rate of removal of atoms around the point at which a dislocation emerges at the surface may be different from that for the surrounding matrix, resulting in the formation of pits. The driving force for such preferential 'etching' arises from the lattice distortion and the strain field of the dislocation.

In the present work, chemical etching was used to reveal the dislocation networks on the surface of polygonised specimens. The etchant selected for this purpose consisted of one part anhydrous methanol to two parts glacial acetic acid. Specimens were dipped for 5 to 10 seconds in the etchant before being thoroughly rinsed in dry diethyl ether and blow-dried in air. The ratio of the solvents used, and the etching time varied slightly from day to day. A sample being sacrificed beforehand to establish the conditions necessary for most efficient etching. After etching each batch of a few specimens, the reagents, especially the rinses, were discarded and fresh samples were obtained.

A clean specimen surface is essential to obtain a good etch-pit pattern. The surface features of a specimen which has been previously

chemically treated, tends to lose sharp contrast. A plastically deformed and polygonised specimen was cleaved into two halves. The freshly cleaved surface of one half was immediately etched, whilst the other half was retained for subsequent diffusion experiments. Special care was taken to minimise deformation of the specimen during cleaving. A very thin specimen tends to buckle slightly during cleaving, and the damage can be extensive unless cleavage is rapid. (See Discussion chapter.)

Etch pits are best viewed in oblique reflected light, because contrast effects are produced between the facets of the pits and the surrounding surface. Etch pits formed at freshly introduced dislocations have the form of a square pyramid with the base edges in <100> directions and the apex of the pit sited at the line of the dislocation.

4.4. Radiation Work

A thin layer of tracer was vacuum-evaporated onto the surface of a specimen that has previously been microtomed flat. It was sealed and diffusion-annealed. Slices were then microtomed from the diffusion surface of the specimen and weighed in order to determine the thickness of the slices. These were then dissolved in the scintillator and the amount of radioactivity was counted in a radiation counter. The radiation work in the above procedures will be described below and the microtoming and weighing will be described in the next section.

4.4.1. Use of tracer

Na^{22} obtained from the Radiochemical Centre of Amersham was used as tracer in the diffusion sectioning experiments of the present work. The total nuclidic impurity was less than 50 ppm, and less than 10 ppm for any single nuclide. The high radiochemical purity content was essential since Mitchell and Lazarus (97) reported that there is a significant codiffusion of heterovalent impurities with the monovalent tracer in ionic crystals. The carrier-free Na^{22} is in the form of

sodium chloride in aqueous solution which has a radioactive concentration of 200 μCi/ml.

Na^{22} has a half-life of 2.6 years and thus the loss of its specific activity is negligible even during a prolonged diffusion anneal of a month. It disintegrates with the transition probability of 90% by positron emission. These positive beta particles are light and have a continuous spectrum of energy up to a maximum value of 0.546 MeV. Positrons disappear rapidly by annihilation with electrons, and the liberation of energy of 1.275 MeV which appears as photons. These photons are considered as secondary gamma rays rather than those resulting from direct disintegration.

4.4.2. Vacuum-evaporation of tracer

An Edwards 306 Vacuum Coater was used to evaporate the tracer on to the NaCl diffusion surface. A photograph of the equipment is shown in Figure 4.6.

$Na^{22}Cl$ in aqueous solution was dispensed on the central crucible of a molybdenum boat using a Hamilton microsyringe, the syringe having a capacity of 50 μl. The accuracy of dispensation was regularly calibrated by weighing a dispensed amount of distilled water. The molybdenum boat was placed inside an aluminium box which rested on a hot plate at a temperature of 50°C. Tracer solution in 30 μl amounts was dispensed on to the crucible of the boat. This was left to dry in the warm draught allowed to pass through the box. When the tracer had dried, the procedure was repeated until the total amount of tracer solution dispensed was 200 μl.

The molybdenum boat was then clamped on to the two flexible filament holders of the evaporator, which could be adjusted until a position for central evaporation of the tracer was achieved. A brass plate with a central square-hole was mounted just above the molybdenum boat as shown



Fig. 4.6. Edward 306 vacuum-coater.

in Figure 4.7. The size of the hole was 1.2 x 1.2 cms and determined the area of tracer deposition. Two similar plates with hole dimensions of 1 x 1 cms and 0.8 x 0.8 cms had been used for specimens with smaller surface area for diffusion. The duplicate cleaved face to that examined in the etching experiments was previously microtomed (see microtoming section) to give a flat plane for tracer deposition, and was carefully placed on the brass plate with the microtomed surface covering the square opening of the plate. The specimen was then covered by a petri dish, and care was taken to ensure that the microtomed surface and the molybdenum boat were parallel and the crucible of the boat was centrally positioned below the hole of the brass plate. The vertical distance between the crucible and the specimen surface was adjustable but was usually set at 0.9 to 0.8 cm. The relative positions of the components were important in establishing the conditions for optimum efficiency of evaporation (see Appendix I).

The evaporating system was then sealed from the atmosphere and was pumped overnight until a vacuum of 10^{-7} torr was attained. The variable transformer of the evaporator was then slowly rotated to a setting giving a current just below the evaporation current, but sufficiently high to outgas the source. The current was then slowly increased until the vacuum was affected suggesting that vaporisation of the source was commencing. This point was usually reached when the molybdenum boat just began to turn dull red. Tracer deposition then continued for 15 minutes, after which a 30 second burst of current was applied to drive off any remaining tracer in the molybdenum boat. After allowing the system to cool under vacuum, then switching off the pumps, air was then leaked into the unit and the tracer-coated specimen was removed.



Fig. 4.7. Close up view of the radioactive tracer evaporating unit.

4.4.3. Diffusion annealing

A tracer coated specimen was sandwiched by two parallel thin quartz plates and completely wrapped in a thin platinum sheet. This 'package' was then sealed into the pyrex capsule after evacuation, and flushing with argon, and finally maintaining an argon pressure of 250 mm Hg. The capsule was made sufficiently long to ensure that no excessive heating of the specimen occurred during the sealing operation. A hook was incorporated into the sealed capsule so that the capsule could be suspended in the diffusion furnace.

The crystal growing apparatus shown in Figure 4.2. was used, with slight modification, for diffusion annealing. The jig that held the crystal seed during crystal growth was replaced by a stainless steel tube encircling a pair of chromel-alumel thermocouples, and sealed against the external atmosphere using 'O' rings. By sliding the stainless steel tube through the O-ring seal, the position of the thermocouples could be adjusted and the temperature difference across the horizontal distance of 1 cm at any height could be measured.

Using the side window of the quartz tube, the capsule was lowered into the hot zone of the furnace preset to a required temperature for diffusion annealing. The system was then sealed and evacuated, with the vacuum being maintained throughout the diffusion anneal. The temperature inside the system was found to come rapidly to equilibrium. The heat-up time of the specimen was short which was an important factor when short annealing times were employed. The temperature variation at the mid-region of the furnace was less than 1°C over the period of diffusion anneal, and the temperature gradient across the diameter of the furnace tube was less than 1°C per cm. The vertical temperature gradient was less than 2°C over a distance of 1 cm above and below the position of the specimen.

Annealing time ranged from 5 ½ hours at 506°C to 42 days at 374°C, with checks being made on the temperature at least 3 times per day. When the diffusion anneal was complete, the capsule was taken out from the furnace and cooled to room temperature in air. The specimen was then removed and stored in a vacuum-desiccator for subsequent microtoming and radiation counting.

4.4.4. Use of scintillator and radiation counter

Ionising radiations of the positrons in Na^{22} cause the scintillator to emit light. The light from each emission falls on the electrode of the photomultiplier tube of the scintillation counter. Electron emissions by the photo-electric effect were then recorded as pulses in the counter.

The liquid scintillation counting method was used in the present work, since it produces a higher counting efficiency than the other methods available. This is particularly important in counting samples of low activity at deep diffusion penetration. Liquid scintillator Unisolve 294 was obtained from Koch-Light Laboratories Ltd; and is a high performance general purpose emulsifying scintillator based on pseudocumene (1, 2, 4-trimethylbenzene) as solvent. 10 ml of the scintillator can take up to 1.8 ml of water or 2.1 ml of 1 M NaCl solution at 20°C. Solutions are stable at temperatures as high as 35°C and can be retained in good use for a lengthy period when stored in a cool dark place. The counting efficiency of Na^{22} using this scintillator was found to be as high as 72.4% (see Appendix II).

Polyethylene scintillation vials were used instead of glass vials to avoid the ion-exchange process between the tracer and the glass. A volume of 10 ml of the scintillator and 0.5 ml of distilled water were carefully pipetted into the vial to dissolve the specimen. Extra care was taken to ensure that the pipette was thoroughly cleaned and dried before use, and the pipette did not make contact with any part of the vial.

This was to avoid the introduction of impurities, and cross contaminations of the specimens. In an array of samples, a habit was developed in pipetting the solution into vials containing samples of ascending order of radioactivity. The prepared vials were then stoppered and shaken to ensure that the specimen was completely dissolved in the scintillator solution.

A Beckman LS-200B liquid scintillation β-particle counter was used to measure the radioactivity of the samples. Samples in their containing vials were loaded onto the automatic conveying belt of the counter, and were left in the closed system for an hour before counting commenced. This procedure was necessary to overcome the effect on the scintillators of being exposed to air during handling. A standard of known radioactivity and a 'blank' sample of non-radioactive NaCl were used to check the counting efficiency and the background before each assay.

Each sample was counted for a minimum period of 10 minutes. The statistical error of counting was computed as < 1% in samples of low radioactivity and ∿ 0.1% in samples of high activity.

4.5. Microtome - Sectioning

Specimens were sectioned using a modified M.S.E. sledge base biological microtome, which was bolted to a heavy steel table, which, in turn was bolted to a concrete base, as shown in Figures 4.8. and 4.9. The rigidity of the system helped to improve the accuracy of the sectioning by preventing vibration of the microtome.

The microtome blade used in sectioning was made of stainless steel, and was regularly sharpened. When viewed under reflected light in an optical microscope, the smooth polished edge of a sharp blade was revealed as a narrow, straight, and unbroken bright line.

Operation of the microtome was straightforward and is illustrated schematically in Figure 4.10. The rotation of spindle A caused the

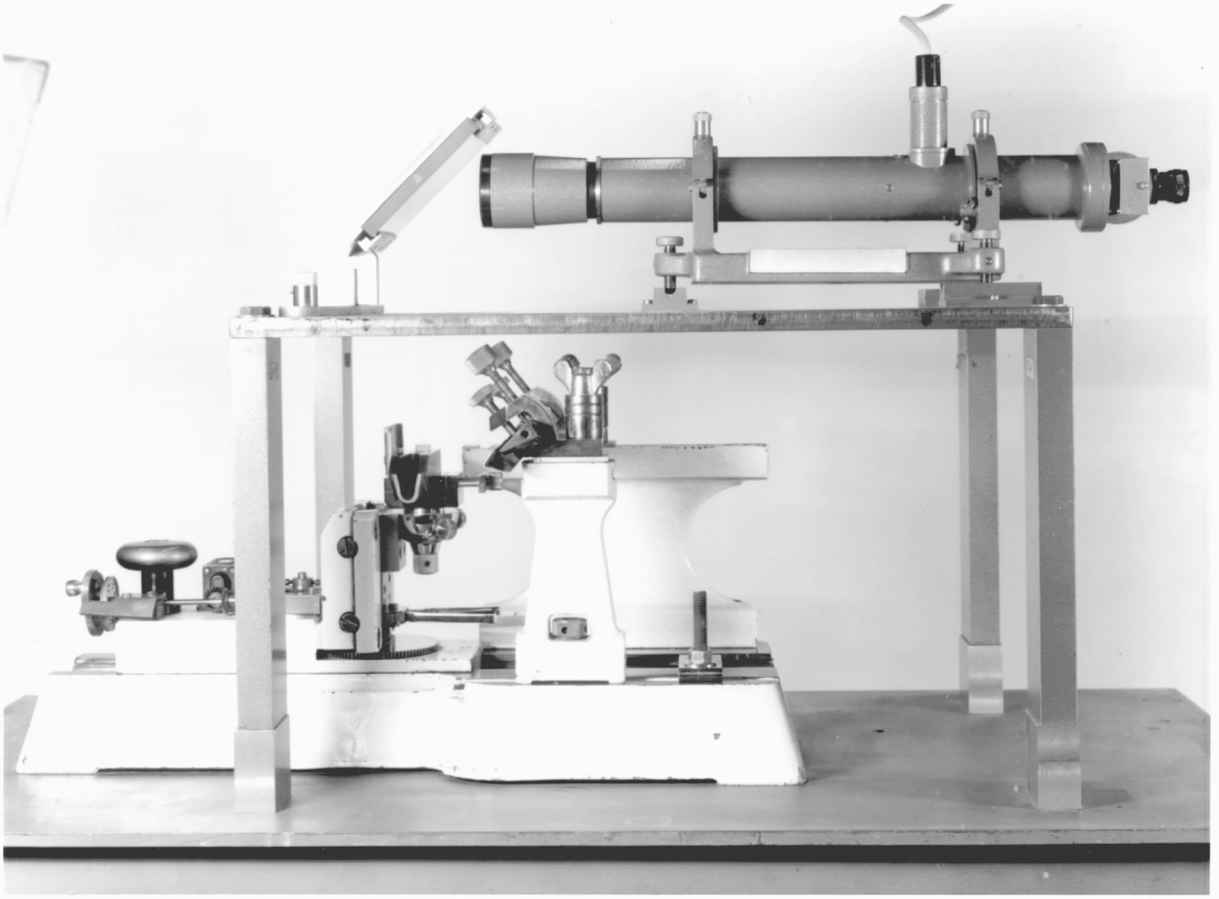


Fig. 4.8. The relative position of the microtome and the auto-collimator.



Fig. 4.9. Close up view of the sectioning unit of the microtome.

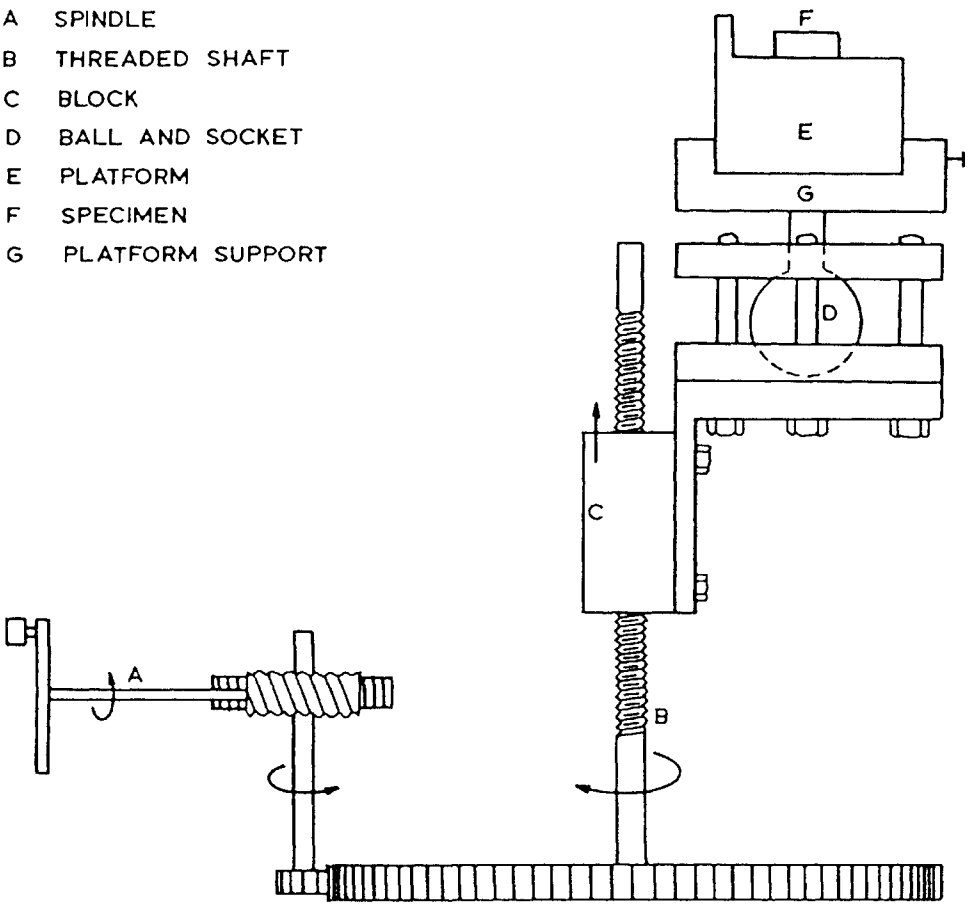


Fig.4.10. Schematic diagram of microtome.

threaded shaft B to rotate. The block C which was on the shaft B, was restrained from turning by the microtome body. When the shaft B rotated, the block and therefore the platform was either raised or lowered. The platform support which clamped the platform was mounted on the ball point D, and could be adjusted to give the desired angle between the sample and the blade. Every 5 complete rotations of the spindle was expected to change the level of the platform by 10 μm. However, regular calibration of the microtome was carried out. A dial-gauge having a sensitivity limit of 0.2 μm was attached to the platform of the microtome. The platform was raised by 5 complete revolutions of the spindle, and the corresponding reading on the dial gauge was recorded. This was repeated until the platform had theoretically been raised by 400 μm. The results of theoretical reading versus the dial gauge reading were plotted and is shown in Figure 4.11. For every 5 rotations of the spindle the deviations of the theoretical 10 μm values from those noted by the dial-gauge was observed to vary, with a standard deviation of ±0.95 μm, and a highest deviation of 2.2 μm. These might have resulted from the wearing out of some parts of the threads in the shaft. The general deviation trend tended to follow a sinusoidal curve. The positive errors were compensated for by the negative errors, so that, for an expected increment of 400 μm, there was an overall error of ±0.8%, i.e. ±3.2 μm.

As it was necessary to section parallel to the diffusion front, the surface of the crystal had to be aligned parallel to the knife edge. The following procedure was adopted to ensure this alignment was achieved. A dummy sample was mounted on some melted paraffin wax on the platform. A flat surface of the sample was microtomed at an angle of about 5° to the (001) plane. The angle ensured that the blade actually cut the surface of the sample, since the sample might splinter if the blade cut parallel to the (001) plane. An optically flat, with parallel sides,

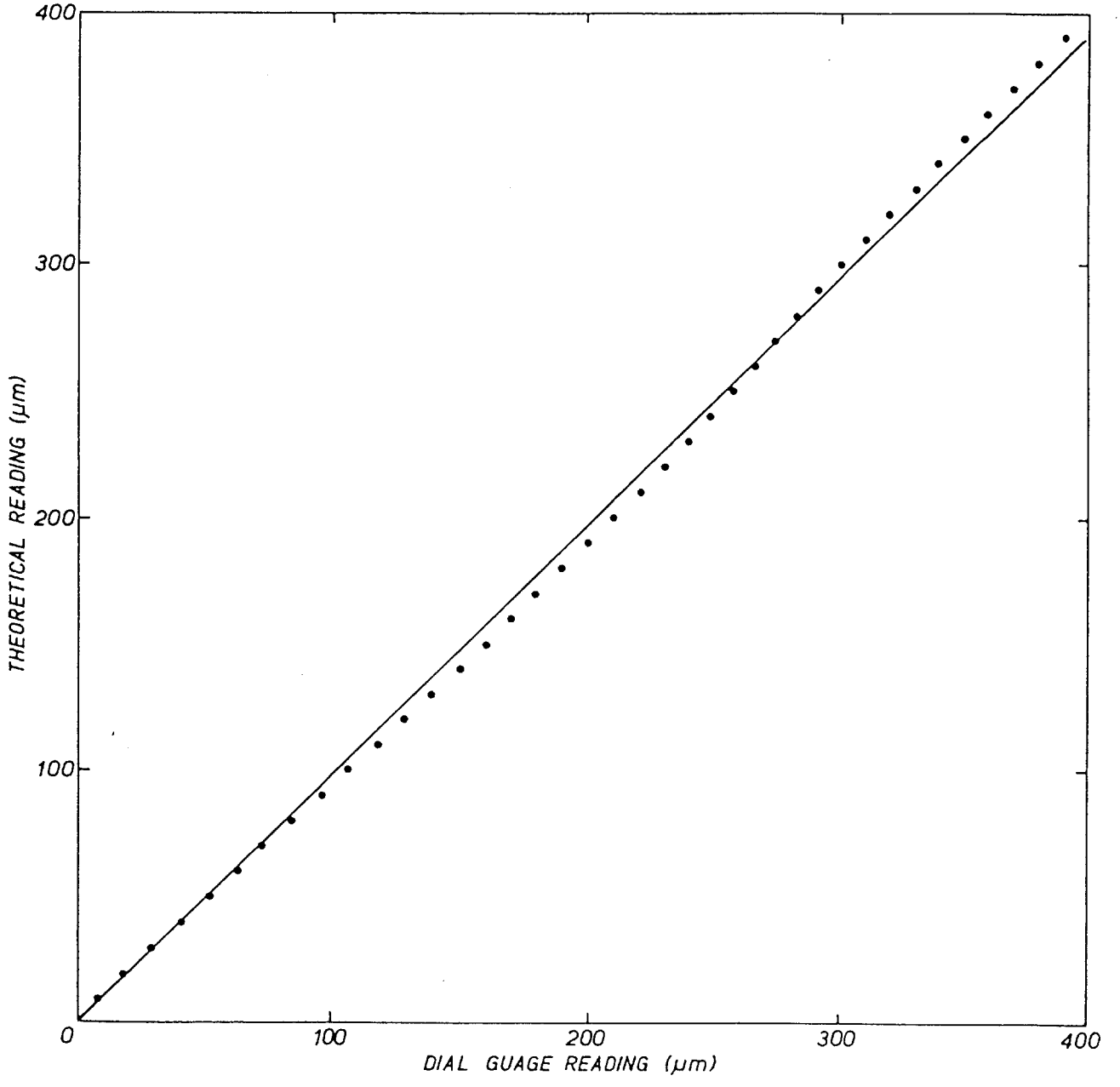


Fig.4.11. Microtome calibration plot.

silvered mirror mounted on a ball bearing tripod, was placed on the microtomed surface of the sample. A microptic auto-collimator (126) was fixed in a position as shown in Figure 4.8. The co-ordinates of the cross-wires in the autocollimator were adjusted to mark the reflected image from the mirror. This optical system could detect the planarity of the sample to an accuracy of 1 second of arc. The platform was then thoroughly rinsed in Analar benzene, after the sample was dismounted, to remove any traces of the wax.

About 1 mm was cleaved off the sides of the diffusion specimen to avoid any edge effect. The dimensions of the specimen surface were measured in several places with a travelling microscope. Each dimension was found to be constant to within ±0.02 mm. These were later measured again after the last slice of the specimen was sectioned. The biggest change of the dimensions ever noted was less than 0.05 mm.

The diffusion specimen was now mounted on to the platform with Durofix glue. The planarity of the specimen was then adjusted as described earlier until the reflected image of the cross-wires in the autocollimator fell back to the previously marked position. The effect of microtoming on the alignment of the specimen was checked after every 80 μm were sectioned. The biggest misalignment ever noted was 24 seconds of arc. It indicated that the surface of the specimen was parallel to the blade edge to within 1 μm over the crystal surface of 1 cm^2.

A series of 40 sections, 10 μm in thickness each, were microtomed from the specimen. The slices were noted to curl up slightly and hung together long enough for it to be brushed into the preweighed scintillation vials. The camel hair brushes were previously trimmed to the length of around 2 mm before use. A new brush was used for each slice of the specimen to avoid any cross-contamination between the slices. After collecting the slices, each brush used was ground gently against the inside wall of the vial to prevent any trapping of some of the specimen between the hair. After each sectioning, the microtome blade was rinsed

with acetone to remove any traces of powder of the specimen. When all the sectionings were completed, the vials were then dried overnight in a closed dry box at 90°C before they were subsequently reweighed.

4.6. Determination of Section Thickness by Weighing

The thickness of each microtomed section of specimen was determined by dividing the weight of the section by its area and density. The density of sodium chloride being 2.165 g per cm^3.

Weighing was carried out using a Stanton semi-microbalance, the sensitivity limit of which was 0.01 mg. The typical weight of a 10 μm slice of a 1 cm^2 specimen section was 2.165 mg.

Polyethylene scintillation vials were used to collect the sections of the sample. The average weight of the vial was around 6.5 g. Due to the nature of the vial material, static charges were found to exist on the walls of the vials which prevented accurate weighing, especially of small samples. The problem was circumvented by placing a Polonium-210 static eliminator disc (Radiochemical Centre of Amersham) behind the sample weighing pan of the balance. With careful acclimatisation of sample and vial, the absolute weighing error was found to be < 0.05 mg. For a 10 μm slice of 1 cm^2 sample section, the weighing error was ±2.3%.

The samples in the vials were stored in a dry box, and were left next to the balance case to acclimatise for at least 5 hours. This was particularly important if there were differences in humidity and temperature of the laboratory and the microbalance room. The vials were then placed inside the balance case and left for at least 10 minutes to equilibrate with the surroundings before weighing. Temperature and humidity inside the balance case were regularly checked. They were found to remain quite constant during the whole period of weighing.

Attempts were made to microtome thinner specimen sections. But in addition to producing an irregular thickness, the weighing error would increase to ±4.6% for a 1 cm^2 section of thickness 5 μm. A decrease in

sectional area of the specimen similarly increased weighing error, i.e. a $(0.8\ cm)^2$ section of 10 μm thickness had a weighing error of ±3.6%. Thus, the weighing error was a significant factor in determining the specimen-size obtained from microtoming. This is reflected in Table I.

Table I. Theoretical Weighing Errors in Percentage in Relation to the Area and Thickness of the Specimen Section.

Area in cm^2 / Thickness in μm	1.0^2	0.9^2	0.8^2	0.7^2
10.0	2.3	2.9	3.6	4.7
9.0	2.6	3.2	4.0	5.2
8.0	2.9	3.6	4.5	5.9
7.0	3.3	4.1	5.2	6.7
6.0	3.9	4.8	6.0	7.9
5.0	4.6	5.7	7.2	9.4

CHAPTER FIVE

RESULTS AND DISCUSSION

5.1. Precision and Limits of the Sectioning Technique

The main difficulties in applying the sectioning technique were experimental. The error in annealing times was negligible if the specimen was fairly rapidly introduced into the furnace at a preset annealing temperature and subsequently cooled rapidly after the anneal. By maintaining the diffusion anneal system in vacuum, temperature stability remained within ±1°C over the whole period of annealing. Similarly, the counting errors were small and did not exceed 1% since a sufficiently large number of counts were made in a long counting time.

A more important error was introduced in the determination of the thickness of the microtomed sections. If the dial gauge reading of the microtome was accepted, calibration of the microtome showed that there was an unacceptable ±10% error in raising the specimen by 10 μm. An alternative method of determining section thickness was by weighing the microtomed sections, making sure that all fragments and particles were collected directly in the scintillation vials. The usual method of weighing the specimen bulk before and after the sectioning experiment to double-check on the total amount of material removed during microtoming was not feasible in the present work. The specimen was glued onto the platform using Durofix, the solvent for which is also a solvent for the sodium chloride crystal specimen. Mounting the specimen with wax proved impractical since microtomed fragments adhered to the wax and could not be removed to the scintillation vial. Another conventional check on the amount of material loss during microtoming is to determine the total radioactivity of the specimen bulk before and after sectioning. This is possible only if a dry scintillation counting method such as Geiger counting is used. However, the counting efficiency by such a method is very low which is a disadvantage when counting specimens of low activity at the limit of diffusion penetration. The present work employed a high counting efficiency liquid scintillation method which prevented sample recovery.

In microtome sectioning, if ε is the thickness of the slice, ω is its weight, and d is the diameter of the specimen, then

$$\frac{\Delta\varepsilon}{\varepsilon} = \frac{\Delta\omega}{\omega} + 2\,\frac{\Delta d}{d} \qquad 5.1.$$

The relative error in d is very small. For a precision of 2% in the thickness cut, it is necessary that $\Delta\omega/\omega = 2\%$. To achieve this, with the absolute weighing error of the balance of ±0.05 mg, ω should be about 2.5 mg. For a 1 cm^2 sectioning area of a slice of NaCl, this should correspond to a thickness of the slice of around 10 μm, the thickness used in the present work.

The method of cutting can also introduce an error, if the requirement that the slices removed should be cut parallel to the diffusion plane is considered. Shirn, Wadja and Huntington (113) have tried to calculate this error. Suppose that from a square specimen of dimension a, slices are cut with a thickness ε, and that α is the angle of inclination of the axis of the sample to the axis of the microtome blade, it may be shown that the slope of the linear region in the ln C versus penetration^2 plot is equal to

$$-\frac{1}{4Dt}\left[1 - \frac{\varepsilon^2 + (a\alpha)^2}{24Dt}\right] \qquad 5.2.$$

The relative error of the slope of the line is thus equal to $\frac{\varepsilon^2 + (a\alpha)^2}{24Dt}$ If we take $D = 10^{-12}$ cm^2/sec, $t = 10^6$ seconds, $\varepsilon = 10^{-3}$ cm, a = 1 cm and $\alpha = 1/60°$, then the relative error of the slope is 3.7%. But if $\alpha = 1/6°$ the error will be 33%. Hence the importance of controlling the planarity of the specimen. In the present work, the largest angle of displacement ever noted during microtoming was 24 seconds of arc. This corresponds to an error of 3.4% in the slope of the ln C versus penetration^2 plot. Obviously, this error may be diminished by reducing the transverse dimension of the specimen. For example, if the microtomed section was 5 μm rather than 10 μm thick, the corresponding error would be 0.9%, although the weighing error would then be increased.

5.2. Cleavage Damage and Dislocations - Etch Pits

Figure 5.1. reveals the surface of a pre-etched specimen after annealing at 650°C for 24 hours. The surface of the same specimen, freshly cleaved, is shown in Figure 5.2. It is clear that a clean, freshly-cleaved surface is a pre-requisite for optical studies of dislocations. However, cleaving itself introduces deformation which, according to the geometry of the crystal, can result in dislocation densities increasing by an order of magnitude.

Figure 5.3(a)-(c) illustrate the cleaving damage after a specimen, 1 x 1 x 0.5 cm in size, was successively cleaved into halves along the same plane, and etched. Observation of the etched surfaces reveal a significant increase in the dislocation densities due to cleaving. It is impossible to monitor the original dislocation patterns with change in specimen depth by successive cleaving. Dislocations of this nature can be effectively reduced in number by prolonged annealing at very high temperature. However, annealing produces a surface effect which makes it difficult to image dislocations clearly, as shown in Figure 5.1.

Cleaving damage could be significantly minimised by choosing appropriate specimen dimensions, i.e. the ratio of specimen width to cross-sectional area should be large, and cleaving rapidly and efficiently. For example, when an annealed specimen of 1.5 x 1.5 x 1.5 cm^3 in size was etched and examined, the cleavage damage was restricted mainly to a region immediately surrounding the contact point between cleaving blade and the specimen. The observed dislocation density of the remainder of the specimen surface was of the order $10^4 cm^{-1}$. The latter is demonstrated in Figure 5.10(a)-(c).

Dislocations emerging at a specimen surface can be readily observed by chemically treating the surface to develop an etch-pit pattern. A number of methods have been used to confirm the one-to-one correspondence between dislocations and etch-pits. Vogel et al (125) compared the

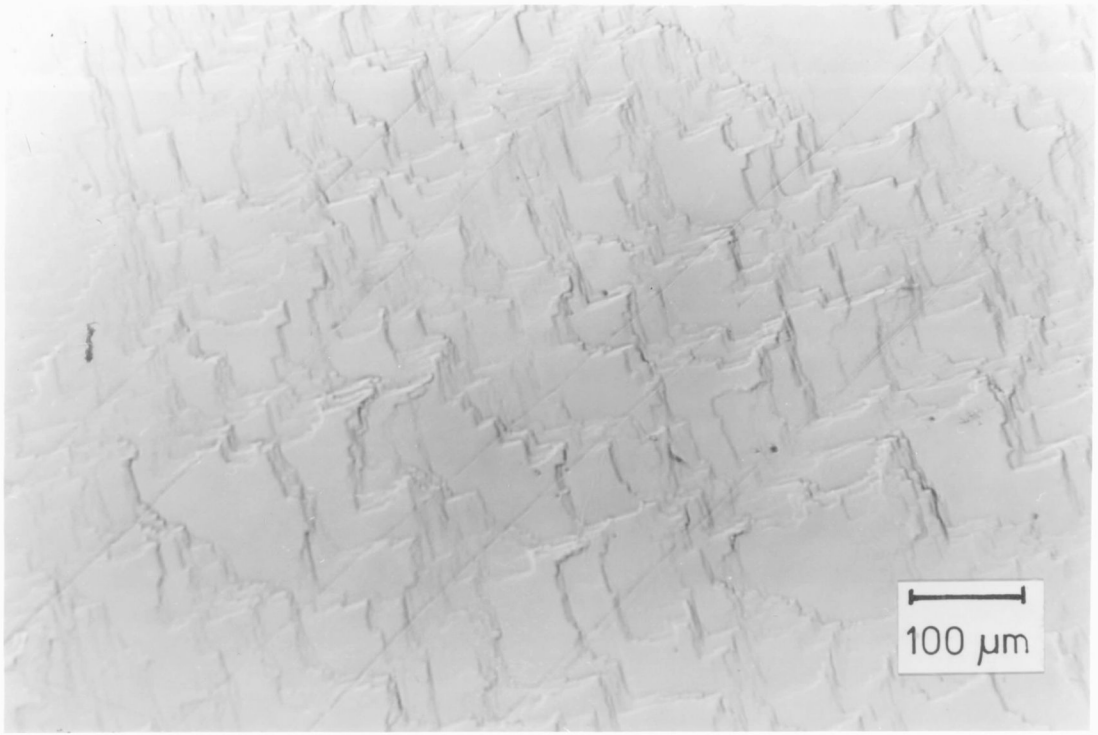


Fig. 5.1. Surface of a well-annealed NaCl specimen.

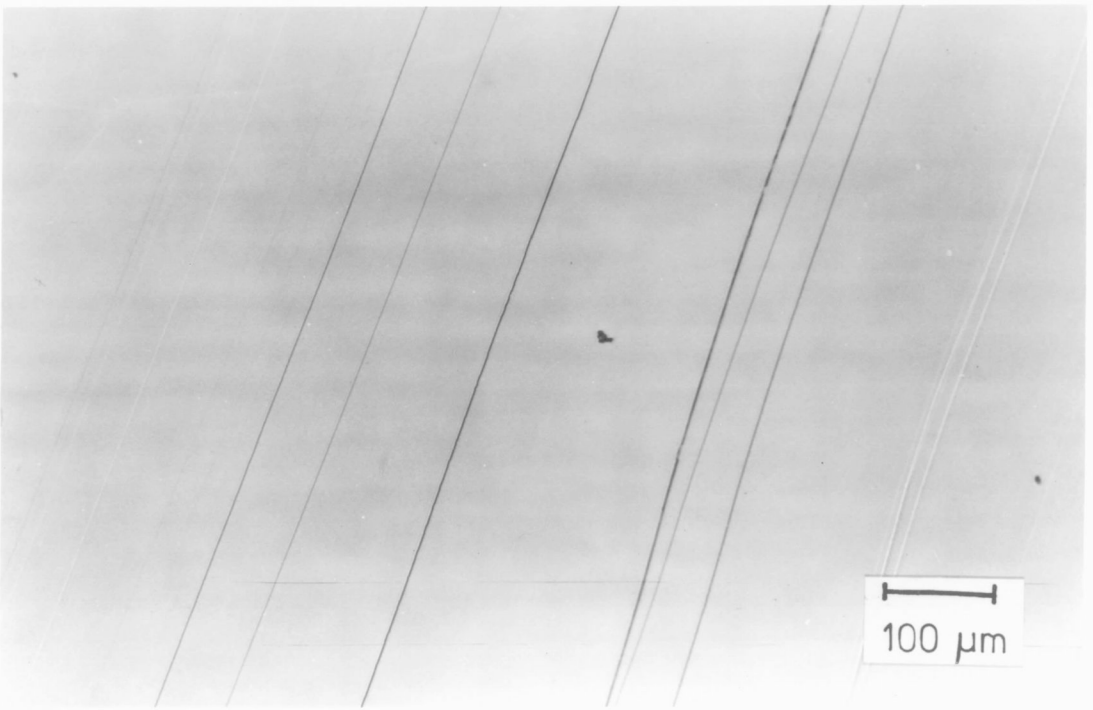


Fig. 5.2. Surface of a freshly cleaved NaCl specimen.

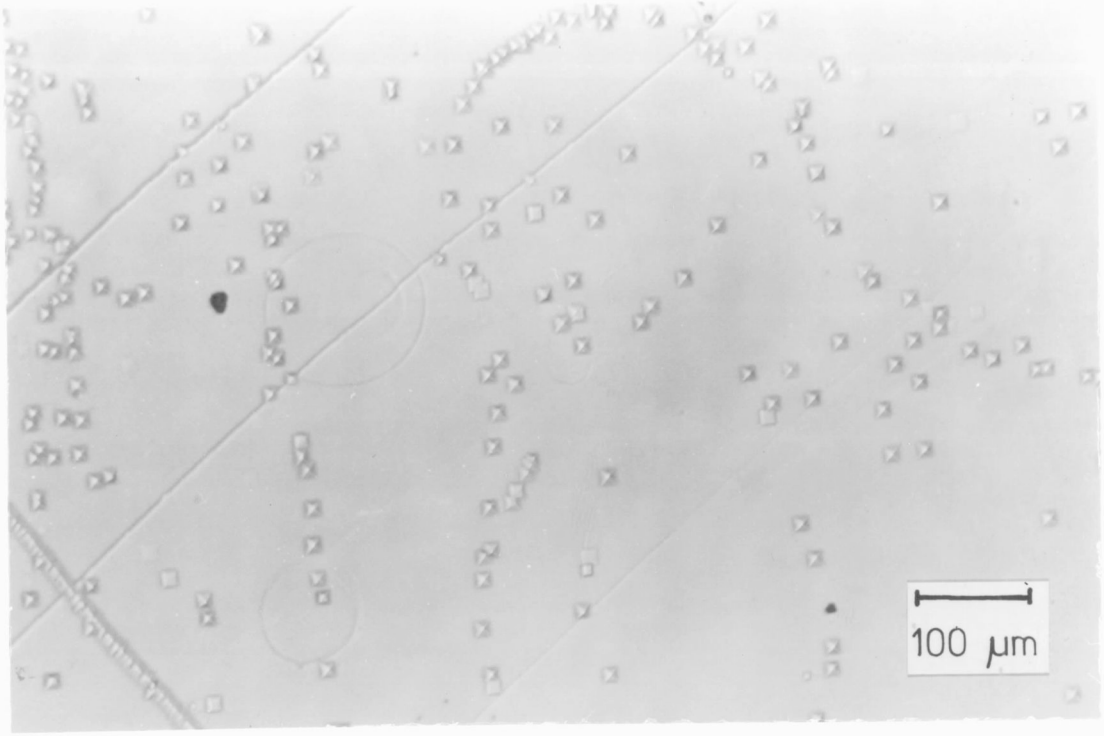


Fig. 5.3. (a)

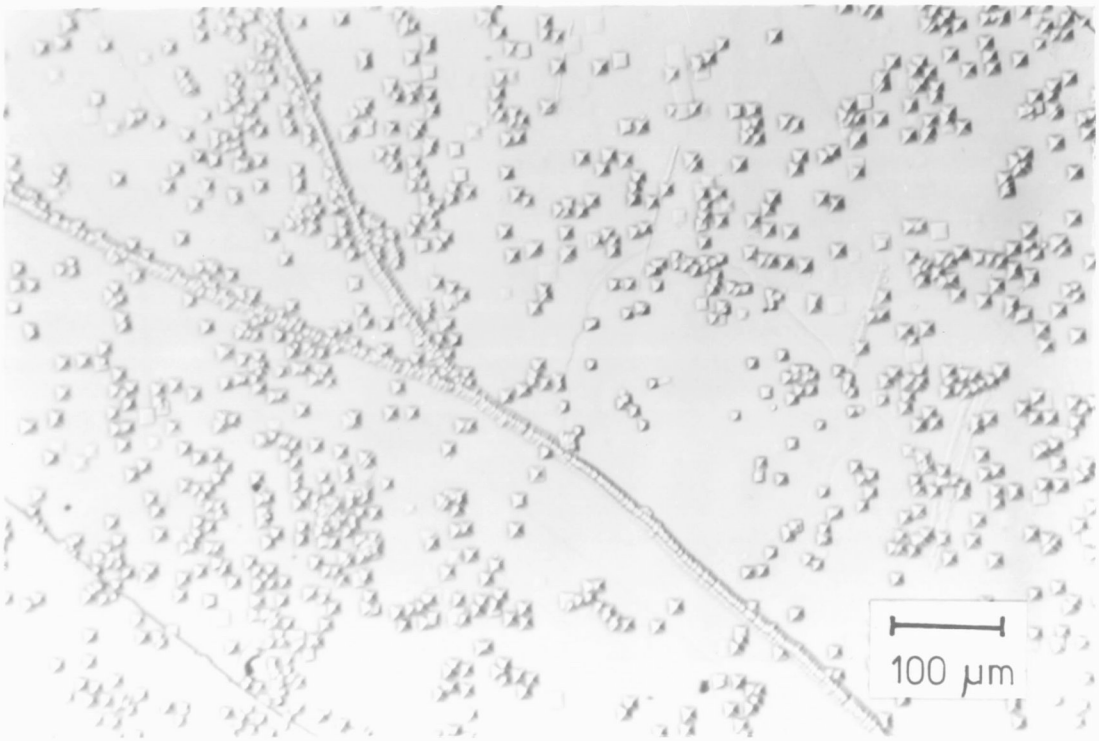


Fig. 5.3. (b)

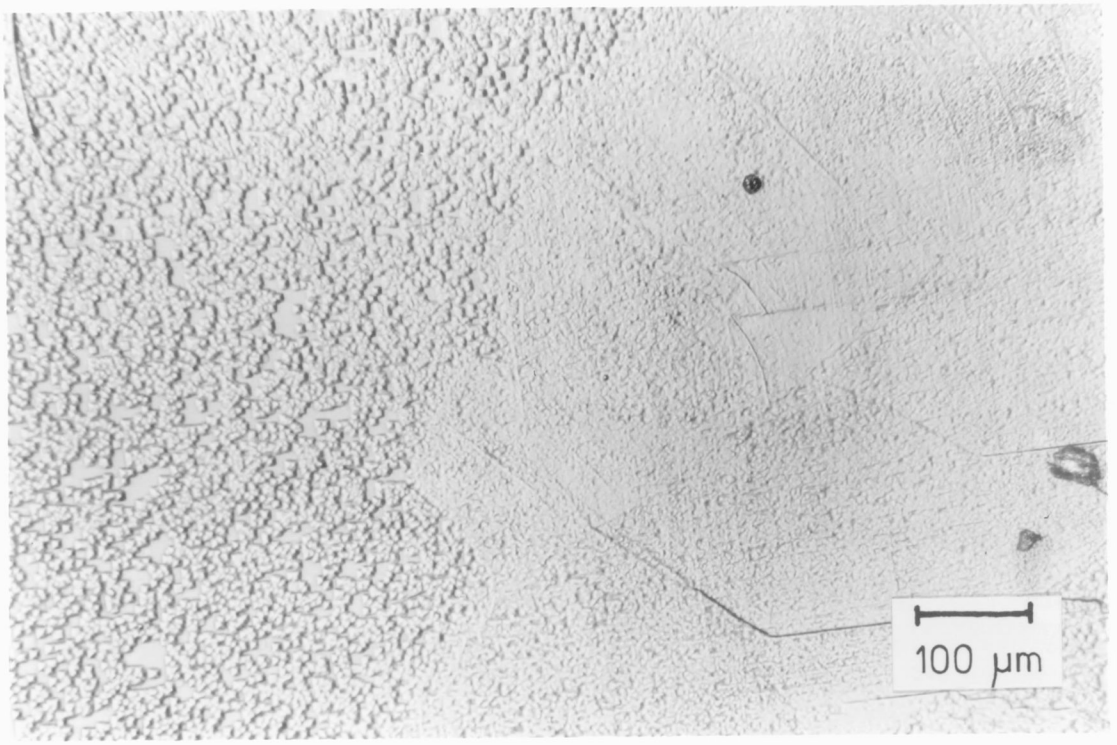


Fig. 5.3. (c)

Fig. 5.3. (a)-(c). Etched-surface of a NaCl specimen showing the damage of successive cleaving.

measured spacing d of etch pits in a pure tilt boundary in germanium with the orientation change, θ, across the boundary. The angle θ was measured by an X-ray method, and for very small angles, $\theta \simeq b/d$. They confirmed that each etch-pit in the boundary correspond to a dislocation.

Amelinckx (4) pointed out that when three, asymmetric pure tilt boundaries meet along a nodal line, the linear densities ρ_i, of dislocations along the three boundaries must satisfy the condition that

$$\sum_{i=1}^{3} \frac{\rho_i}{\cos \phi_i + \sin \phi_i} = 0$$

where ϕ_i is the angle between the ith boundary and a symmetrical boundary. Amelinckx found that this relationship was satisfied for the grain boundary junctions in NaCl, which implied the one-to-one correspondence between etch pits and dislocations.

In the present work, it is reasonable to assume that all dislocations are etched, and that each corresponds to an etch pit observed on the specimen surface.

5.3. Bending and Polygonisation

In all dislocation diffusion experiments, the value of the bulk diffusion coefficient D has to be known in order to determine the diffusion coefficient along dislocations D_d. Transport properties in NaCl, particularly at low temperatures, are structure sensitive. Thus, the appropriate value of D cannot be extracted from the literature but has to be measured. From the tracer diffusion profile of the specimen, the value of D can be determined from the initial steep slope of the curve, and subsequently a^2D_d from the 'tail' of the profile that represents the deep penetration region. Due to the technical difficulties of microtoming less than 10 μm sections, the value D, in the present work, can only be reliably determined from a profile with a minimum bulk diffusion penetration of about 40 μm. Hence, the decision was made to set the bulk diffusion length $(Dt)^{1/2}$ at about 10 μm for the study of self

diffusion via isolated dislocation-pipes. To ensure that these diffusion paths are isolated and independent of each other, the inter-dislocation distance d should not be less than $2(Dt)^{1/2}$, i.e. 20 μm. The aim of bending and polygonising the specimens is to provide such stable isolated diffusion paths.

The slip systems in a crystal for dislocation movement that will predominantly be employed during deformation will depend on the direction in which the shearing stress is applied. The Burgers vector for slip in many crystals lies in the plane of closest atomic packing, which in NaCl are the {100} planes. But observations have shown that the slip planes in NaCl crystals are the {110} series. The reasons for the adoption of the less dense {110} planes in NaCl are rather involved. The main reason is associated with the repulsive forces between ions of like charge which are brought into closer proximity as the dislocation moves. In NaCl this effect is less pronounced for dislocations moving on the {110} planes than for those moving on {100} planes.

NaCl crystals were bent to various strains in the present work and were shown to be plastically deformed by observing the stress birefringence pattern when a specimen was viewed under polarised light after the applied stress had been relieved. This further demonstrates that the slip systems are of the {110} type. Deformation by four-point bending is essentially a non-uniform process. The dislocation density is a maximum at the tensile region near the $[00\bar{1}]$ plane. It decreases to a minimum as it reaches the neutral axis of the specimen and rises to a maximum as it approaches the compressive [001] plane. The average dislocation density in a typical specimen under 0.2% strain is of the order 10^6 cm^{-2}, and fresh dislocations of this nature are quite mobile particularly at elevated temperature.

During ideal 4-point bending of a NaCl crystal, there are 4 glide systems for dislocation motion, namely the [011], [0$\bar{1}$1], [$\bar{1}$10] and [110] planes. The resolved shear stress acting on the [$\bar{1}$01] and [101] planes is zero, and thus these two planes are not responsible for any dislocation slip. Due to the relative mobility of edge and screw dislocations in NaCl, the existence of a 3-dimensional slip is quite unlikely, and 2-D slip on the [0$\bar{1}$1] and [011] planes is predominant. Subsequently, etching of [100] specimen planes reveals the dislocation arrangement along [0$\bar{1}$1] and [011] slip planes.

During polygonisation, edge dislocations start gliding along the [0$\bar{1}$1] and [011] planes and anihilating dislocations of the opposite sign on the corresponding planes. At elevated temperatures, dislocations act as 'sources' or 'sinks' for vacancies and the half planes may thus climb up or down. The result of polygonisation is a general reduction of the dislocation density in the specimen, and the excess dislocations of a given sign group together in a low energy state as arrays of low angle boundaries. The higher the strain that the specimen experiences, the higher is the dislocation density, and the closer is the spacing of separate dislocations in the dislocation walls.

Figure 5.4. shows the dislocation arrangement on the etched surface of a specimen loaded to 0.3% strain, polygonised at 650°C for 1 hour, and then further annealed at 400°C for 1 week. Specimens were always polygonised at temperatures much higher than the chosen diffusion temperatures to ensure that the dislocations were stabilised and thus the tracer diffusion paths were preserved before and after diffusion annealing. The numerous scattered dislocations observed between the arrays of dislocation walls in the micrograph, indicate that the polygonisation is incomplete. The steps shown in the micrograph provide evidence that some dislocations were in the process of climbing out of their original slip planes.

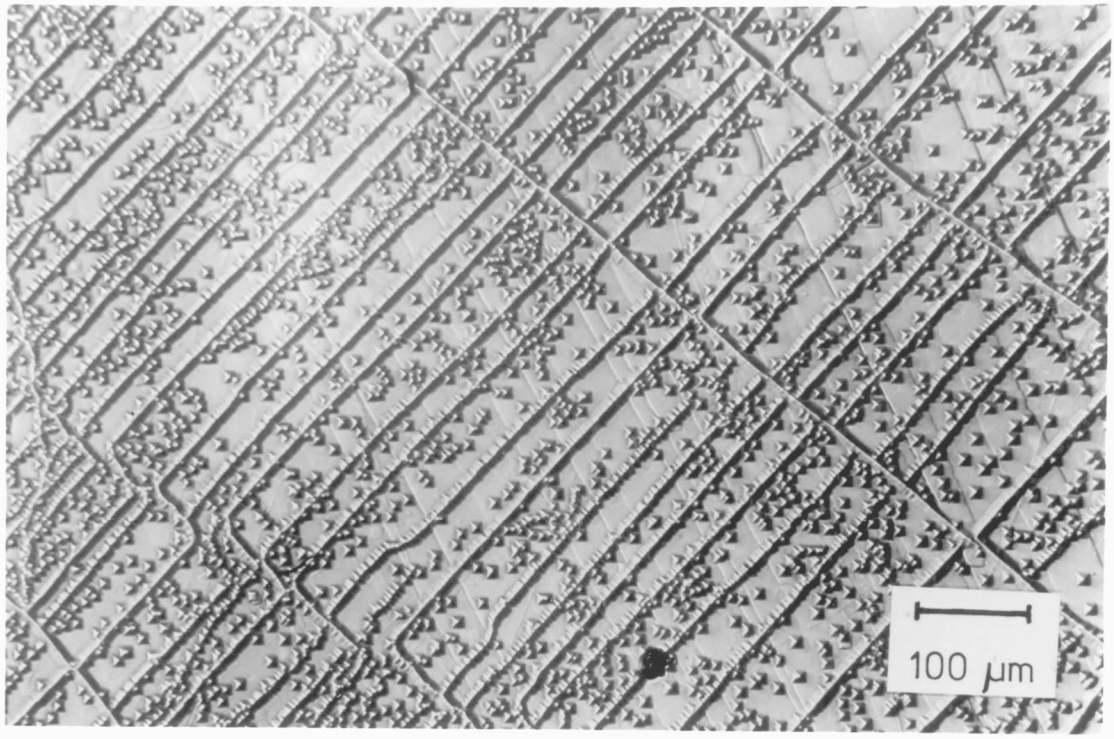


Fig. 5.4. Etched [100] surface of NaCl specimen loaded to 0.3% strain and polygonised at 650°C for 1 hr.

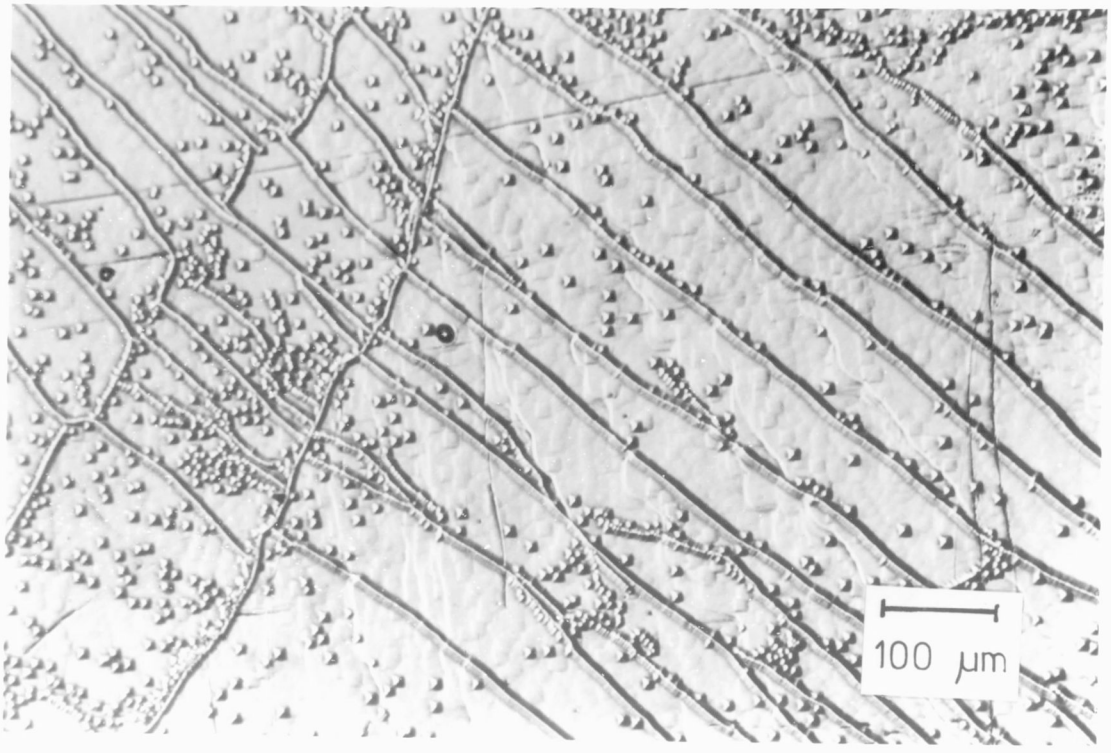


Fig. 5.5. Same as Fig. 5.4. but ε = 0.2%, T = 600°C and t = 2 hrs.

Figure 5.5. shows the dislocation arrangement in a specimen loaded to 0.2% strain and polygonised at 600°C for 2 hours. The faint etch-pit marks in the background are the debris of the dislocations that had moved away during polygonisation. Scattered dislocations are found at the two corners of the micrograph, which may indicate deformation during non-uniform bending, with areas of low dislocation density not being polygonised into low angle boundaries. It should be noted that the interboundary distances are increased slightly, when compared with the specimen shown in Figure 5.4., with decrease in percentage strain.

The dislocation arrangement of a specimen also loaded to 0.2% strain, but polygonised at the higher temperature of 650°C for 2 hours, is shown in Figure 5.6. The overall dislocation density is significantly reduced. There is clear evidence of the neutral axis of the bending system which marks the least strained region of the specimen. Slip steps of the [101] or [$\bar{1}$01] origins are observed as vertical lines across the micrograph. The presence of such features indicates some fault in the bending of this particular specimen. This could be due to the fact that [001] faces of the specimen were not flat but slightly twisted, which would give rise to dislocation slip on the [101] and [$\bar{1}$01] planes. These further act as some kind of barrier for [011] dislocation movement, resulting in dislocation pile-up along the line. The faint horizontal lines on the micrograph suggest the sites of emergence of the screw dislocations from the [110] or [$\bar{1}$10] planes. The existence of this 3-D slip in the present system is not clearly understood.

Attempts were made to reduce the dislocation density, and hence the inter-dislocation spacing d, by reducing further the level of strain in the specimens, and polygonising at higher temperature. Figure 5.7. reveals the etched surface of a specimen loaded to 0.1% strain and polygonised at 650°C for 2 hours. The number of scattered 'background' dislocations is reduced, indicating more efficient polygonisation and

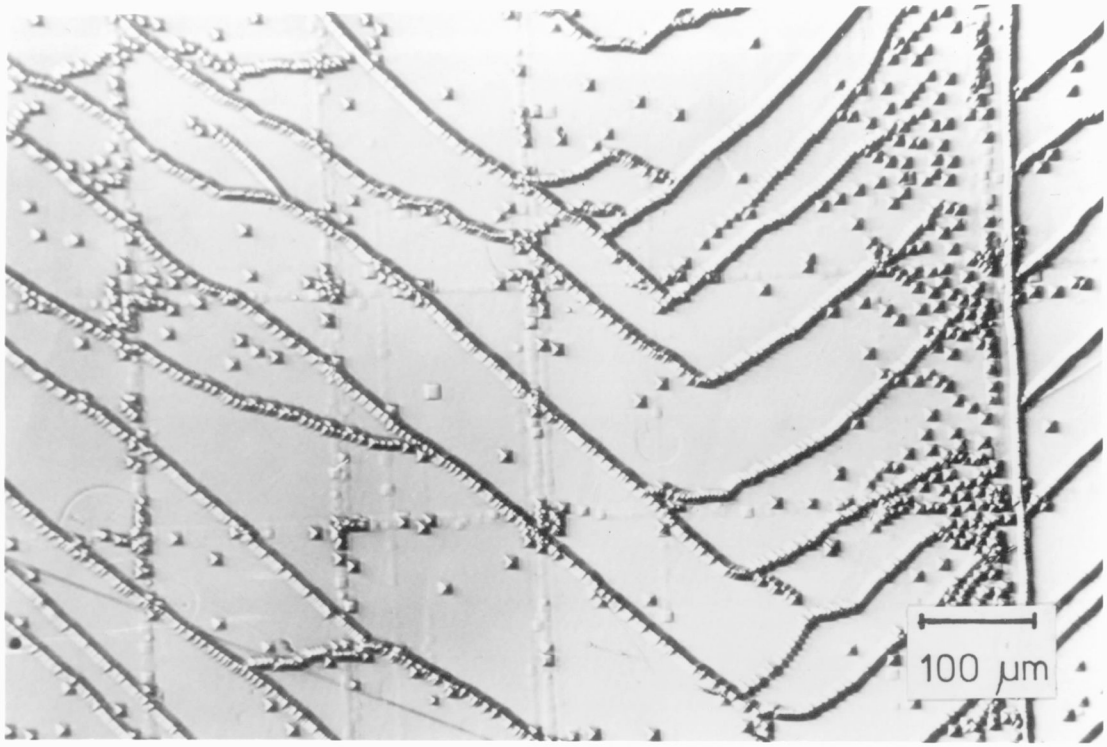


Fig. 5.6. Same as Fig. 5.4., but ε = 0.2%, T = 650°C, and t = 2 hrs.

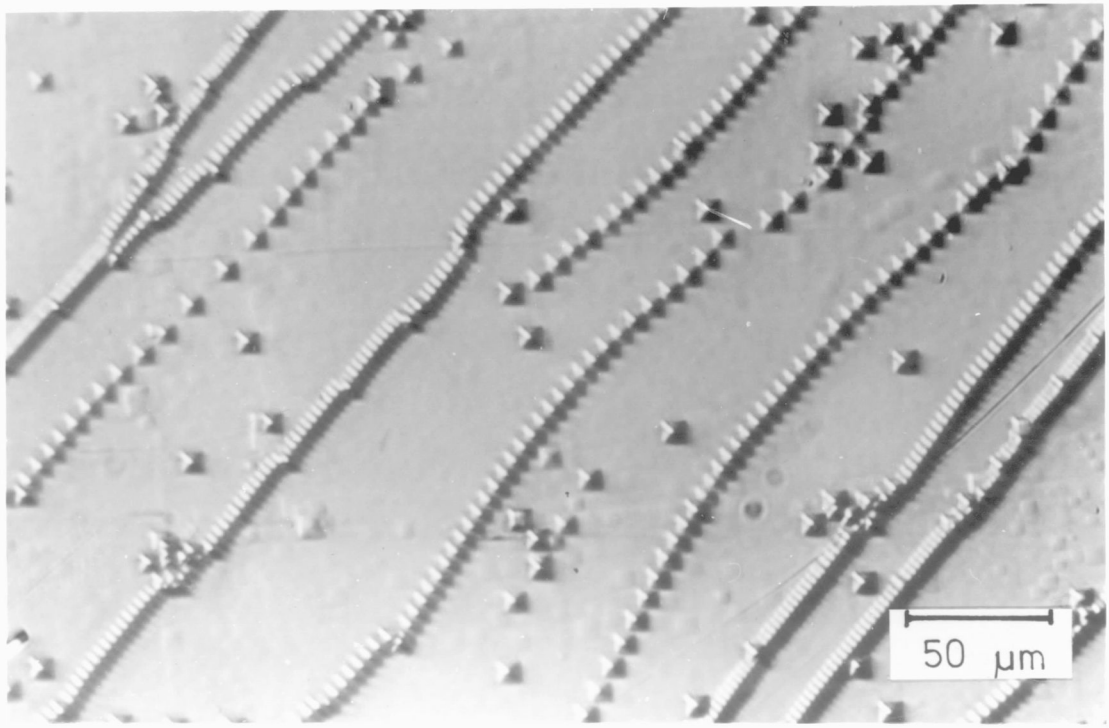


Fig. 5.7. Same as Fig. 5.4., but ε = 0.1%, T = 650°C, and t = 2 hrs.

alignment to form low angle boundaries. The average distance between the boundaries is ∿40 μm and, in most cases, the average inter-dislocation spacing d, along the boundaries, is ∿7 μm.

The specimen shown in Figure 5.8. was also loaded to 0.1% strain but was polygonised at the higher temperature of 700°C for 2 hours. The inter-boundary distances increased significantly to an average of about 75 μm, which may be the result of the coalescence of some boundaries. Evidence of such movement is observed at the top right hand corner of the micrograph, where two adjacent parallel rows of dislocations stop and another boundary of increased dislocation density emerges at a mid-point between the two. A reasonable number of non-polygonised dislocations are observed between the boundaries, indicating that coalescence of the boundaries was incomplete, leaving some dislocations of the intial boundaries between the coalesced walls. The widest inter-dislocation spacing, d, along the boundaries is ∿7 μm but decreases to 3 μm in the more closely spaced boundary.

Figure 5.9. shows the surface of an etched specimen, loaded to 0.05% strain and polygonised at 700°C for 2 hours. The micrograph shows a reduction in the overall dislocation density and an increase in the inter-boundary distance to ∿200 μm. However, the spacing d is still as high as 7 μm. Loading to strains < 0.05% was not attempted since the yield point is approached and deformation becomes predominantly elastic.

These results demonstrated that polygonisation of a strained NaCl specimen aligns dislocations into arrays of low angle boundaries lying in the {110} planes. Also, by varying the percentage strain in the specimen, and conditions of polygonisation, patterns of dislocation walls with different overall dislocation densities are produced. Once formed, the dislocation walls are quite stable, but at temperatures > 650°C, they start to coalesce. However, the observed spacing d between the dislocations of each boundary in all specimens remained well below 20 μm, and the



Fig. 5.8. Same as Fig. 5.4, but ε = 0.1%, T = 700°C, and t = 2 hrs.

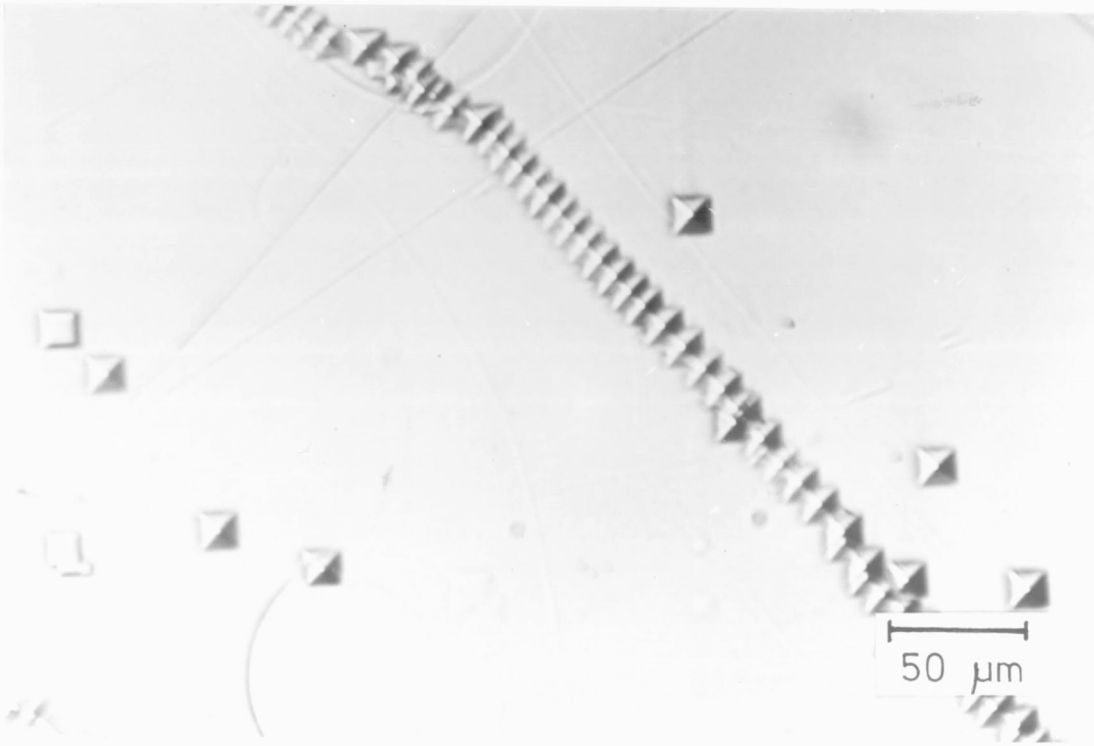


Fig. 5.9. Same as Fig. 5.4., but ε = 0.05%, T = 700°C, and t = 2 hrs.

condition, $2(Dt)^{1/2} < d \lesssim 20$ μm, for the stable dislocations to be isolated and independent of each other, was not achieved.

Attempts were then made to use a well annealed specimen that had not previously been subjected to any deliberate deformation. Figure 5.10 (a)-(c) show the etched surface of three slightly different areas of such a typical specimen, annealed at 700°C for 24 hours, and reveals a dislocation density of the order 10^4 cm^{-2}. Generally the dislocations are well separated with $d > 20$ μm. These in-grown dislocations attract impurities present in the crystal, and tend to act as barriers to dislocation motions. Thus, it was reasonable to assume that such dislocations remained quite stable, even after prolonged periods of diffusion annealing at relatively low temperature. Such specimens were used for tracer diffusion studies and found to produce well-defined "tails" in the diffusion profiles which were subsequently identified as a true representation of diffusion along isolated dislocation pipes (see discussion in the later section).

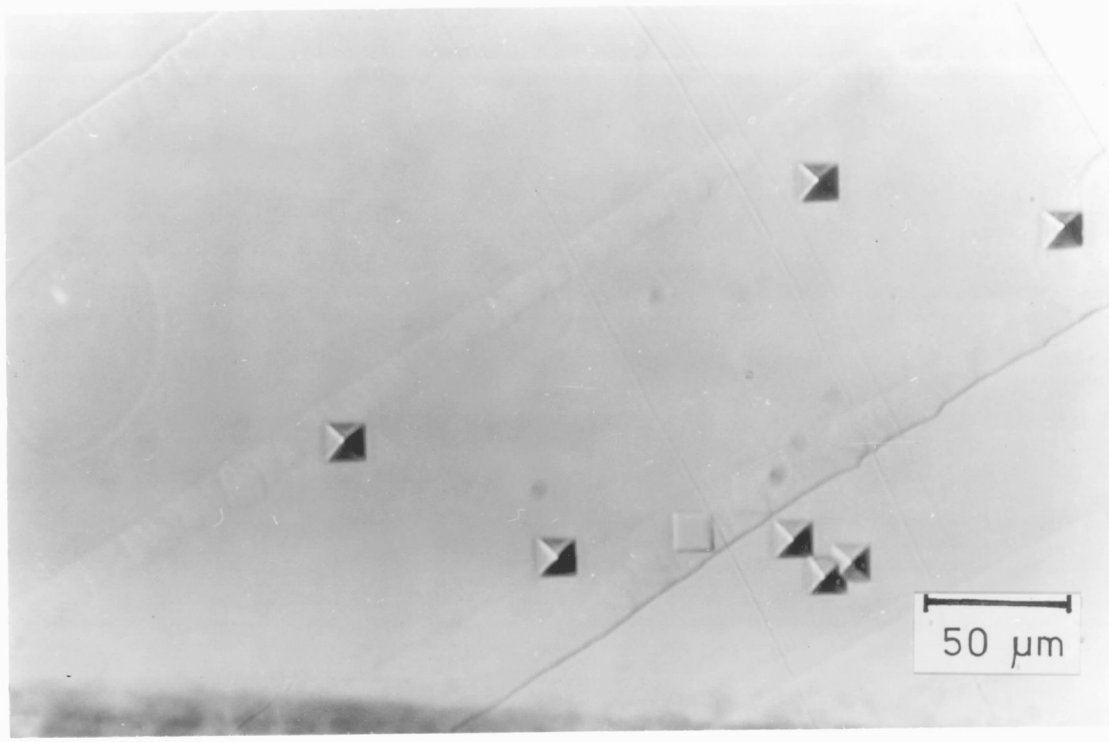


Fig. 5.10 (a)

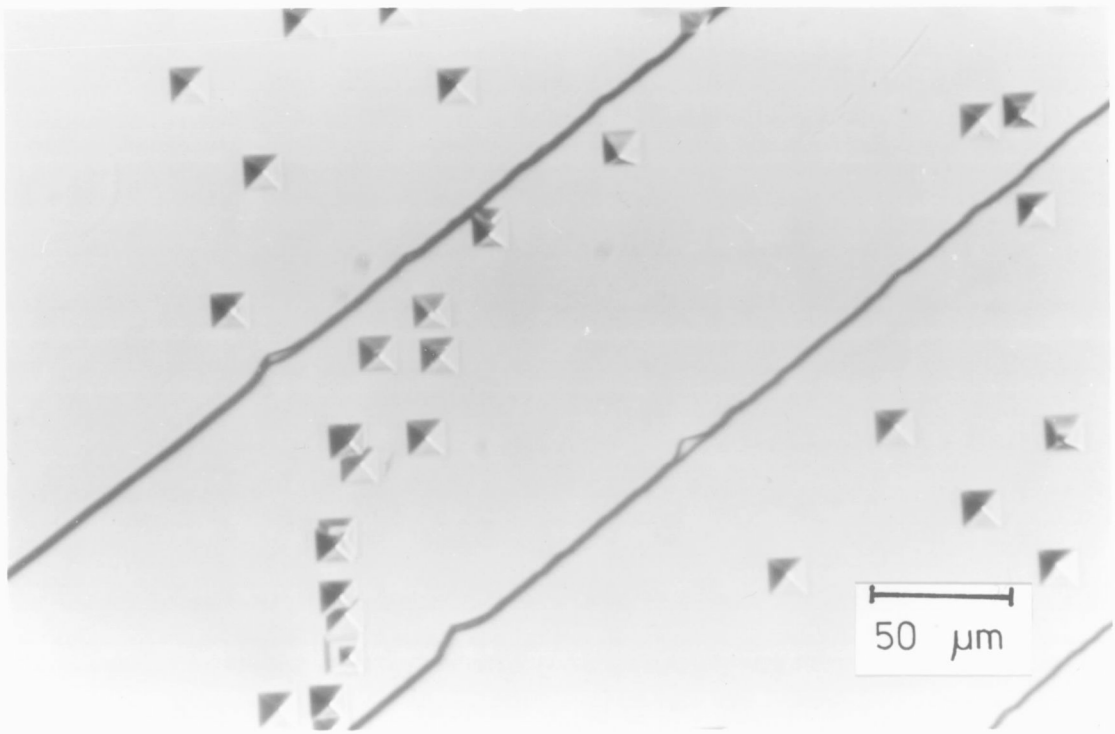


Fig. 5.10 (b)

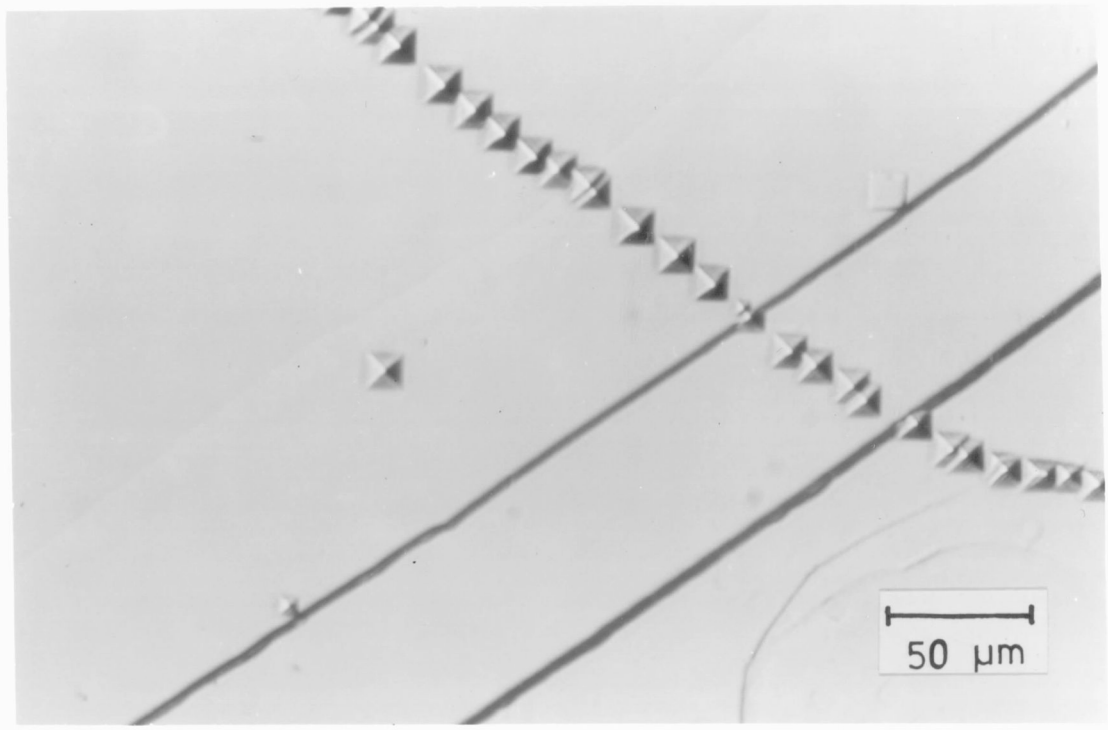


Fig. 5.10.(c)

Fig. 5.10. (a)-(c). Etched-surface of different areas of a non-deformed NaCl specimen.

5.4 Analysis of the chemical contents of specimens

5.4.1 Spectroscopic determination of the divalent cation and hydroxyl anion impurity contents

Replicas of specimens taken from the grown crystals used in the final 5 diffusion experiments were analysed to account for any variation in the diffusion behaviour. Samples 1 to 3 were prepared from the same crystal while samples 4 to 5 were prepared from another crystal grown in an identical way. The results of the analyses are presented in Table II.

Table II. Spectroscopic Analysis of Calcium and Magnesium Impurity Contents.

Sample Number	Diffusion temperature in ^{o}C	Ca^{++} in ppm	Mg^{++} in ppm
1	374	1.0 ± 0.1	0.4 ± 0.1
2	414	9.1 ± 1.0	0.5 ± 0.1
3	449	1.2 ± 0.1	0.5 ± 0.1
4	505	1.6 ± 0.2	0.4 ± 0.1
5	506	2.4 ± 0.2	0.4 ± 0.1

The analysis of calcium and magnesium contents was carried out using a Perkin-Elmer Model 290 atomic absorption spectrometer, the detection limit of such divalent cations using the technique being <0.1 ppm. The magnesium contents in all five samples were found to range from 0.4 to 0.5 ppm. A high calcium contents was found in sample 2, which was in poor agreement with the results from the samples 1 and 3, extracted from the same crystal boule. Therefore, the anomalous result for sample 2 is unlikely to be a true reflection of its Ca^{++} concentration. It has been suggested that the high value

may have resulted from contamination by $CaSO_4$, used as hardener in the white paper of the envelope in which this particular sample was stored. The calcium contents of the other samples range from 1 to 2.4 ppm. In general, the results obtained confirm the purity levels claimed by the manufacturer for the starting powder, i.e. $Ca^{++} < 5$ ppm and $Mg^{++} < 3$ ppm.

The hydroxyl ion impurity was determined using a Perkin-Elmer Model 621 double beam infra-red spectrometer, in the wavelength range of 3000 to 4000 cm^{-1}, and a sample thickness ranging from 0.7 to 1.5 cm. Entrained hydroxyl ions were expected to give a peak at 3450 cm^{-1}, but comparison with a standard revealed no peak at all at that wavelength. The absence of such a peak does not necessarily imply that hydroxyl ions were absent, but suggests that the concentrations were below the detection limit of the spectrometer, and might be in the region of 1 ppm.

5.4.2 Determination of the divalent cation impurity contents using the conductivity technique

The experiment was performed with the aim of establishing the Knee temperature and the formation energy of a Schottky pair of vacancies in a sodium chloride single crystal, and thus to determine the total cation impurity content.

This experiment was carried out with the help of Guerrero (49) who has previously described the experimental details. The specimen used was identical to that used in the diffusion Run 3. Etzel (35) has reported that the conductivity decreases with time particularly at high temperature. In this experiment, the specimen was cycled a number of times between 360 °C and 680 °C until a consistent conductivity

reading was obtained at the higher temperature, before the full data were collected. The conductivity of the specimen was measured in the temperature range 683 °C to 356 °C using A.C. at a frequency of 20 kHz. The lower temperature limit was determined by the sensitivity limit (∿ 350 °C) of the Wayne-Kerr Bridge employed. The conductivity data are tabulated in Appendix V, and the plot of $\log(\sigma T)$ versus 1000/T is shown in Fig.5.11.

The linearity of the intrinsic region I extends from the 3rd to the 10th point of the conductivity plot. The region between the 11th and 14th points of the plot appears to have a distinctly different slope and is called stage II'. The apparent extrinsic region II ranges from the 16th to the 23rd point of the plot. The region from the 24th to the last point of the plot represents stage II" which deviates slightly from the linearity of stage II due to the association of the cation vacancies with the divalent cation impurities.

From the extrapolations of stage I and II, the Knee temperature of the specimen was found to be 532 °C. From the gradients of stages I, II' and II of the conductivity plot, the corresponding activation energies were calculated as 1.84 ± 0.02 eV, 1.25 ± 0.01 eV, and 0.71 ± 0.01 eV respectively.

i.e. $Q_I = Hm + H_{f/2} = 1.84 \pm 0.02$ eV 5.3

$Q_{II} = Hm = 0.71 \pm 0.01$ eV 5.4

Thus H_f, or the formation energy of a Schottky pair of vacancies was calculated as 2.27 ± 0.06 eV.

In the intrinsic region, the concentration of the cation vacancies is thermally controlled and is represented by the equation

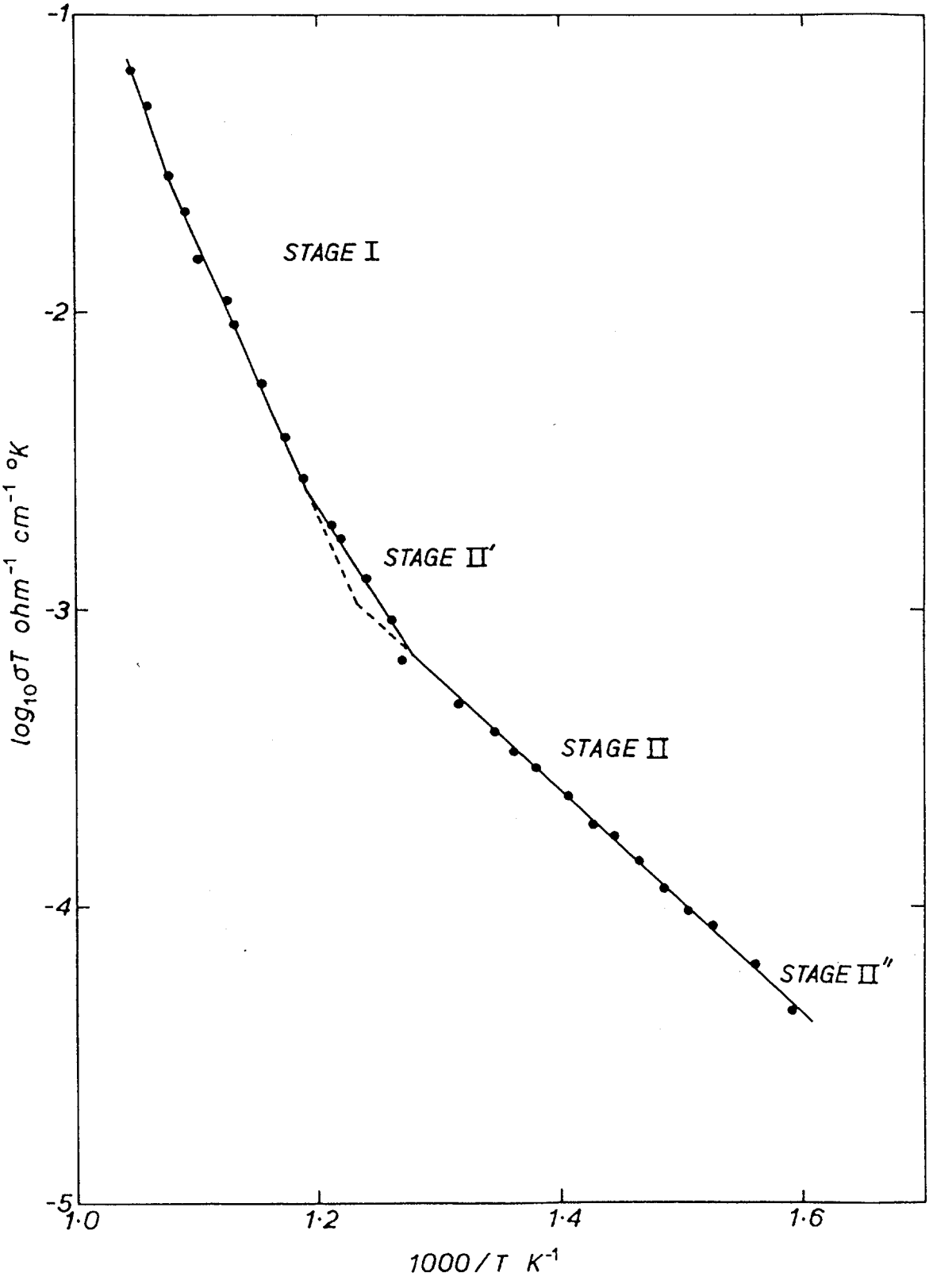


FIG.5.11 Arrhenius conductivity plot for a pure NaCl crystal

$$X_v = \exp - \left[\frac{H_f}{2kT} - \frac{S_f}{2k} \right]$$

In the extrinsic region, the concentration of the cation vacancies is determined by the total amount of divalent cation impurity existing in the crystal. This is equal to X_v at the Knee temperature where the intrinsic and extrinsic regions meet. From above, H_f was found to be 2.27 eV, the value $\frac{S_f}{2k} = 2.7$ being quoted from Guerrero (49) who determined the value from a conductivity-comparison plot. From the Knee temperature of 532 °C, X_v was calculated as $(1.2 \pm 0.5) \times 10^{-6}$. Since each of the cation vacancies in the extrinsic region is induced by a divalent cation impurity, the total effective concentration of divalent cation impurities in the specimen is (1.2 ± 0.5) ppm. However, spectroscopic analysis of an identical specimen showed that the concentrations of Ca^{++} and Mg^{++} were (1.2 ± 0.1) ppm and (0.5 ± 0.1) ppm respectively. This implies that some of the divalent cation impurity in the specimen was bound by existing anion impurity such as OH^-, so that the concentration of divalent cation impurity which induced the formation of cation vacancies was effectively 1.2 ppm

5.5 Diffusion and Conductivity

Figs 5.12 - 5.16 show the overall diffusion profiles of Na^{22} tracer in NaCl single crystals at different diffusion times and temperatures. The initial portions of the $\ln C/C_0$ versus penetration plots correspond to the region where lattice diffusion predominated. The 'tails' of the curves represent the deep penetration region where diffusion was greatly enhanced by the presence of dislocations.

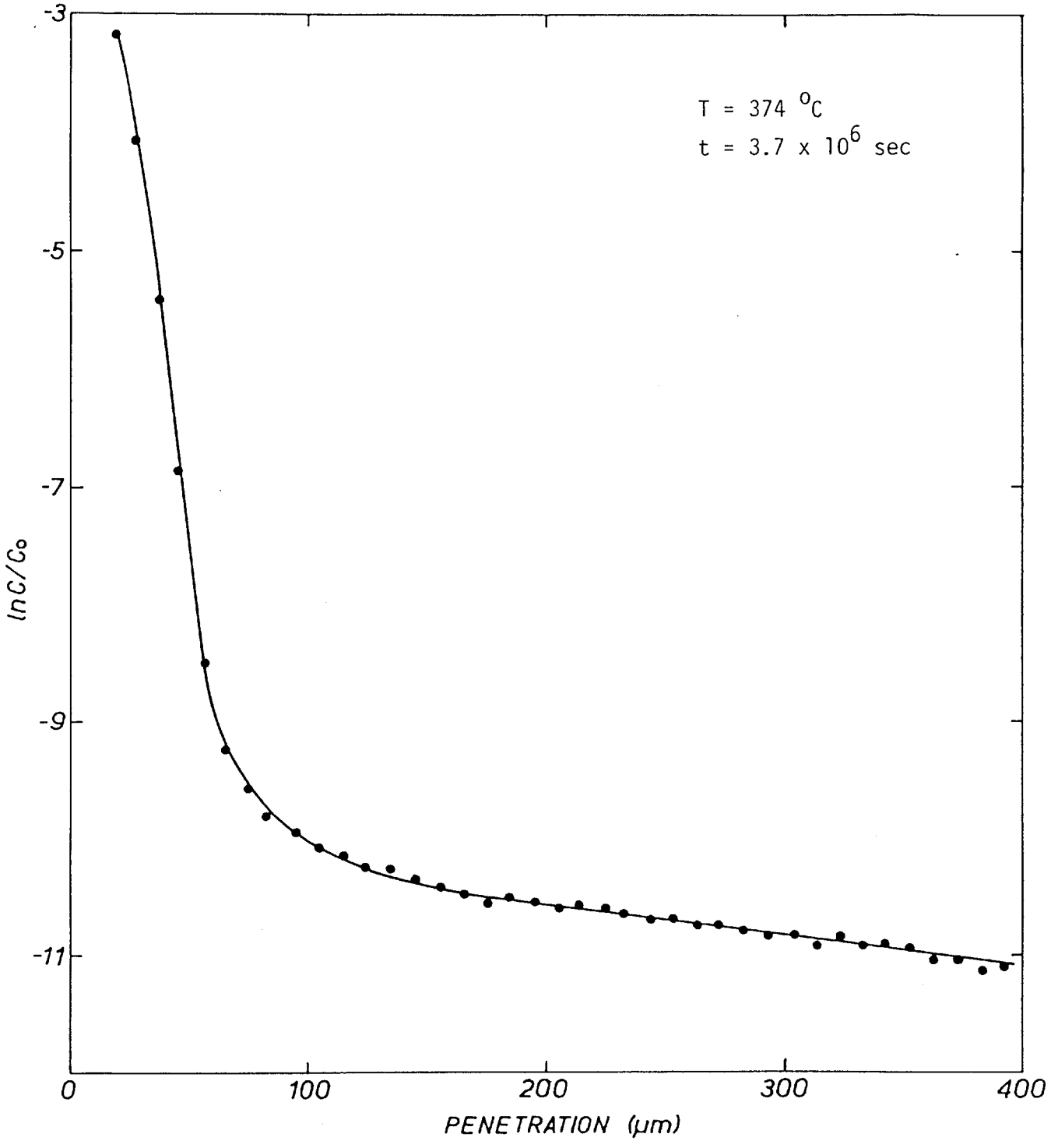


FIG.5.12 Diffusion profile of Run 1

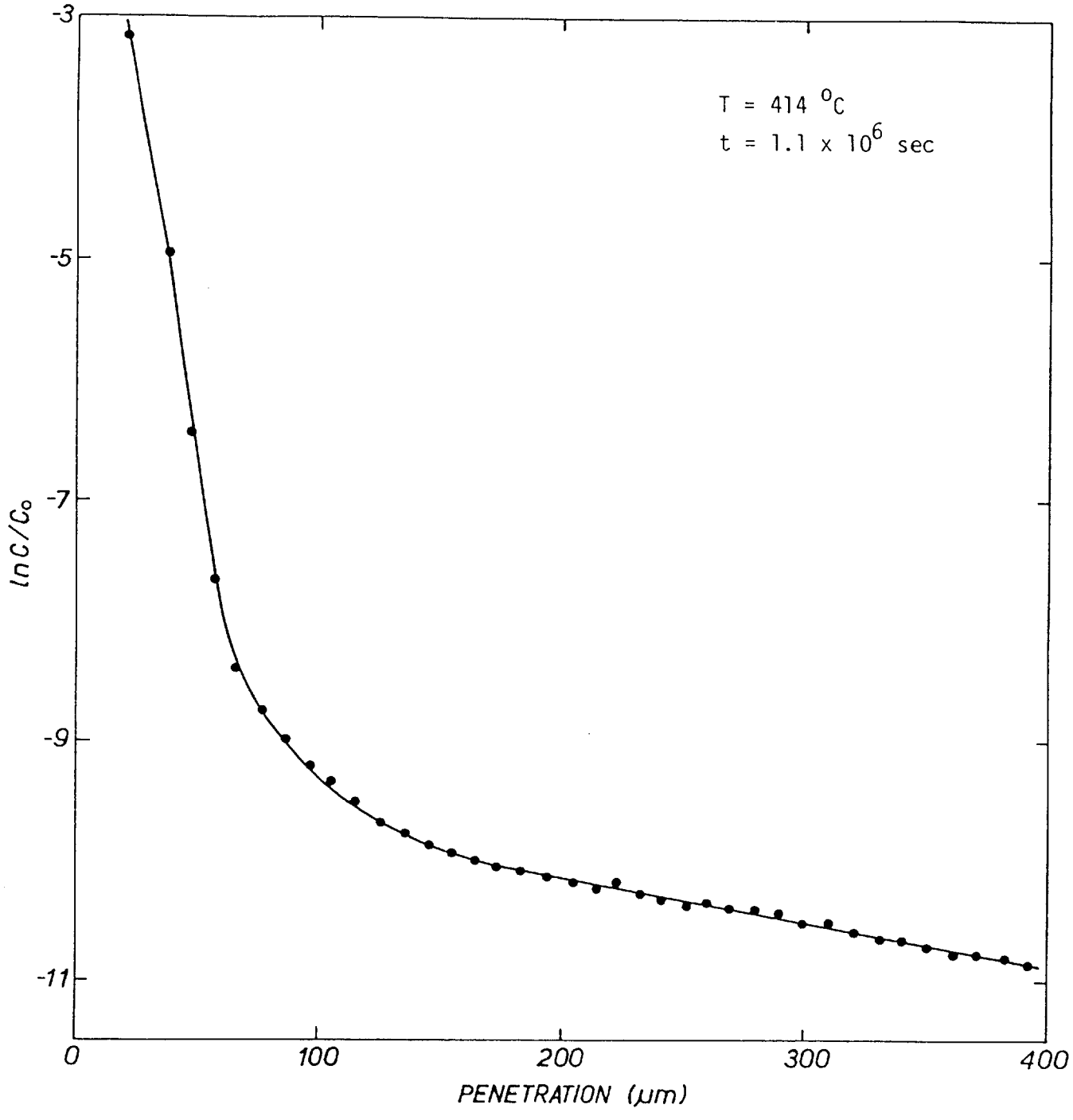


FIG.5.13 Diffusion profile of Run 2

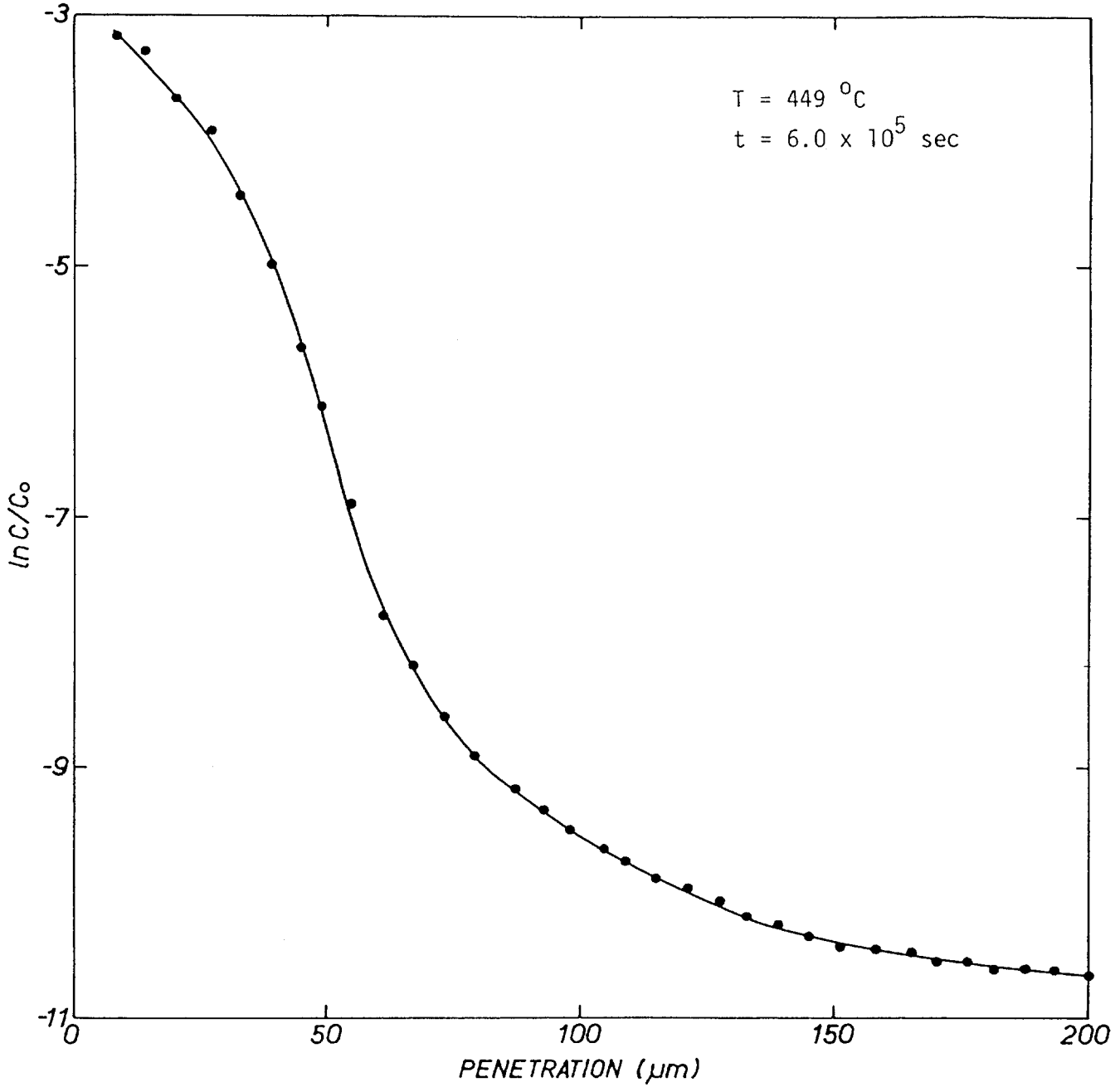


FIG.5.14 Diffusion profile of Run 3

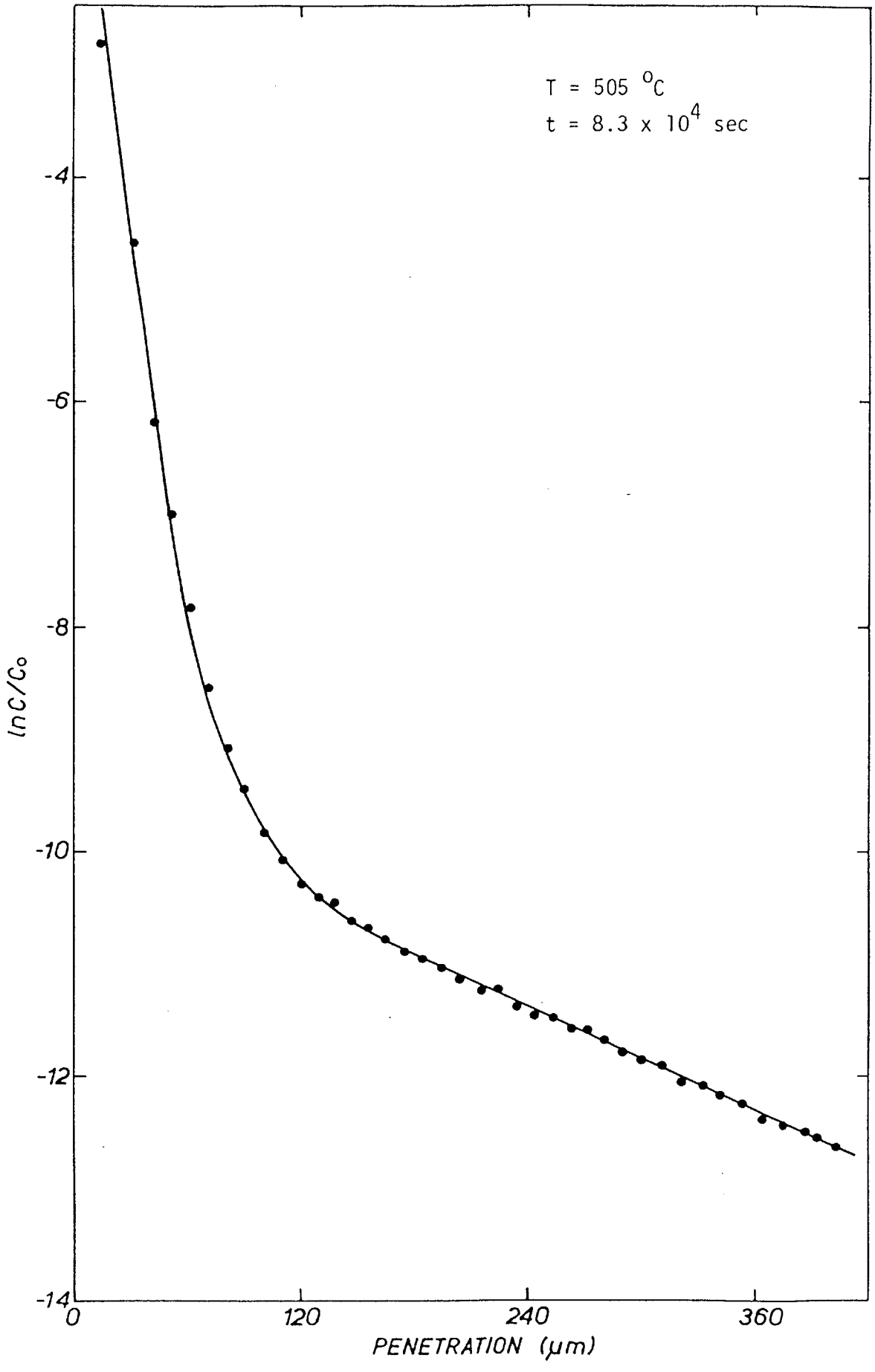


FIG.5.15 Diffusion profile of Run 4

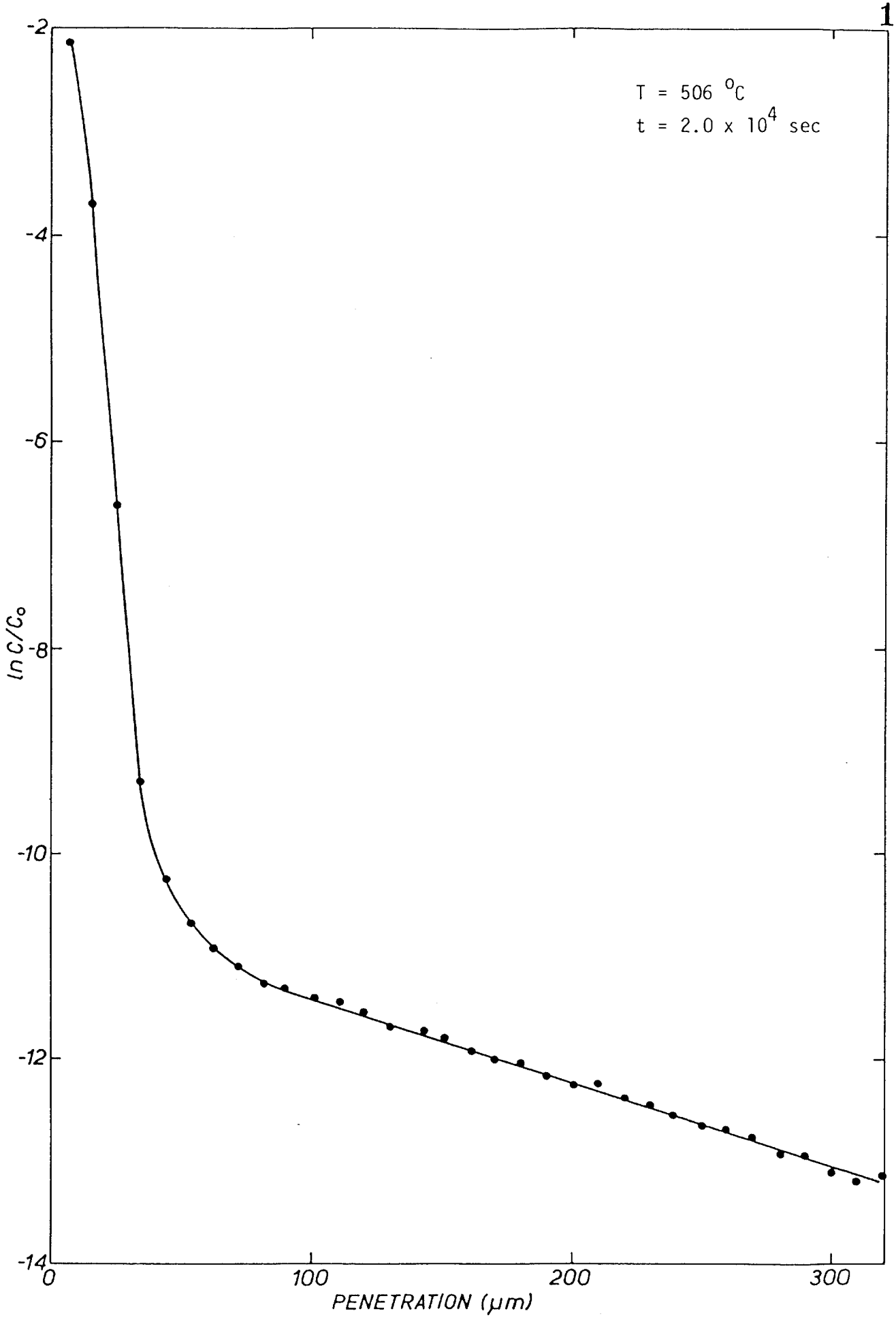


FIG.5.16 Diffusion profile of Run 5

The tracer layer thickness of all specimens was calculated to be around 0.3 μm (see Appendix IV), which justifies the use of the thin source condition in the analysis of the diffusion results. There is generally a slight decrease in the concentration of the tracer at the beginning of the diffusion profiles, which may be a result of local depletion of the thin source in regions where dislocations emerged at the surfaces, due to faster transport down the dislocations than elsewhere. Most specimens were sectioned to a total penetration of 300 - 400 μm, where the concentration of tracer was found to be a few times that of the background counts. The basic assumption of tracer diffusion in a semi-infinite specimen is justified for such penetration distances in specimens about 7 mm thick.

The diffusion distance, $(Dt)^{\frac{1}{2}}$, was conveniently set at ~11 μm for most experiments to enable an easy comparison of the various experimental results. Run 5 was carried out at nearly the same temperature as Run 4 but with a shorter diffusion time, resulting in a $(Dt)^{\frac{1}{2}}$ value of about 5 μm. The aim was to study the effect of diffusion time on the gradient of the 'tail' portion of the diffusion profiles.

5.5.1 Lattice diffusion

Figs.5.17 - 5.21 show the plots of $\ln C/C_0$ versus $(\text{penetration})^2$ which resemble the initial features of the plots shown in Fig.5.12 - 5.16.

In all the plots, $\ln C/C_0$ is shown to vary linearly with $(\text{penetration})^2$ over relatively shallow penetration distances. From the slope of the linear region, the lattice diffusion coefficient D

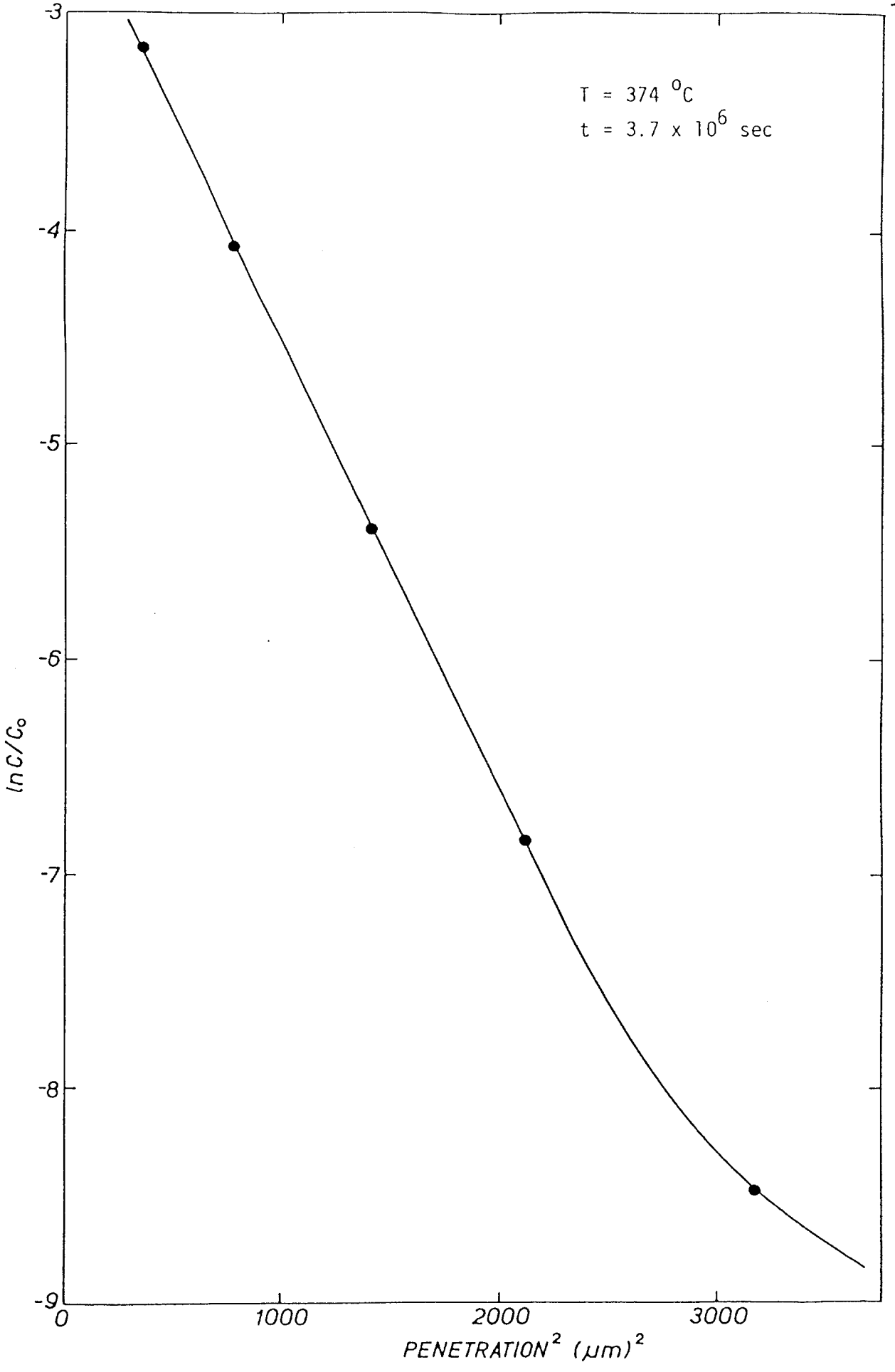


FIG.5.17 Lattice diffusion profile of Run 1

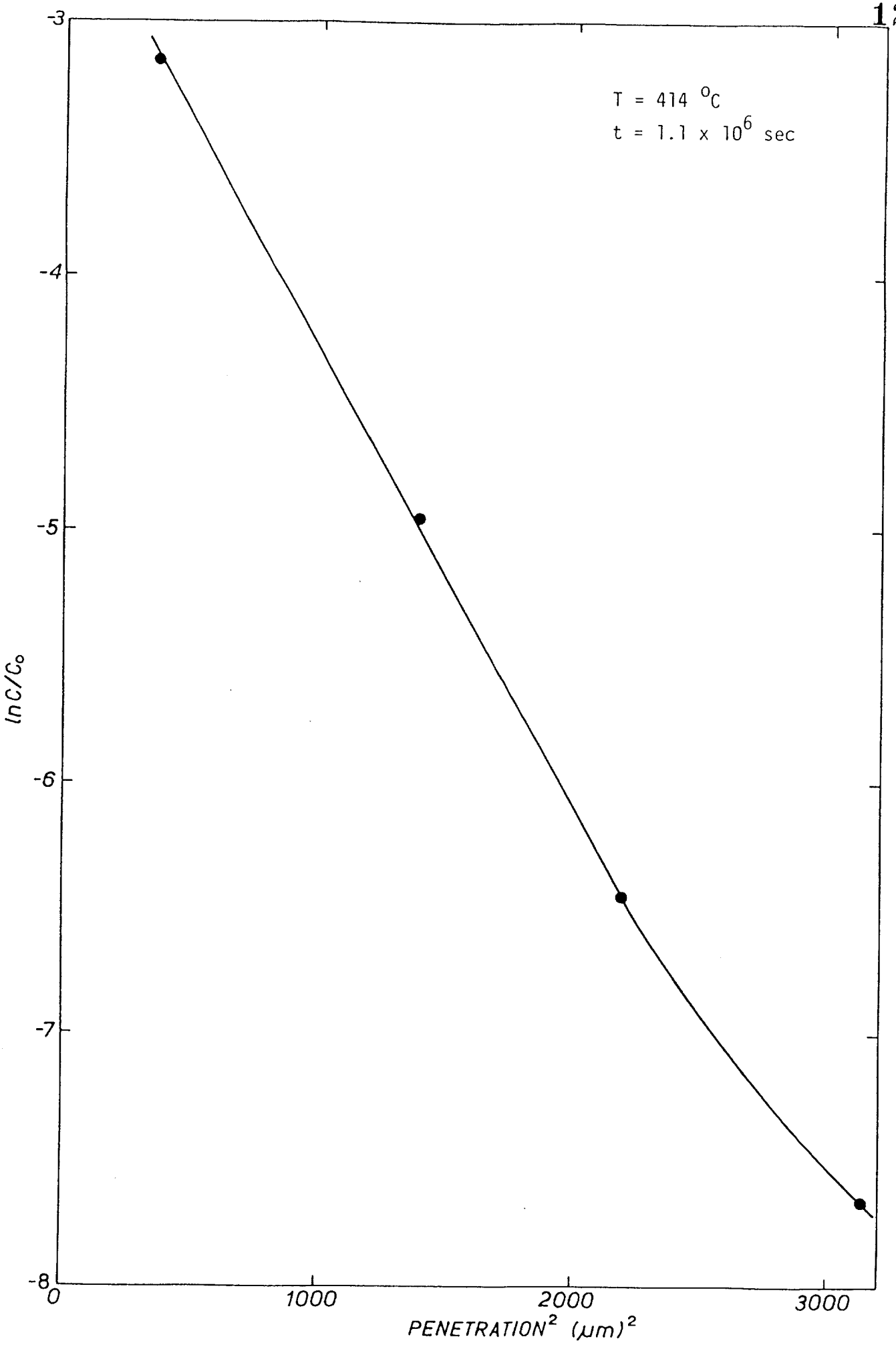


FIG.5.18 Lattice diffusion profile of Run 2

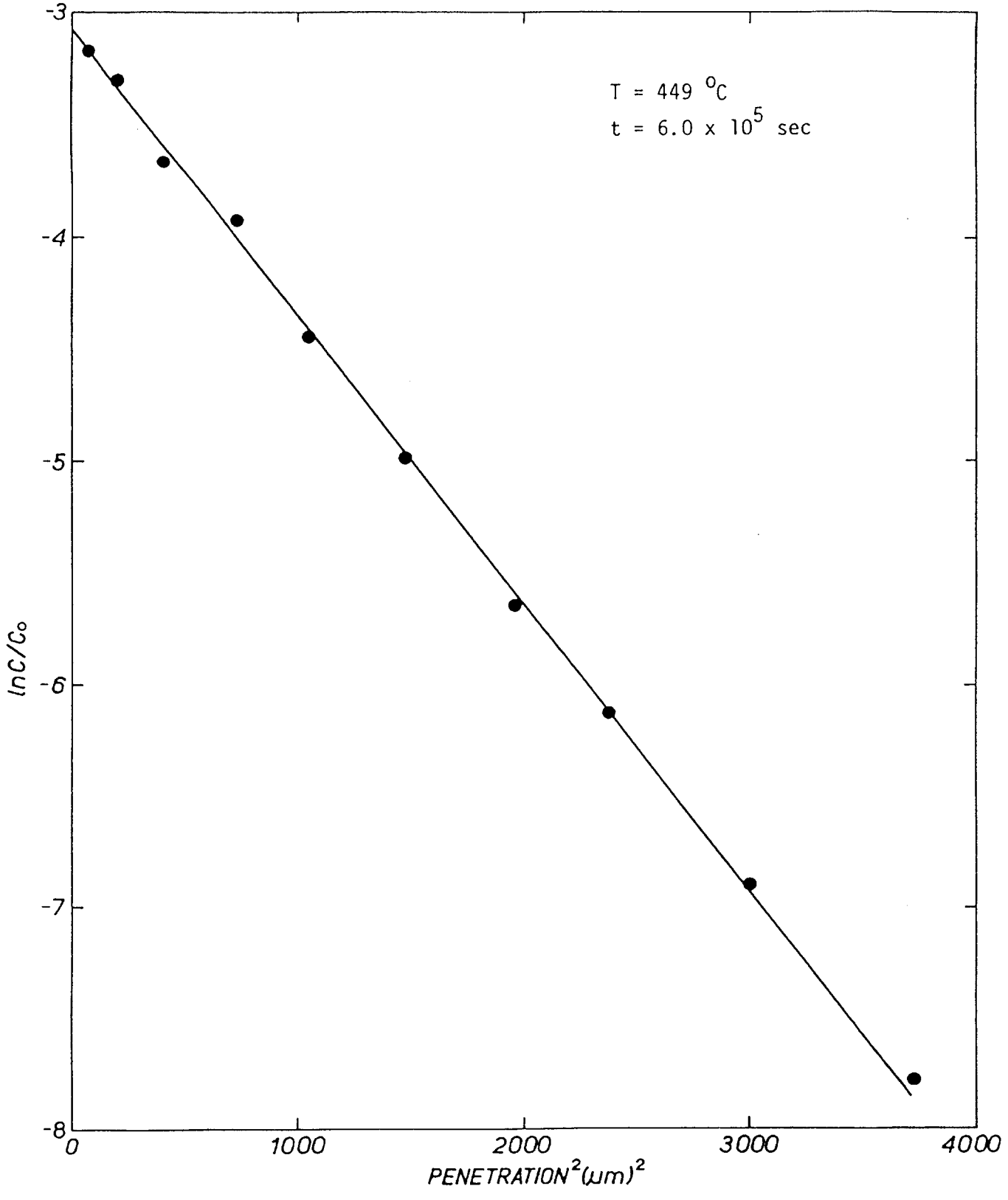


FIG.5.19 Lattice diffusion profile of Run 3

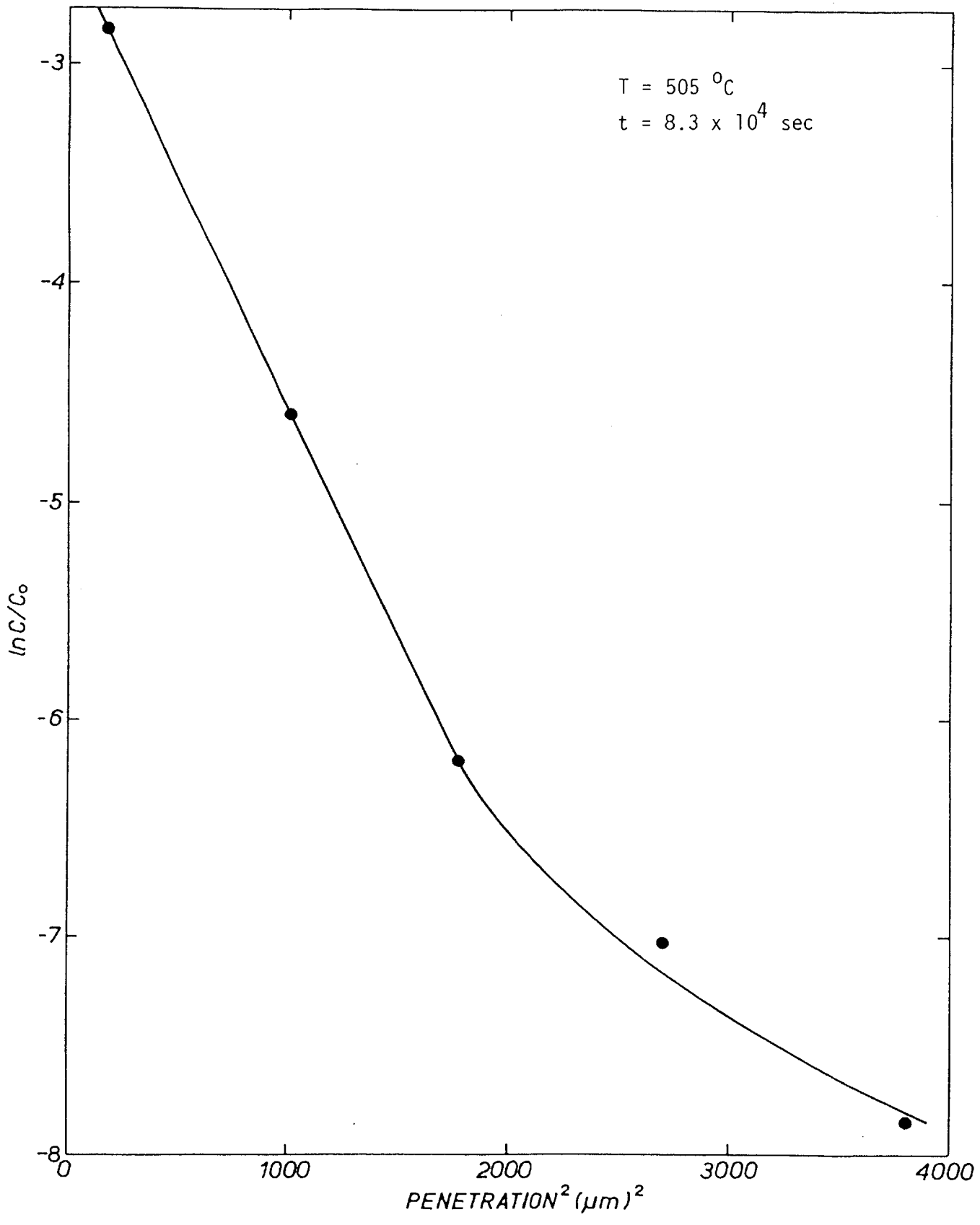
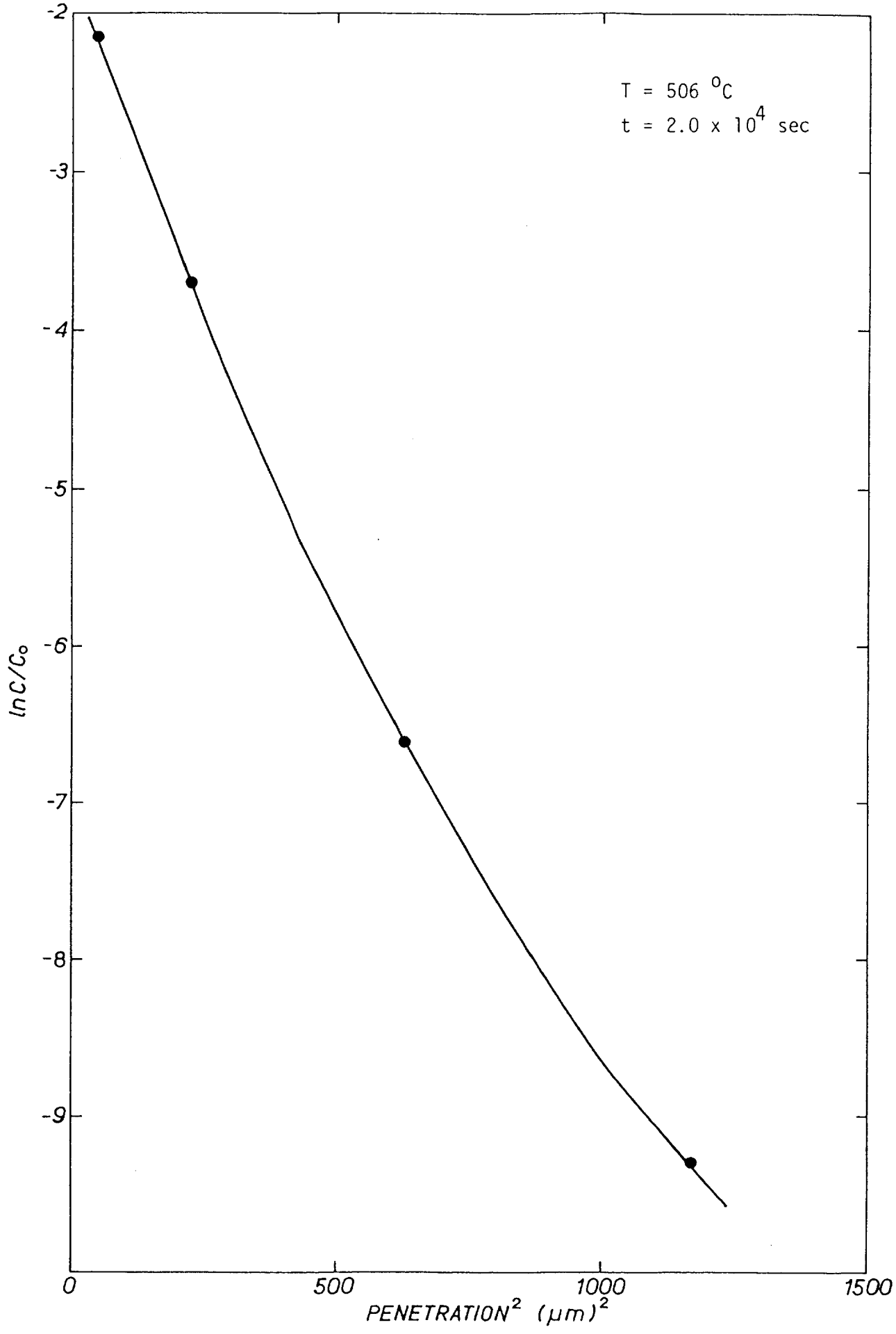


FIG.5.20 Lattice diffusion profile of Run 4



5.21 Lattice diffusion profile of Run 5

was calculated, the linear regions corresponding only to the initial 3 or 4 points of the plots. More points could have been obtained in these regions by sectioning the specimens into thinner slices. However, it has already been shown in the previous chapter that in so doing larger errors are incurred in determining the section thickness using the weighing method. In the present work, the errors involved in determining the values of D from the gradients of linear regions were very small, the highest being ±3.1% in Run 3.

The Arrhenius plot of ln D versus 1/T for Runs 1 - 4 is shown in Fig.5.22, and from the slope, the activation energy for lattice diffusion was found to be 1.25 ± 0.02 eV. The general expression for lattice diffusion in sodium chloride over the temperature range 374 °C - 505 °C is given by

$$D = 1.77 \times 10^{-3} \exp\left[-\frac{1.25 \pm 0.02}{kT}\right] \text{cm}^2 \text{ sec}^{-1} \qquad 5.5$$

The value of D in Run 5 at 506 °C was calculated from the above equation, since the diffusion distance $(Dt)^{\frac{1}{2}}$ was too short for reliable determination from the corresponding ln C/C_o versus $(\text{penetration})^2$ plot. The calculation is reasonable as the specimen in Run 5 is of similar purity to that of the specimens used in other runs.

From the conductivity plot of a specimen similar to that used in Run 3, the diffusion temperature range of 374 °C - 506 °C was found to be within the extrinsic region, as shown in Fig.5.11.

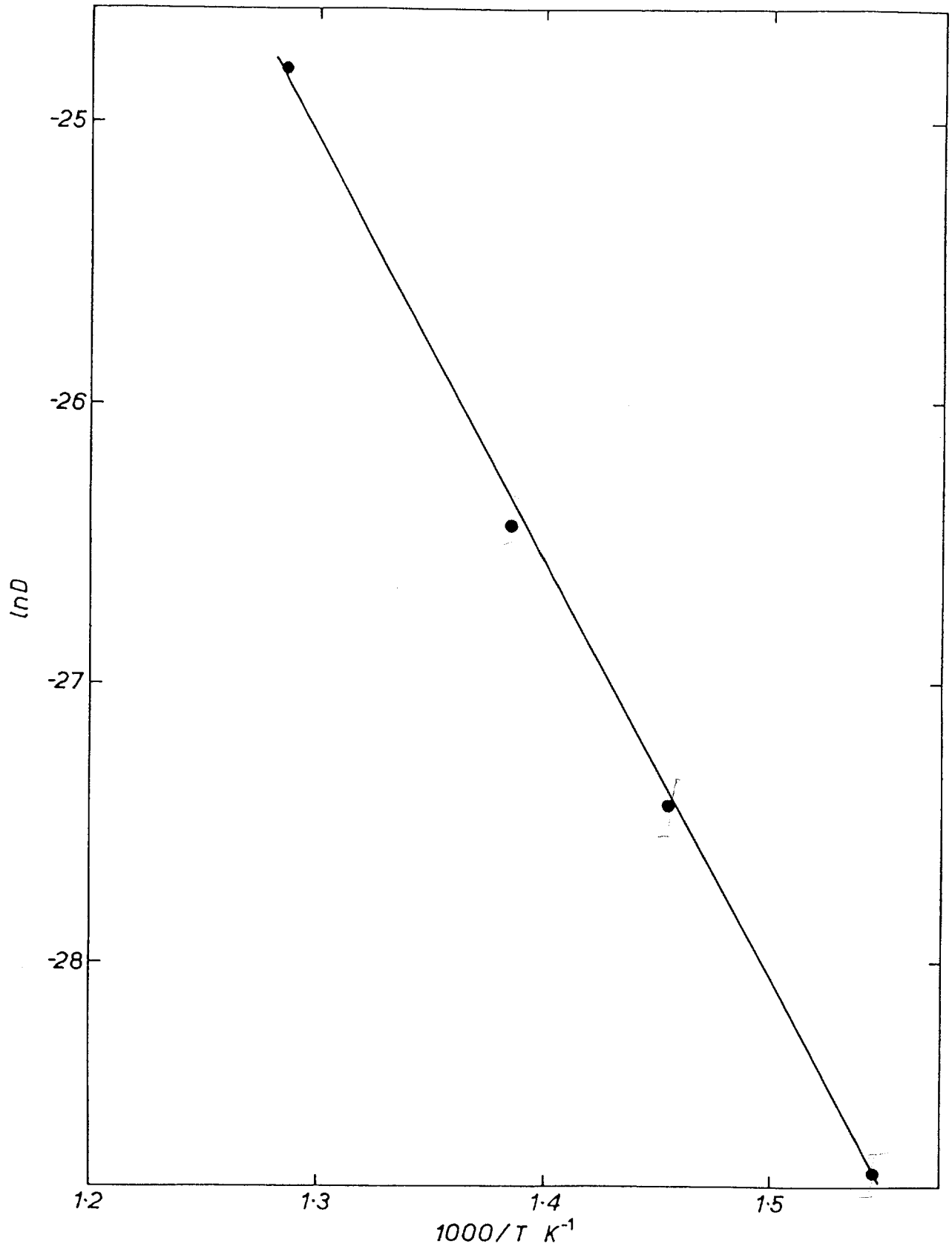


FIG.5.22 Arrhenius lattice diffusion plot of NaCl crystal

This is further supported by the fact that the coefficients of lattice diffusion, D, for the different experiments, are well represented by the single Arrhenius Equation 5.5, indicating that lattice diffusion in this temperature range is via the same mechanism. The energy of migration, Hm, is the same as the activation energy of diffusion in this extrinsic region, and is equal to 1.25 ± 0.02 eV.

The diffusion profiles of Runs 1 - 5 consistently show that the region over which lattice diffusion predominates extends to a penetration distance of $\sim 4(Dt)^{\frac{1}{2}}$, where the tracer concentration relative to the surface concentration is 10^{-3} - 10^{-4}. The region beyond starts to show signs of diffusion enhancement by the random distribution of dislocations in the crystal.

5.5.2 Isolated-dislocation diffusion

In the diffusion profiles of Runs 1 to 5, shown in Fig.5.12 - 5.16, the lattice diffusion dominated region extends to a relatively shallow penetration distance of $\sim 4(Dt)^{\frac{1}{2}}$. Thereafter, there is further penetration to a distance of $\sim 8(Dt)^{\frac{1}{2}}$, via the combined effect of lattice diffusion and dislocation diffusion, with the latter becoming more pronounced with increased penetration. At a penetration distance of $\sim 12(Dt)^{\frac{1}{2}}$ from the surface, lattice diffusion becomes insignificant and it is suggested that diffusion from this region is mainly via dislocations. This region corresponds to the linear tail of the diffusion profile.

LeClaire (86) has pointed out that in isolated dislocation diffusion, the gradient of the diffusion tail should be nearly independent of the diffusion annealing time, at constant diffusion

temperature, as is shown in Eqn.3.35. For grain boundary diffusion, the slope of the corresponding tail is proportional to $t^{-\frac{1}{4}}$. Thus measurements of the slopes as a function of time provide a means of distinguishing experimentally between tails due to diffusion down isolated dislocations, and tails due to diffusion down dislocations closely arrayed into boundaries or walls. The diffusion anneal in Run 5 was carried out at 506 °C for $5\frac{1}{2}$ hours which corresponds to a lattice diffusion distance $(Dt)^{\frac{1}{2}} \sim 5.4$ μm. The diffusion profile obtained is compared with that of Run 4, at 505 °C for 23 hours, in Fig.5.24. The diffusion time of Run 5 was so chosen that the gradient of the tail should show a 40% change from that of Run 4, if diffusion occurred down boundaries. This would be far in excess of any experimental error, and could confirm unambiguously whether the diffusion tail was the result of boundary diffusion. The results showed a tail gradient of $(7.72 \pm 0.24) \times 10^{-3}$ in Run 4, and $(8.28 \pm 0.33) \times 10^{-3}$ in Run 5. The difference of 6.8% was found to lie just within experimental error, and is far from the 40% difference expected for boundary diffusion. This and the linearity of the penetration plot indicates quite reliably that the tails of the profiles are the result of diffusion down isolated dislocation pipes.

From micrographic dislocation density measurements, the average spacing between each dislocation, d, was found to be ~100 μm. This is well above the value for $(Dt)^{\frac{1}{2}}$ of ~ 11 μm, and satisfies the condition $2(Dt)^{\frac{1}{2}} \ll d$ for dislocations to act independently. This is in good agreement with results previously observed. From some micrographs, d was found to be < 20 μm in some areas of the specimens, noticeably at sub-boundaries. This could account for the difference

of 6.8% in the gradients of the tails in Runs 4 and 5. Nevertheless, the major observation of the micrographic studies was one of isolated-dislocation.

The use of Fisher's, Whipple's or Suzuoka's solutions for the analysis of the present experimental results would be inappropriate, as they are concerned with diffusion in grain boundaries. Solutions for the analysis of isolated dislocation-pipe diffusion have been provided by many workers. The limits of application of these different solutions have been discussed in Chapter Three. LeClaire's solution appears the most appropriate for analysing the present diffusion results, and to determine the various diffusion parameters from the diffusion profiles obtained.

From Eqn.3.35 of LeClaire's solution for dislocation pipe diffusion, the normalised gradient of the diffusion tail is equal to $A(\alpha)/(\alpha\beta)^{\frac{1}{2}}$. $A(\alpha)$ is a weak function of α and is insensitive to $\alpha\beta$, as shown in Fig.3.9. Changing the value of α by an order of 10^4 only changes $A(\alpha)$ by a ~~magnitude~~ order of 2. The value of $(\alpha\beta)^{\frac{1}{2}}$, hence a^2D_d, can be calculated with reasonable accuracy if an appropriate estimate of a, the radius of the dislocation pipe, can be made. It is generally assumed that the value, a, for a metal is $\sim$5A°, while in alkali halides, there are reports that the value a can be as large as 10^{-4} cm due to the space charge effect (see discussion in next section). It is reasonable to assume that the value, a, in NaCl lies between these two limits. For present purposes, "a" was given the value 10^{-5} cm, which was used to calculate the diffusion parameters listed in Table III.

Table III. Values of the parameters calculated from the diffusion profiles at different temperatures

	Temperature in °C				
	374	414	449	505	506
Diffusion time in sec	3.7098×10^{6}	1.1160×10^{6}	5.9940×10^{5}	8.2800×10^{4}	1.9800×10^{4}
D in $cm^2\ sec^{-1}$	$(3.24 \pm 0.02) \times 10^{-13}$	$(1.23 \pm 0.02) \times 10^{-12}$	$(3.28 \pm 0.10) \times 10^{-12}$	$(1.44 \pm 0.01) \times 10^{-11}$	1.46×10^{-11}
$(Dt)^{\frac{1}{2}}$ in 10^{-4} cm	10.96	11.70	14.02	10.94	5.36
α or $a(Dt)^{-\frac{1}{2}}$ (assuming $a = 10^{-5}$ cm)	9.12×10^{-3}	8.55×10^{-3}	7.13×10^{-3}	9.14×10^{-3}	1.87×10^{-2}
gradient of the "tail"	$(2.75 \pm 0.28) \times 10^{-3}$	$(3.78 \pm 0.22) \times 10^{-3}$	$(4.68 \pm 0.93) \times 10^{-3}$	$(7.72 \pm 0.24) \times 10^{-3}$	$(8.28 \pm 0.33) \times 10^{-3}$
$\ln Q_{ex}^{II}$	6.10	6.68	7.27	7.15	5.30
$\ln C_{ex}\ C_{int}$	-10.02	-9.38	-9.73	-9.54	-10.57
$\ln C_o$	-2.46	-2.43	-3.20	-2.56	-1.76
$A(\alpha)$	0.655	0.650	0.640	0.660	0.710
dislocation density or $\rho_{calculated}$ cm^{-2}	3720	3800	3250	2310	2370
$\alpha\beta$	471	216	95	61	257
a^2D_d/D in cm^2	5.65×10^{-4}	2.95×10^{-4}	1.87×10^{-4}	7.31×10^{-5}	7.36×10^{-5}
a^2D_d in $cm^4\ sec^{-1}$	$(1.83 \pm 0.32) \times 10^{-16}$	$(3.62 \pm 0.43) \times 10^{-16}$	$(6.12 \pm 1.67) \times 10^{-16}$	$(1.06 \pm 0.07) \times 10^{-15}$	$(1.07 \pm 0.09) \times 10^{-15}$

It should be noted that the values of a^2D_d calculated for Runs 4 and 5 at nearly the same temperature are $(1.06 \pm 0.07) \times 10^{-15}$ cm^4 sec^{-1}, and $(1.07 \pm 0.09) \times 10^{-15}$ cm^4 sec^{-1}, respectively. The good agreement of the two values indicates the accuracy and the reproducibility of the present diffusion experiments.

The logarithmic plot of a^2D_d versus the reciprocal of absolute temperature is shown in Fig.5.23; the best fit provides the following general expression for dislocation-pipe diffusion in the extrinsic temperature range of 374 °C - 506 °C,

$$a^2D_d = 5.35 \times 10^{-12} \exp\left[-\frac{0.57 \pm 0.04}{kT}\right] cm^4\ sec^{-1} \qquad 5.7$$

From the equation above, if the value a is assumed to be the upper limit of 10^{-4} cm, the value of D_d at, say 374 °C, is 10^{-8} cm^2 sec^{-1}. However, if a $\sim$5 A°, then D_d has the very high value of $10^{-2} cm^2$ sec^{-1}. Such a high diffusion rate is physically impossible, being more appropriate for diffusion in the liquid state. Until there is evidence of a more realistic value for the radius of a dislocation-pipe, a, it is better to adopt the product value a^2D_d.

In the previous chapter, it has been shown that using the tail-extrapolation method of LeClaire's solution for dislocation diffusion, the density of dislocations, ρ, of the specimen can be fairly reliably determined from the diffusion profile. This has the symbol ρ_c to distinguish it from the dislocation density ρ_m observed in etch-pit micrographs.

The tracer concentration (relative to the surface concentration) at which the tails appear is in the order of 10^{-5} for all experiments. This indicates that a calculated dislocation density of the order

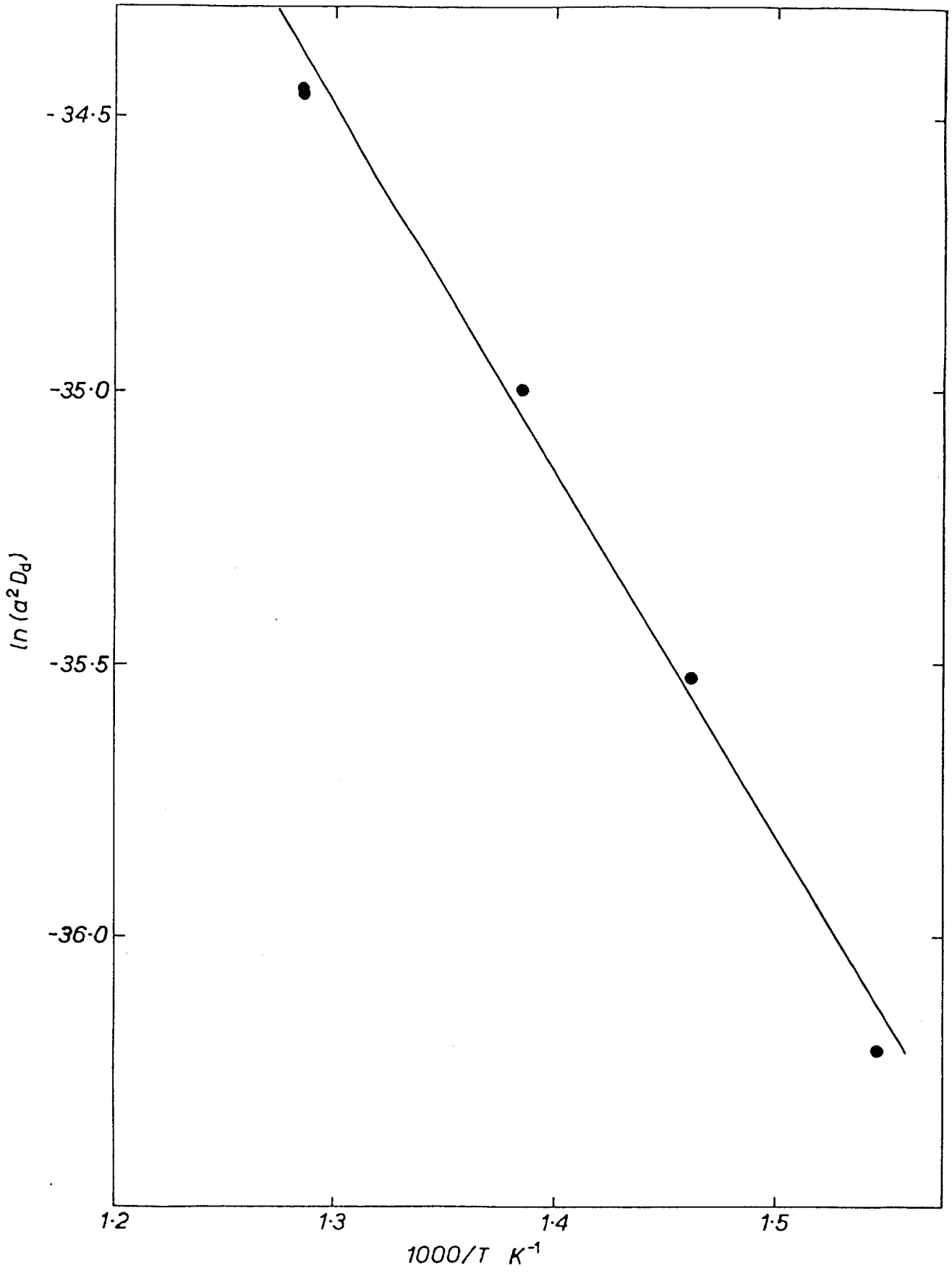


FIG.5.23 Arrhenius dislocation diffusion plot of NaCl crystal

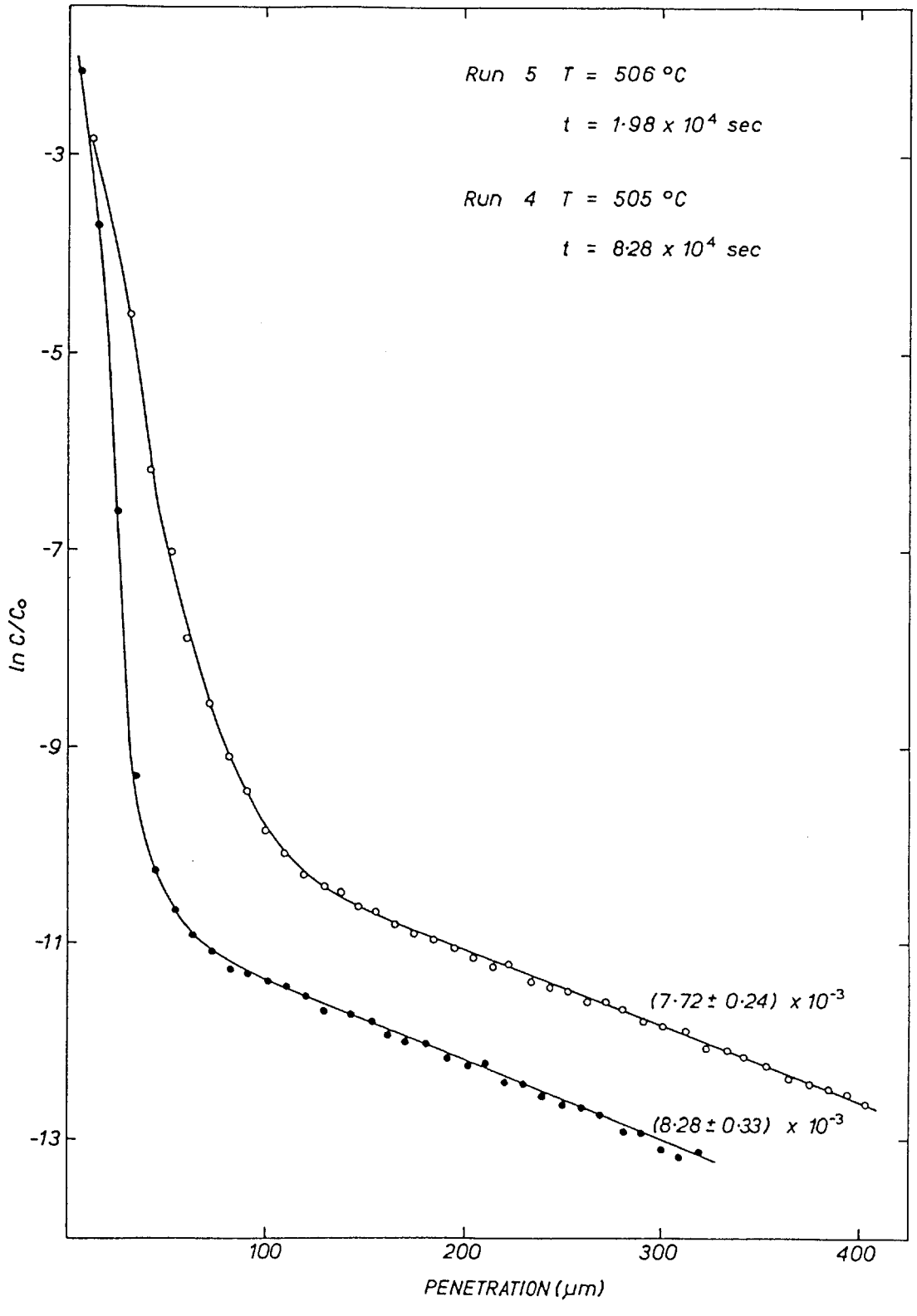


Fig.5.24. Comparison of the diffusion profiles of diffusion Runs 4 and 5.

3×10^3 cm^{-2} (as shown in Table III) was common to all the specimens used, which is reasonable since the procedures used for their preparation were identical. However, the value of ρ_m observed from etch-pit studies of the duplicate halves of the diffusion specimens, shown in Fig.5.10(a) - (c) was of the order 10^4 cm^{-2}. Such a discrepancy could be due to an overestimation of ρ_m. In a well annealed crystal, dislocations may form a network known as a Frank net (67). Thus the number of dislocations emerging at the surface of a crystal may be more than the number present inside the crystal. It has also been assumed throughout the present work that dislocations lie perpendicular to the surface of the specimen. However, since it is known that emerging dislocations are inclined at an angle to the specimen surface, the value of ρ_m observed at the specimen surface may be exaggerated by the factor $1/\cos\theta$. There is also the possibility that some dislocations are 'blocked' by impurities in the crystal, so that the number of effective dislocations for diffusion is reduced. Therefore, in the rest of this work, the value ρ_c is adopted as the actual dislocation density.

5.5.3 Space-charge effects on dislocation diffusion

Due to the ionic nature of alkali halides, dislocations in a crystal can be electrically charged by having an excess of jogs of one sign (34). If a dislocation is positively charged, it tends to attract the cation vacancies in its vicinity and eventually becomes surrounded by a cation vacancy cloud.

The amount of space-charge around dislocations is a function of temperature and the cation impurity content of the crystal. This is illustrated in Fig.5.25 where X_v' is the 'naive' concentration and is the concentration of cation vacancies inferred if the presence of

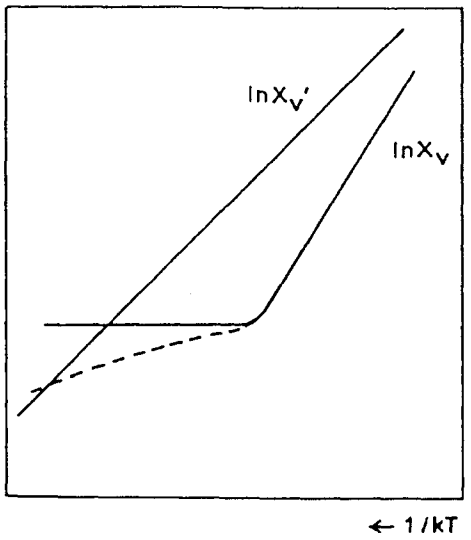


Fig.5.25. Logarithmic plot of cation vacancy concentration versus 1/kT (after Eshelby et al[34])

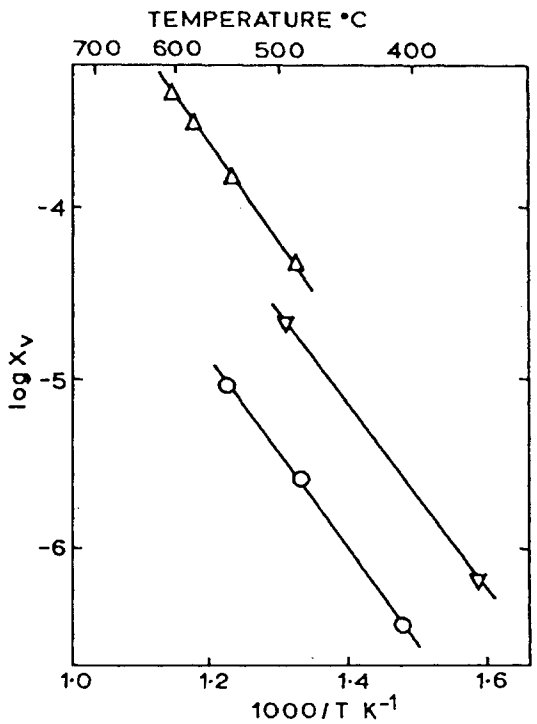


Fig.5.26. Observation of isoelectric temperature T_i in NaCl crystals with a free cation vacancy concentration X_V. o Davidge[29] ▽ Spencer and Plint[116] △ Kliewer and Koehler[76] (after Whitworth[129]).

impurities, and the requirement of bulk neutrality are neglected. The dotted curve is a more realistic representation of X_v, and takes into consideration the association effect of the cation impurities and cation vacancies. The vertical distance between the $\ln X_v'$ and $\ln X_v$ curves represents the amount of space-charge around dislocations.

In the intrinsic temperature range, the number of charges on the dislocations is thermally controlled and increases with decrease in temperature, thus expanding the size of the surrounding space-charge cloud. In the extrinsic temperature range, the presence of divalent impurities modifies the magnitude of charge on the dislocations and reduces the size of the space-charge cloud with decrease in temperature. At lower temperatures, some of the impurities may start to associate with vacancies and precipitate as a new phase, thus reducing the concentration of impurity which takes part in charge-cloud formation. At the isoelectric point, the dislocations become electrically neutral and reverse sign with further decrease in temperature.

The excess cation vacancies surrounding the dislocations may contribute significantly to the faster diffusion of the tracer ions down the dislocation path. Therefore, the effective dislocation pipe radius includes the area of misfit at the core plus the space-charge region around it. In metals, due to the lack of a screening cloud around dislocations, the radius of a dislocation pipe a is generally considered to be about 5 A°. In alkali halides, the space charge region extends well into the good lattice, and the radius of the effective dislocation pipe depends strongly on the impurity level of the crystal. The range of values of a reported is from 200 A° to more than 1 μm. Kliewer and Koehler (75) have suggested

that the value of a in the extrinsic temperature range is determined by

$$a = \left[\frac{\varepsilon kT}{8\pi Ne^2 X_v}\right]^{\frac{1}{2}} \qquad 5.8$$

where ε is the dielectric constant, e is the electrical charge, N is the total number of cation sites, and X_v is the concentration of free cation vacancies. Kliewer and Koehler reported values of a in pure NaCl of $\simeq$80 A° at 900 °K and 2000 A° at 600 °K (75,87). They further proposed that the nearly micron-size value of a at 600 °K is valid only when the divalent impurity concentration is $<$0.01 ppm, and thus the bulk cation vacancies are predominantly thermal (Schottky) defects.

In the extrinsic temperature range, Eshelby et al. (34) reported that the isoelectric temperature T_i of the space charge effect is given by

$$T_i = H_f^+/k \ln(C^{-1}) \qquad 5.9$$

where H_f^+ is the formation energy of a cation vacancy and C is the concentration of divalent cation impurities. Eshelby further suggested that H_f^+ has a value of about one quarter the formation energy of an anion vacancy. In the present work, the formation energy of a Schottky pair of vacancies was found to be 2.27 eV, and C $\sim$1.2 ppm. Using Eqn.5.9, T_i was calculated as 112 °C, well below the range of temperatures used in all the diffusion experiments. The isoelectric temperature in NaCl crystals has been studied by many workers, and was reviewed by Whitworth (129). This is illustrated in Fig.5.26. For the present value of C $\sim$1.2 ppm, T_i was found to lie between 350° - 440 °C. This implies a value for the

energy of formation of a cation vacancy, H_f^+, of ~0.8 eV or half that of H_f^-. For the time being, T_i is assumed to lie between 112 °C - 440 °C.

Lidiard (89) suggested that, for alkali halides with a low concentration of divalent cation impurities, the degree of association in the extrinsic temperature range is given by

$$p = 1 - \frac{1}{y}\left[-1 + (1 + 2y)^{\frac{1}{2}}\right] \qquad 5.10$$

where $$y = \exp\left[\frac{T_o}{T} + \ln(2zc)\right] \qquad 5.11$$

and $$T_o = \frac{e^2}{\varepsilon r_o k} \qquad 5.12$$

there, r_o is the nearest neighbouring distance of the ion in its sublattice and z is the co-ordination number of the crystal. These equations were applied to the present work to calculate p at the different diffusion temperatures, and the radius of the space charge region, a, was determined from Eqn.5.8, the results being listed in Table IV below.

Table IV. Values of degree of association p and radius of the space-charge cloud, a, at different temperatures.

Temperature in °C	p in %	a in A°
374	28.90	268
414	19.80	260
449	14.00	244
505	8.08	259

Yan (133) suggested that when the above equations are used the value of a is much smaller than that estimated by most workers. However, at the diffusion temperatures used, it is realistic to suggest that a ∿260 A° is the lowest possible limit for the dislocation pipe radius in a sodium chloride crystal.

The value a appears to remain quite constant over the extrinsic temperature range of 374° - 505 °C. This is conceivable if the isoelectric temperature T_i is well below 374 °C. Intuitively the estimated range of T_i from Fig.5.26, i.e. 350 °C - 440 °C, is unrealistic since it implies that the space charge cloud diminishes to zero at that temperature. However, the value T_i ∿112 °C calculated from Eqn.5.9 in the present work appears to be quite realistic.

5.5.4 Comparison of conductivity and diffusion results with previous literature

The apparent migration energy of cation vacancies, H_m, in stage II of the extrinsic region was determined as 0.71 eV in the conductivity measurement of the present work. Table V shows the reasonable agreement between this value with those obtained by previous workers. However, from the diffusion studies of the present work, the value H_m was found to have the exceedingly high value of 1.25 eV. This discrepancy in the H_m values obtained from conductivity and tracer self-diffusion studies might imply that different mechanisms were active in the transport processes.

Table VI compares the values of the apparent migration energy H_m, and the pre-exponential term D_o, obtained by a number of workers. The value H_m ranges from 0.72 to 1.25 eV and D_o differs by 3 orders of magnitude. These discrepancies are believed to be related to the

Table V. Enthalpy of migration of cation vacancy in NaCl measured from conductivity

H_m in eV	Reference	
0.65	Rothman et al	(110)
0.66	Allnatt et al	(3)
0.68	Kirk and Pratt	(73)
0.71	This work	
0.72	Benière et al	(15)
0.72	Guerrero	(49)
0.74	Graham et al	(46)
0.75	Jain and Dahake	(68)
0.76	Brown and Hoodless	(20)
0.77	Quin et al	(105)
0.80	Dreyfus and Nowick	(32)
0.85	Etzel and Maurer	(35)
0.85	Kanzaki et al	(71)

Table VI. Values of D_o and H_m measured from the extrinsic region of self-diffusion of NaCl

Divalent cation impurity concentration	D_o in cm^2 sec^{-1}	H_m in eV	Reference	
27 ppm	3.53×10^{-6}	0.72	Benière et al	(15)
7 ppm	-	0.75	Riggs	(109)
Harshaw	1.6×10^{-6}	0.77	Mapother et al	(90)
1 ppm	3.55×10^{-6}	0.84	Reisfeld and Fredericks	(107)
-	2×10^{-6}	0.87	Guccione and Josi	(48)
12 ppm	6.5×10^{-5}	0.89	Benière and Chemla	(13)
5 ppm	6.0×10^{-5}	0.98	Benière and Chemla	(13)
ultrapure	6×10^{-4}	1.23	Schlederer	(112)
2 ppm	1.6×10^{-3}	1.24	Benière and Chemla	(13)
1 ppm	1.77×10^{-3}	1.25	This work	

purity of the material used. Benière et al (15) suggested that with an increase in the divalent cation impurity concentration, there is an increase in the association of divalent cation impurities with cation vacancies to form impurity-vacancy pair in the extrinsic region. The jump of Na^+ into an associated vacancy would be easier than a similar jump into a free vacancy due to the strained state of the complexes. This results in the lower apparent value of H_m in impure crystals. Similarly, with an increase in impurity concentration, there will be an increase in the migration entropy due to the more disordered state, thus reducing the value of D_o. However, the binding energy of a vacancy and a divalent cation impurity, say Ca^{++} (the most abundant cation impurity in the specimens of the present work) with the value 0.57 eV (12), has to be overcome to allow for the dissociation of the complex before the Na^+ can jump into such a relieved vacancy. To account for such an energy, and a further discrepancy in H_m of $\sim$0.5 eV in material of different purity, the strain energy released by dissociating such a vacancy-impurity cation complex must have a value of $\sim$1.1 eV. Such a large value seems most unlikely for sodium chloride crystals.

The possibility that the extrinsic diffusion in high purity NaCl crystals by vacancy pair mechanism has been investigated in this work. Economou and Sastry (33) reported that the migration energy of vacancy pairs is 1.25 eV which has the same value as the H_m observed in the present diffusion work. The formation of vacancy pairs is thermally controlled and has a formation energy value of 1.30 eV. Thus, the activation energy for diffusion by such a mechanism would be $\sim$2.55 eV which is much higher than the H_m observed in this work. Besides, there are doubts about the high concentration of vacancy pairs reported by Economou and Sastry, particularly at the relatively low temperatures employed in the present diffusion studies.

There is a further possibility that the active diffusion mechanism in the extrinsic region is the reorientation of the impurity-vacancy pairs. In crystals of high impurity concentration, there is an abundance of such impurity-vacancy pairs due to the higher degree of association. When these pairs are close enough to each other, the constant movement of these associated vacancies would form a pool of vacancies in their overlapping region. The transport of tracer from the surface to the interior of the crystal might be achieved by the reorientation of associated pairs. Barr and Lidiard (12) reported that the value of the activation enthalpy for such an effect is $\sim$0.6 - 0.7 eV, which is in close agreement with the value of H_m observed by many previous workers in self-diffusion studies of NaCl with high impurity levels. With an increase in the purity of the specimen, the number of such impurity-vacancy pairs is dramatically reduced, and additional energy is required to bind impurities and vacancies into pairs. With the additional binding energy of 0.57 eV for Ca^{++} - vacancy pair formation, the total activation enthalpy for the transport of the tracer in high purity crystals, by the reorientation effect of the pairs, will amount to $\sim$1.25 eV, which is in close agreement with the value of H_m observed in the present work. However, to account for the value H_m $\sim$1.0 eV in crystals of moderate purity, say $\sim$5 ppm, the binding energy of the pair has to be smaller than 0.57 eV. There are doubts that the binding energy of impurity-vacancy pairs is dependent on the impurity concentration of the crystal. Besides, with the smaller degree of association in a pure crystal, the transport of tracers is more likely to occur via the free-vacancy mechanism.

An attempt was made in the present work to correlate the lattice diffusion coefficient, D, at the various temperatures, with the corresponding conductivity σ in order to verify the correlation factor F

inserted in the Nernst-Einstein equation,

$$\frac{\sigma}{D} = \frac{Ne^2}{FkT} \qquad 5.13$$

Taking into consideration the degree of association at the respective temperatures, the value D does not appear to bear any direct relationship to the value σ as shown above, and the expected value of F = 0.7815 was not obtained. This had been similarly observed by Benière (15) in his self-diffusion and conductivity measurements of high purity NaCl specimens in the extrinsic region. He suggested that the conventional rigid lattice model of the crystal should be modified, and that the small volume enclosing the vacancy and the neighbouring atoms is in fact as disordered as in the liquid state. Therefore, the number of possible jumps of the tracer in the crystal could be considerably greater than 12. As a result, the conventional value of correlation factor is not observed. However, there is no experimental evidence to justify such a hypothesis and the conventional rigid lattice model is a more likely situation of the crystal.

It has been reported (16,64,69) that dislocations existing in the crystal contribute to the conductivity to different extents at different temperatures. The enhancement of the effective lattice diffusion coefficient D_{eff} by dislocations is represented in Hart's model as

$$D_{eff} = (1 - f)\, D + fD_d$$

where f is the fraction of atomic sites that are in the region of dislocations. In a well annealed crystal $f \ll 1$, and the above equation becomes

$$D_{eff} = D + \pi a^2 \rho D_d \qquad 5.14$$

Table VII. Values of the different parameters in Hart's equation of the present work.

Temp. in °C	a^2D_d in $cm^4\ sec^{-1}$	ρ_c * in cm^{-2}	$\pi a^2 \rho D_d$ in $cm^2\ sec^{-1}$	D in $cm^2\ sec^{-1}$
374	1.83×10^{-16}	3720	2.14×10^{-12}	3.24×10^{-13}
414	3.62×10^{-16}	3800	4.32×10^{-12}	1.23×10^{-12}
449	6.12×10^{-16}	3250	6.25×10^{-12}	3.28×10^{-12}
505	1.06×10^{-15}	2310	7.69×10^{-12}	1.44×10^{-11}

* the values of the dislocation density ρ_c of the different specimens were calculated from the extrapolation of the "tails" of the diffusion profiles (see Chapter 3.2). These values are not to be confused with the measured dislocation density ρ_m obtained from etch-pit micrographs.

where ρ is the dislocation density of the specimen. The values for the different parameters in Eqn.5.14 at the various diffusion temperatures are listed in Table VII. It is reasonable to assume that the correlation factor, or more appropriately the Haven ratio F_d, is around 0.5, for the jumping of tracers into vacancies in the dislocation paths. Using the established values of $F_1 = 0.7815$ for the jumping of tracer into vacancies in the lattice, the values of D_{eff} at different temperatures were calculated according to Eqn.5.14. These were then converted into the corresponding values of σT according to Eqn.5.13, using the value $N_e^2/k = 4.1 \times 10^7$ coulombs^2 cm J^{-1} K°, and are compared with the values of σT measured from the conductivity plot of Fig.5.11 in the table below.

Table VIII. Measured and calculated values of $\log(\sigma T)$ at different temperatures.

Temperature in °C	$\log(\sigma T)_{measured}$	$\log(\sigma T)_{calculated}$
374	-4.1644	-4.2657
414	-3.8186	-3.8928
449	-3.5664	-3.6321
505	-3.1743	-3.2144

The calculated and measured values of $\log(\sigma T)$ appear to be in good agreement. The small discrepancy may be due to the underestimation of the value F_d for tracer jumps in the dislocation paths. The exact values of F_d were then calculated by converting the values of $\log(\sigma T)_{measured}$ to D_{eff} according to Eqn.5.13, and further subtracting the lattice contribution D using $F_1 = 0.7815$. The results obtained are tabulated below.

Table IX. Values of F_d, the Haven ratio of dislocation contributions to conductivity at different temperatures.

Temperature in °C	F_d
374	0.6624
414	0.6343
449	0.6485
505	0.6571

Using the above information, the contributions of the dislocations and of the lattice to the conductivity at different temperatures were calculated, and are compared with the conductivity plot of Fig.5.11, as shown in Fig.5.27. The slope of the $\log(\sigma T)_D$ plot corresponds to an activation energy of 1.25 ± 0.02 eV which is in good agreement with the activation energy of stage II' in the main conductivity plot. Fig.5.27 shows that the summation of the values $\log(\sigma T)_D$ and $\log(\sigma T)_{D_d}$ reproduces the value of the conductivity on the main plot at any temperature.

It has been suggested in the previous section that the effective dislocation path for diffusion is the area of misfit in the dislocation core plus the space-charge cloud surrounding it. The radius of the dislocation core is only a few atomic spacing while the space-charge cloud essentially remains as a good lattice region. A more realistic value of F_d in the dislocation core might probably be smaller than 0.65, while the value F_d in the cloud should remain as 0.7815 as in the lattice. Since there is an uncertainty of the exact value of the radius of the space-charge cloud, it is not possible to calculate the exact contribution of the core and the cloud to conductivity with the more appropriate use of their F_d values. However, the radius of the space-

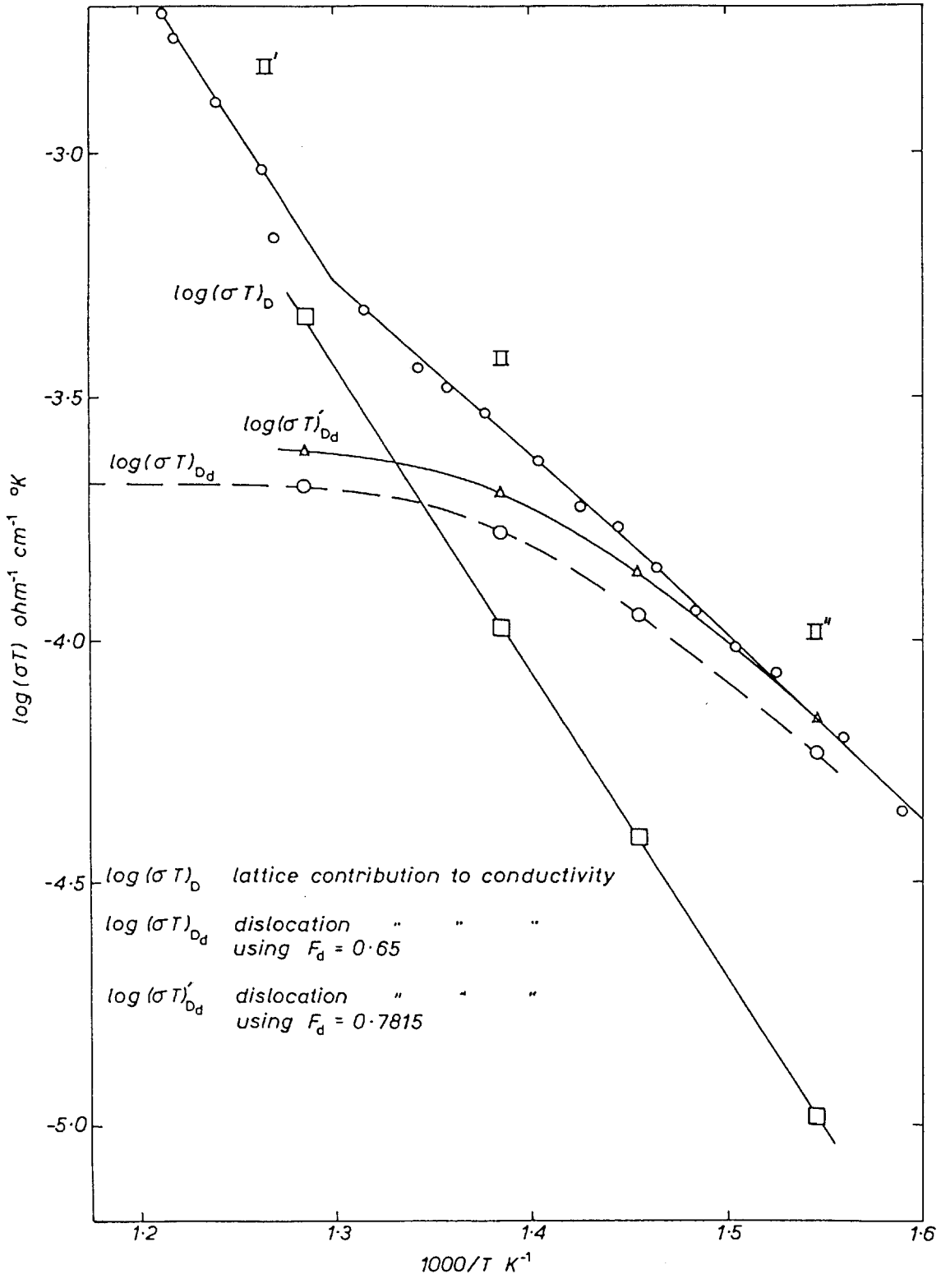


Fig.5.27. Lattice and dislocation contributions to conductivity.

charge cloud of several hundred angstroms is so much greater than the core's radius of ∿5 A°, it would then be reasonable to assume an overall F_d value of the effective dislocation diffusion path as 0.7815. With the present assumption, the dislocations contribution to conductivity is calculated and is shown as the $\log(\sigma T)'_{D_d}$ curve in Fig.5.27. The summation of this contribution and that of the lattice will amount to a value slightly greater than the value of $\log(\sigma T)_{measured}$. However, the amount of dislocation contribution to conductivity is sensitive to the dislocation density of the specimen (see later discussion). With the margin of error of the value of calculated dislocation density, ρ_c, it may then be possible to account for the small discrepancy between $\log(\sigma T)_{measured}$ and $\log(\sigma T)_{calculated}$.

It is reasonable to suggest that the relationship of the conductivity and the diffusion coefficient in the Nernst-Einstein equation is obeyed when the dislocation contribution to conductivity is considered. From Table VII, it is shown that the dislocation contribution to conductivity becomes less significant at higher temperature. This work implies that the true extrinsic region for impurity controlled conduction in the crystal lattice of NaCl is represented by stage II', while stage II is the extrinsic region for impurity-controlled conduction down dislocations. It is then reasonable to suggest that the migration energy of cation vacancies in NaCl is the activation energy of stage II', i.e. $H_m = 1.25 \pm 0.01$ eV. This is in exact agreement with the corresponding H_m value determined from the diffusion experiments of the present work.

From the information deduced above, the conductivity of NaCl should be sensitive to the dislocation density of the specimen used. With an increase in dislocation density, the dislocation contribution to conductivity will increase and the $\log(\sigma T)'_{D_d}$ curve will shift upward.

Fig.5.28 shows the theoretical estimation of such an effect by retaining the values of a^2D_d of the present work. It shows that with an effective $\rho > 2 \times 10^4$ cm^{-2}, stage II' of the conductivity plot will be masked. The determination of the activation energy in this extrinsic region will give a value similar to that for stage II in Fig.5.11. There is evidence that stage II' was observed by some previous workers. However, this region is usually overlooked (49,73) or is too small to produce reliable information.

The $\log(\sigma T)_{D_d}$ curve in Fig.5.27 appears to flatten out at high temperatures notably at ∿505 °C, which indicates that the dislocation contribution to conductivity may reach a constant value. However, it should be noted that the calculated contribution at 505 °C was based on a dislocation density smaller by a factor of ∿1.3 than the other three points at lower temperatures. With the proper adjustment of ρ at this temperature, the dislocation contribution will increase, and thus the adjusted $\log(\sigma T)_{D_d}$ curve will follow the general trend of the theoretically estimated curves of $\log(\sigma T)_{D_d}$ as shown in Fig.5.28.

If the isoelectric temperature T_i, for the NaCl crystals of the present work, is within the range of 350 °C - 440 °C as observed in Fig.5.26, the dislocation contribution to conductivity should diminish significantly with decreasing temperature and even give rise to a negative contribution to conductivity when $T < T_i$. However, the evidence that dislocations contribute positively to conductivity in the diffusion temperature range 374 °C - 505 °C, indicates that $T_i \ll 374$ °C. Thus the value T_i ∿112 °C calculated in the present work appears reliable.

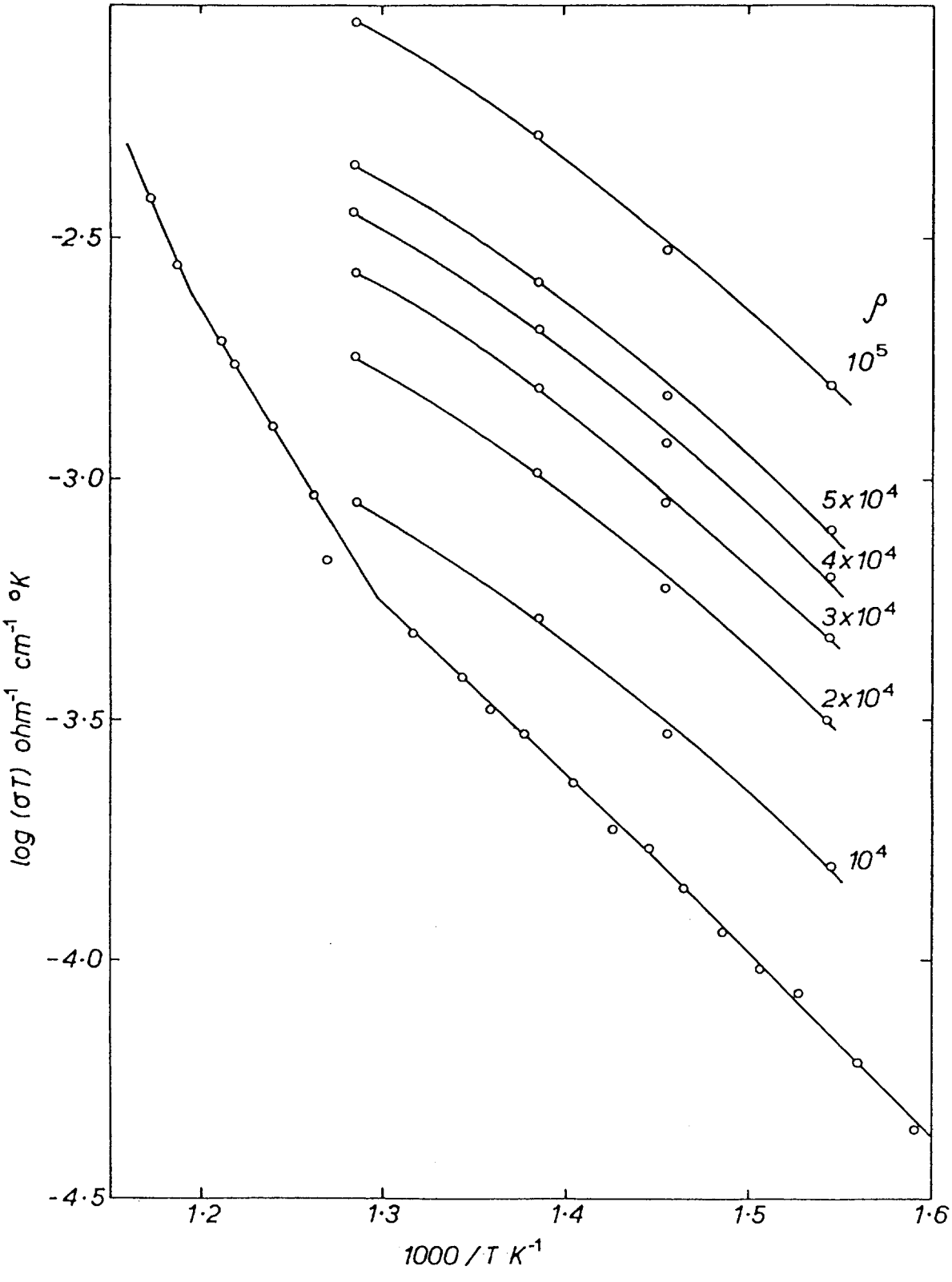


Fig. 5.28. Theoretical estimation of the dislocation contribution to conductivity as a function of dislocation density (ρ)

There have been many conflicting reports concerning the dislocation enhanced diffusion of cations in sodium chloride. Some workers did not detect enhanced diffusion at all, while others attributed different mechanisms to their observed enhancement. A number of factors may be contributing, i.e. the improper use of the diffusion solution, variation of the purity of the specimens, sensitivity of the detection techniques, etc.

Since the transport properties of alkali halides are structure-sensitive, it is essential to use material of high purity in the diffusion studies, in order to minimise the extrinsic effect of impurities. Many previous workers used crystals of nominal purity, in which impurity concentrations can be >10 ppm. Hence the suggestion (57) that the presence of the impurity precipitates in the extrinsic temperature range was the cause of the observed enhanced diffusion.

It is logical to expect the excess cation vacancies in the charge-cloud surrounding the dislocations to facilitate the tracer diffusion process. In the extrinsic temperature range, the size and thus the contribution of the cloud depends strongly on the purity level of the crystal. Using material of high impurity level greatly reduces the size and the contribution of fast tracer transport. Yan (133) reported a theoretical estimation of such a space-charge effect on diffusion, and suggested that the observation of cation dislocation diffusion is feasible for ultra-pure crystals. Mimkes (94) suggested that the impurity concentration should be <1 ppm. In the present work, the total divalent cation impurity content in the crystals was found to be 1.2 ppm. It is possible that some of this impurity was bound by anion impurity present, e.g. OH^-, so that the effective divalent cation impurity content in the crystals was <1 ppm.

In grain boundary diffusion experiments, it is important to keep the value $\beta > 10$ in order that the enhanced cation diffusion is observed. This can be achieved by keeping the diffusion time, t, short so that the lattice penetration distance $(Dt)^{\frac{1}{2}}$ is small. Hoodless and Thomson (64) observed no enhanced Na^+ grain boundary diffusion in their work at 511 °C, which is not surprising, since the long diffusion time of >200 hours they employed at such a high temperature, would give rise to a large value of $(Dt)^{\frac{1}{2}}$, and subsequently a small value of β. The same reasoning may explain a similar observation by Laurent and Bénard (80,81) in their high temperature diffusion studies.

Dislocation enhanced diffusion is observable only at relatively deep penetration distances when lattice diffusion becomes insignificant. In tracer experiments, this corresponds to a region where the tracer concentration, relative to the surface concentration, is very small. In the present work, the tracer concentration of this region was found to be $\sim 10^{-5}$ that of the surface. For the accurate detection of such a low activity, it is essential that the sensitivity of the detection technique, and the specific activity of the tracer, is high. A lack of these requirements may possibly account for the reported absence of any boundary diffusion by Klotsman (77). In the present work, a high activity of $\sim 40\,\mu Ci$ was deposited on each specimen. The tracer concentration after diffusion annealing was followed through a penetration distance of $\sim 400\,\mu m$. The activity of the last section was still several times higher than the background count, and the total activity of the specimen was ~ 13 million counts per minute. The accuracy of counting low activity at deep penetration was improved by counting for long periods.

Riggs and Wuttig (108) observed no Na^+ grain boundary diffusion in NaCl at a diffusion temperature of 500 °C and a diffusion time of 32 hours, and in the absence of OH^- hydroxyl ions. It is possible that the negative result of Riggs and Wuttig is due to the overall depth of sectioning, only 50 μm, being too shallow. In the experimental Run 4 of the present work, which has a similar diffusion time and temperature, dislocation diffusion was not observable before a penetration distance of ∿60 μm.

Harris (57) observed a distinct tail in the grain boundary diffusion of Na^+ in a NaCl bicrystal at 360 °C. He attributed the enhanced diffusion to the phase change disorder of the segregated impurity precipitates along the boundaries. He concluded that enhanced diffusion in NaCl was only a boundary-associated effect, but the boundaries did not directly enhance the diffusion process. He supported his argument by showing the distribution of precipitates along the boundaries by light scattering method (52,53,55). It is reasonable to expect such an observation at low temperature. However, these precipitates should redissolve into the matrix, at a temperature of ∿360 °C. Thus, it is most unlikely that the enhanced diffusion Harris observed was a consequence of precipitation at the boundaries.

In the same work (57), Harris did observe a small tail in the diffusion profile of a single crystal, which became less discernable at longer diffusion times. He overlooked this 'substructure diffusion' and it is unfortunate that there is not enough information for this tail feature to be compared with the present work. The lattice diffusion coefficient determined by Harris was an order of magnitude larger than the corresponding value determined in this work.

Nevertheless, the diffusion profile started to deviate from the lattice diffusion-dominated region at a penetration distance $\sim 4(Dt)^{\frac{1}{2}}$, which is in agreement with the observations of the present work. A low counting efficiency is suggested by Harris' use of the solid powder scintillation method. With an improved detection sensitivity, and the use of a higher activity, following the tail to much deeper penetration distances may have been possible.

There are only two reports on the observation of dislocation-pipe diffusion in NaCl. Schlederer (112) reported a value $Q_d \sim 0.4$ eV and a corresponding lattice diffusion energy of $Q_v \sim 1.23$ eV in his diffusion studies of ultrapure NaCl in the extrinsic temperature range. Geguzin et al (42) observed fast transport of Na^+ down NaCl edge dislocations in the temperature range 200 - 540 °C. Using the Smoluchowski solution as well as Hart's model for the analysis of diffusion profiles in specimens of different dislocation density, Geguzin reported an activation energy for dislocation-pipe diffusion of $Q_d = 0.61$ eV. In their later diffusion work on NaCl bicrystals (43), they reported a similar value for the activation energy for grain boundary diffusion, $Q_b = 0.62$ eV. They suggested that the close resemblance of Q_d and Q_b implied that a similar vacancy mechanism was active for fast transport of Na^+ down the dislocations. It is unfortunate that the diffusion data in these reports is insufficient to enable a more critical comparison to be made with the present work. Recently Bielig (16), in his work of the recovery of internal friction in NaCl crystals of different purity, suggested that cation vacancies are the pinning points for dislocations, and that they could diffuse down the dislocations with an activation energy of 0.55 eV. The agreement of diffusion parameters (as shown in Table X) obtained in these independent investigations, on samples of different purities,

and containing different number of defects, should be regarded as an indication of the reliability of the results of the present work.

Table X. Comparison of the lattice and dislocation diffusion parameters of NaCl crystal

Q_v in eV	D_o in cm^2 sec^{-1}	Q_d in eV	D_{o_d} in cm^2 sec^{-1}	Reference
1.23	6×10^{-4}	0.4	-	Schlederer (112)
-	-	0.55	-	Bielig (16)
1.25±0.02	1.77×10^{-3}	0.57±0.04	5.35×10^{-12}	This work
-	-	0.61±0.03	7×10^{-12}	Geguzin et al (42)

All the diffusion profiles of the present work show distinct diffusion tails. Since the specimens used were single crystals, the evidence suggests that the tail features result from dislocation diffusion. This is further supported by the following observations.

a) The linear relationship of ln C versus penetration in the tail region, which is characteristic of dislocation diffusion;
b) gradients of the tails are not dependent on diffusion time;
c) extrapolation of the tail feature gives rise to a dislocation density of the specimen which is in agreement with observations from etch-pit micrographs.

The product value of $a^2 D_d \sim 10^{-15}$ to 10^{-16} cm^4 sec^{-1} is observed in the present diffusion temperature range. The extremely large value of $D_d \sim 10^{-2}$ cm^2 sec^{-1} is physically impossible if the radius of the dislocation path is assumed to be ~5 A°. Thus, the space-charge cloud must certainly contribute significantly to dislocation diffusion.

This is further supported by the evidence of a positive contribution of dislocations to conductivity. Since the space-charge cloud around a dislocation pipe is essentially a region of excess cation vacancies, it is realistic to suggest that the mechanism for the fast transport along the dislocation pipes is the jumping of the tracers into these vacancies. The fast transport of the tracers could also be aided by the easier passage through the internal voids of the dislocation cores. The extent of this contribution is not known. The overall mechanism for dislocation pipe diffusion in NaCl could be a combination of both.

Since the value D_d determined from experiments is always in the product a^2D_d, it is not possible to extract D_d explicitly without its independent measurement at some temperature. This can be achieved if the experimental condition satisfies the criterion $(Dt)^{\frac{1}{2}} < a$, when the tracer atoms are essentially trapped within the dislocation-pipes and diffusion corresponds to Harrison's (60) type C condition. The diffusion profile can then be analysed using the equation $C = Co\ \mathrm{erfc}[y(4D_dt)^{-\frac{1}{2}}]$ and D_d can be measured independently. Use of the equation assumes that a constant tracer concentration on the surface is maintained due to the short diffusion time. To maintain the condition $(Dt)^{\frac{1}{2}} < a$, the value a has to be large and D and t have to be small. At the lowest diffusion temperature used in the present work, i.e. 374 °C, if a is assumed to have the upper limit value of 10^{-4} cm, then t has to be less than 8 hours in order to observe type C diffusion and the total tracer penetration distance may be 20 - 30 μm. It has been shown in the previous chapter that sectioning becomes unreliable if the slices are less than 10 μm, and there is insufficient information in this short diffusion profile for a reliable determination

of the value D_d. With increasing diffusion temperature, and hence the value $(Dt)^{\frac{1}{2}}$, t has to decrease drastically to an even smaller value to satisfy type C condition. Such a short diffusion time is impractical, and no sensible results can be obtained. For practical purposes, this independent method of determining D_d can only be used effectively for very low values of lattice diffusion coefficient. In the diffusion temperature range of the present work, 374 °C - 505 °C, the use of such a method would be impossible.

CHAPTER SIX

CONCLUSIONS AND SUGGESTIONS FOR FURTHER WORK

The major problems experienced in applying the microtome sectioning technique were experimental, in particular the determination of section thickness. However, the technique was precise and efficient when the penetration of the tracer was sufficiently deep to allow optimum specimen thickness. The use of a more sensitive microbalance for weighing specimens of finer section would necessarily require a much longer acclimatisation time, and thus would limit the number of sections that could be cut in an assay. In the present work, specimens were sectioned to a thickness of $\sim$10 μm, and to a total penetration distance of $\sim$400 μm with a weighing error of $\sim$2.3%.

Polygonised arrays of dislocation in the four-point bend specimens were clearly revealed in the etch-pit micrographic studies of specimen surfaces. The inter-dislocation distance d was <10 μm or $\pi(Dt)^{\frac{1}{2}}$, and did not satisfy the condition for the dislocations to be isolated and independent in the tracer diffusion, i.e. $2(Dt)^{\frac{1}{2}} < d$. It was found that specimens from well annealed single crystals were more appropriate for the present study, having an average dislocation density $\sim 10^4$ cm^{-2}.

High purity NaCl crystals were grown, and subsequent spectroscopic analysis and conductivity measurements revealed that the divalent cation impurity content was $\sim$1 ppm.

Lattice diffusion coefficients in the extrinsic temperature range 374 °C - 505 °C were determined with an average error of $\sim$3%. The migration energy of cation vacancies H_m was (1.25 ± 0.02) eV. There is a suggestion that discrepancies in the H_m values quoted by previous

workers are a result of the differences in the purity of the materials used, even though there have been attempts to explain the discrepancies in terms of cation impurity-vacancy pairs or vacancy pairs. It would be worthwhile in any further work to conduct diffusion experiments using wider temperature range, and materials of different purity. This would enable an investigation of whether other migration mechanisms are contributing, by determining the formation energy of the defects that are acting during tracer transport in the intrinsic temperature range. In addition, such further work would support the suggestion that the migration energy changes with varying specimen purity.

The apparent migration energy of cation vacancy in NaCl determined from the extrinsic stage II of the conductivity plot was 0.71 eV and that for the short stage II' was 1.25 eV. There is evidence that in stage II there is a combination of lattice and dislocation contributions to conductivity. Haven ratios of 0.7815 and 0.65 were obtained for the lattice and dislocation contribution respectively, and thus the Nernst-Einstein equation is obeyed. A theoretical estimation showed that stage II' would be masked in specimens having a dislocation density $> 2 \times 10^4$ cm^{-2}. It will be most important for further work to study the change of conductivity of a well annealed and then deformed specimen of known dislocation density. An observed shift of stage II in the conductivity plot would support the present suggestion of a dislocation contribution to conductivity.

The tails in the diffusion profiles were found to be independent of diffusion time, a feature which is characteristic of isolated-dislocation diffusion. Extrapolation of the tails revealed a dislocation density 2 to 3 times smaller than that observed etch-pit micrographs.

The product value of a^2D_d for dislocation enhanced diffusion was between 10^{-15} to 10^{-16} cm^4 sec^{-1} in the present diffusion temperature range, and the activation energy was 0.57 ± 0.04 eV. There was evidence that the space-charge effect played an important role in the fast transport of the tracers down the dislocation paths. The calculated radius of the charge cloud was ∿260 A°. With a cloud of excess cation vacancies surrounding the dislocation-pipes, it is suggested that the fast transport of tracers is by jumping of the tracer into vacancies.

The value D_d may be measured independently in an experiment that satisfied Harrison's type C condition. Experimentally this could be achieved if specimens could be sectioned accurately to much thinner slices. If the use of other microsectioning techniques, such as chemical polishing or radio frequency sputtering, is applicable in NaCl crystal, it may then be possible to obtain D_d with more certainty, and use this value as an alternative to the product relationship of a^2D_d.

REFERENCES

1. Ahlborn K.
   Journal de Physique, Colloque C6. Supplement au No.6, 40, 185, (1979).

2. Allnatt A.R. and Chadwick A.V.
   Trans. Faraday Soc. 63, 1929, (1967).

3. Allnat A.R., Pantelis P. and Sime S.J.
   J. Phys. C: Solid State Phys. 4, 1778, (1971).

4. Amelinckx S.
   Acta. Metall. 2, 848, (1954).

5. Argarwal S.K. and Kulshreshtta A.P.
   Ind. J. Pure Appl. Phys., 5, 535 (1967).

6. Atkinson A. and Taylor R.I.
   Harwell AERE, R.9171, (July 1978).

7. Austin A.E. and Richards N.A.
   J. Appl. Phys. 32, 1462, (1961).

8. Austin A.E. and Richard N.A.
   J. Appl. Phys., 33, 3569, (1962).

9. Balluffi R.W.
   Phys. Stat. Sol., 42, 11, (1970)

10. Barr L.W., Hoodless I.M., Morrison J.A. and Rudham R.
Trans. Faraday Society, 56, 697, (1960).

11. Barr L.W. and Dawson D.K.
Phys. Rev. Lett. 19, 844, (1967).

12. Barr L.W. and Lidiard A.B.
~~Phys. Chem., 10, 151 (1970).~~ physical chemistry - An Advance Treatise eds. Eyring, Henderson, Jost

13. Béniere F. and Chemla M.
C.R. Acad. Sci., Paris, 266C, 660, (1968).

14. Béniere F., Béniere M. and Chemla M.
J. Chim. Phys. Physiochim Biol. 66, 5, 898, (1969).

15. Béniere F., Béniere M. and Chemla M.
J. Phys. Chem. Solids, 31, 1205, (1970).

16. Bielig G.A.
J. Phys. C: 14, L901, (1981).

17. Borisov V.T. and Lyubov B.Y.
Fiz. Metallov i. Metallovedenie 1, 298, (1955).

18. Borisov V.T., Golikov V.M., Lyubov B.Y. and Shtsherbendisky G.V.
Proc. Conf. on Radioisotopes in Scientific Research 1, 212, (1957).

19. Brebec G.
Rapport CEA-R2831, (1965), Saclay, France.

20. Brown N. and Hoodless I.M.

J. Phys. Chem. Solids, 28, 2297, (1967).

21. Bruneau A.A. and Pratt P.L.

Phil. Mag. 1, 1871, (1962).

22. Burgers J.M.

Proc. Phys. Soc. (London), A52, 23, (1940).

23. Butler C.T., Russe J.R., Quincy Jnr. R.B. and Lavalle D.E.

J. Chem. Phys., 45, 968, (1966).

24. Cabané J.

J. Chim. Phys., 59, 1123, (1962).

25. Cabané J.

J. Chim. Phys. 59, 1135, (1962).

26. Chemla M.

Ann. Phys. 1, 959, (1956).

27. Crawford J.H. and Slifkin L.M.

'Point Defects in Solids' Vol. 1, Plenum Press, N.Y. (1972).

28. Davidge R.W. and Whitworth R.W.

Phil. Mag., 6, 62, 217, (1961).

29. Davidge R.W.

Phys. Stat. Sol., 3, 1851, (1963).

30. Dawson D.K. and Barr L.W.
Proc. Brit. Ceram. Soc., 9, 171, (1967).

31. Downing H.L. and Friauf R.J.
J. Phys. Chem. Sol., 31, 845, (1970).

32. Dreyfus R.W. and Nowick A.S.
J. Appl. Phys. Suppl., 33, 473, (1962).

33. Economou N.A. and Sastry P.V.
Phys. Stat. Sol., 6, 135, (1964).

34. Eshelby J.D., Newey C.W.A., Pratt P.L. and Lidiard A.B.
Phyl. Mag., 3, 75, (1958).

35. Etzel H.W. and Maurer R.J.
J. Chem. Phys. 18, 8, 1003, (1950).

36. Etzel H.W. and Patterson D.A.
Phys. Rev., 1112, (1958).

37. Fisher J.C.
J. Appl. Phys., 22, 1, 74, (1951).

38. Frank F.C.
Phil. Mag., 42, 1014, (1951).

39. Fuschillo N., Gimpl M.L. and McMaster A.D.
J. Appl. Phys., 37, 2044, (1966).

40. Geguzin Y.Y., Kovalev G.N. and Ratner A.M.
Phys. Met. and Metallog. 10, 45, (1960).

41. Geguzin Y.Y. and Dobrovinskaya. E.R.
Soviet Phys., - Solid State, 7, 1660, (1966).

42. Geguzin Ya. E. and Dobrovinskaya E.R.
Soviet Phys., - Solid State, 7, 2826, (1966).

43. Geguzin Ya. E., Dobrovinskaya E.R., Lev. I.E. and Mozharov M.V.
Soviet Phys., - Solid State, 8, 2599, (1967).

44. Ghoshtagore R.N.
Phys. Rev., 155, 3, 589, (1967).

45. Ghoshtagore R.N.
Phys. Rev. 155, 3, 603, (1967).

46. Graham H.C., Tallan N.M. and Russel R.
J. Amer. Ceram. Soc., 50, 156, (1967).

47. Grno J. and Trnovcova V.
Phys. Stat. Sol., (a) 18, 303, (1973).

48. Guccoine R. and Tosi M.P.
J. Phys. Chem. Sol., 10, 162 (1959).

49. Guerrero A.L.
Ph.D. thesis, University of London, (1981).

50. Gupta D.

Phys. Rev., B7, 586, (1973).

51. Gupta D. and Tsui R.T.C.

Appl. Phys. Letters, 17, 294, (1970).

52. Harris L.B.

Appl. Phys. Lett. 13, 154, (1968).

53. Harris L.B. and Schlederer J.L.

Acta. Met. 19, 577, (1971).

54. Harris.L.B.

J. Crystal Growth, 24/25, 410, (1974).

55. Harris L.B. and Quang P.G.

Phil. Mag., 32, 1213, (1975).

56. Harris L.B.

J. Physique Colloq. 37, C7365, (1976).

57. Harris L.B. and Fiasson J.

Phys. Stat. Sol., (a) 33, 696, (1976).

58. Harris L.B.

J. Solid State Chem., 20, 245, (1977).

59. Harris L.B.

J. de Physique Colloq., supp. 7, 41, C6-285, (1980).

60. Harrison L.G.

Trans. Faraday Soc., 57, 1191, (1961).

61. Hart E.W.

Acta. Met., 5, 597, (1957).

62. Hendrickson A.A. and Machlin E.S.

Trans. A.I.M.E., 200, 1035, (1954).

63. Hobbs L.W.

J. Phys. E: Scientific Instruments 3, 85, (1970).

64. Hoodless I.M. and Thomson S.J.

Phil. Mag., 46, 1131, (1959).

65. Huddart A. and Whitworth R.W.

Phil. Mag., 27, 1, 107, (1973).

66. Hughes and Pooly.

J. Phys. C 6, 2094, (1973).

67. Hull D.

'Introduction to Dislocations' , (1968), Pergamon Press.

68. Jain S.C. and Dahake S.L.

Indian J. Pure.Appl. Phys., 2, 71, (1964).

69. Johnston W.G.

Phys. Rev., 98, 6, 1777, (1955).

70. Johnston W.G.

Progress in Ceramic Science 2, (1961).

71. Kanzaki H., Kido K., Tamura S. and Oki S.

J. Phys. Soc. Japan., 20, 2305, (1965).

72. Kingery W.D.

'Introduction to Ceramics', John Wiley & Sons, N.Y., (1976).

73. Kirk D.L. and Pratt P.L.

Proc. Brit. Ceram. Soc., 9, 215, (1967).

74. Kirk D.L., Phillips D.C. and Pratt P.L.

Proc. Brit. Ceram. Soc., 19, 105.

75. Kliewer K.L. and Koehler J.S.

Phys. Rev., A 140, 4, 1226, (1965).

76. Kliewer K.L. and Koehler J.S.

Ibid., 157, 685, (1967).

77. Klotsman S.M., Polikarpova I.P., Timofeev A.N. and Trakhtenberg I.Sh.

Soviet Physics - Solid State, 9, 1956, (1968).

78. Lai C.T. and Morrison H.M.

Canad. Jl. Physics 48, 1548, (1970).

79. Langmuir I.

J. Franklin Inst. 217, 543, (1934).

80. Laurent J.F. and Be'nard J.

J. Phys. Chem. Solids, 3, 7, (1957).

81. Laurent J.F. and Be'nard J.

J. Phys. Chem. Solids, 7, 218, (1958).

82. LeClaire A.D.

'Progress in Metal Physics' Vol.1, Chapter 7, (1948).

83. LeClaire A.D.

Phil. Mag., 42, 468, (1951).

84. LeClaire A.D.

Progr. Met. Phys., Vol.4, London, Pergamon Press Ltd (1953).

85. LeClaire A.D.

Brit. J. Appl. Phys., 14, 351, (1963).

86. LeClaire A.D. and Rabinovitch A.

Harwell Publication R10195, (1981) A.E.R.E. Harwell U.K.

87. Lehovec K.

J. Chem. Phys., 21, 1123, (1953).

88. Levine H.S. and MacCallum C.J.

J. Appl. Phys. 31, 595, (1960).

89. Lidiard A.B.

Phys. Rev., 94, 1, 29, (1954).

90. Mapother D., Crooks H.N. and Maurer R.
J. Chem. Phys. 18, 1231, (1950).

91. Mimkes J. and Wuttig M.
J. Appl. Phys., 41, 3205, (1970).

92. Mimkes J. and Wuttig M.
Phys. Rev. B 2, 1619, (1970).

93. Mimkes J.
Phys. Stat. Sol., (b) 58, K31, (1973).

94. Mimkes J.
Thin Solid Films, 25, 221, (1975).

95. Mimkes J.
Journal de Physique, Colloque C6. Supplement au No.6, Tome 40, 181 , (1979).

96. Mistler R.E. and Coble R.L.
J. Appl. Phys., 45, 1507, (1974).

97. Mitchell J.L. and Lazarus D.
Phys. Rev. B 12, 734, (1975).

98. Mizuno H. and Inoue M.
Phys. Rev., 120, 1226, (1960).

99. Moment R.L. and Gordon R.B.
J. Appl. Phys. 35, 2489, (1964).

100. Montel M.E.

J. Phys. Rad. 10, 78, (1929).

101. Mott N.F.

Proc. Phys. Soc. (London), 60, 391, (1948).

102. Nelson V.C. and Friauf R.J.

J. Phys. Chem. Sol., 31, 825, (1970).

103. Pavlov P.V., Panteleev, V.A. and Maiorov A.V.

Soviet Physics - Solid State, 6, 2, 305, (1964).

104. Pratt P.L., Roy C. and Evans A.G.

Material Science Research, Vol. 3, Plenum Press (1966).

105. Quin J., Redfern B.A.W. and Pratt P.L.

Proc. Brit. Ceram. Soc., 9, 35, (1967).

106. Read W.T.

'Dislocations in Crystals', McGraw Hill, London, (1953).

107. Reisfeld R. and Fredericks W.J.

Israel J. Chem. 8, 959, (1970).

108. Riggs K.R. and Wuttig M.

J. Appl. Phys. 40, 4682, (1969).

109. Riggs K.R.

Ph.D. thesis, University of Missouri-Rolla, U.S.A. (1970).

110. Rothman S.J., Barr L.W., Rowe A.H. and Selwood P.G.

Phil. Mag., 14, 501, (1966).

111. Rothman S.J., Peterson N.L., Laskar A.L. and Robinson L.C.
J. Phys. Chem. Solids, 33, 1061, (1972).

112. Schlederer L.J.
Ph.D. thesis, University of New South Wales, Australia (1974).

113. Shirn G.A., Wajda E.S. and Huntington H.B.
Acta. Met. 1, 513, (1953).

114. Smoluchowski R.
'Imperfections in Nearly Perfect Crystals', John Wiley & Son, Inc., N.Y. 451, (1952).

115. Smoluchowski R.
Phys. Rev. 87, 482, (1952).

116. Spencer O.S. and Plint C.A.
J. Appl. Phys., 40, 168, (1969).

117. Springer E.
Zeit. f. Metallk. 62, 298, (1971).

118. Stark J.P.
J1. Appd. Phys. 36, 3938, (1965).

119. Stark J.P. and Upthegrove W.R.
Trans. Amer. Soc. Metals., 59, 479, (1966).

120. Stokes R.J., Johnston T.L. and Li C.H.
Trans. AIME, 218, 655, (1960).

121. Suzuóka T.

J. Phys. Soc. Japan, 19, 6, 839, (1964).

122. Tucker P., Laskar A. and Thomson R.

J. Appl. Phys. 34, 445, (1963).

123. Turnbull D. and Hoffman R.E.

Acta. Met. 2, 419, (1954).

124. Upthegrove W.R. and Sinnott M.J.

Trans. Amer. Soc. Metal., 50, 1031, (1958).

125. Vogel F.L., Pfann W.G., Corey H.E. and Thomas E.E.

Phys. Rev., 90, 489, (1953).

126. 'Watts Microptic- Auto-Collimator Catalogue'.

Hilger and Watts Limited.

127. Wei G.C.T. and Wuensch B.J.

J. Amer. Ceram. Soc., 59, 7-8, 296, (1976).

128. Whipple R.T.P.

Phil. Mag., 45, 1225, (1954).

129. Whitworth R.W.

Advances in Physics, 24, 2, 203, (1975).

130. Williams G.P. and Slifkin L.

Phys. Rev. Letters, 1, 243, (1958).

131. Wuensch J. and Vasilo T.

J. Amer. Ceram. Soc., 47, 63, (1964).

132. Wuensch B.J. and Vasilo T.

Office of Naval Research, Report No. NONR 4267(00).

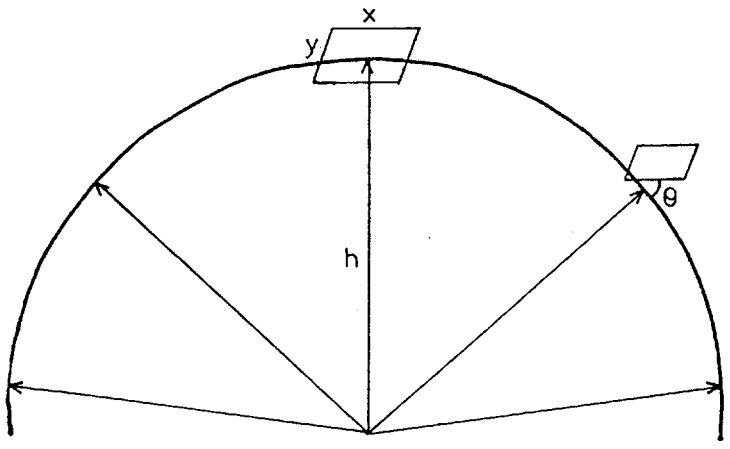
133. Yan.M.F., Cannon R.M., Bowen H.K. and Coble R.L.

J. Amer. Ceram. Soc., 60, 120, (1977).

134. Yukawa S. and Sinnott M.J.

J. Metals, 7, 996, (1955).

APPENDIX I: Theoretical Calculation of the Efficiency of the Vacuum Evaporation Technique in Relation to the Geometry of the Source and the Specimen.



In the upward vacuum evaporation technique, the density of the source per unit area of the half sphere of radius $\hat{s}$, assuming 100% evaporation is given by $\rho = C/2\pi\hat{s}^2$. The amount of source deposited on a surface area of xy at a distance h is a function of x, y, h and the angle θ .

$$\text{i.e. Intensity} = \iint \rho \cos\theta \, dx dy$$

$$= \frac{C}{2\pi} \iint \frac{dx\, dy \cos\theta}{x^2 + y^2 + h^2}$$

$$= \frac{C}{2\pi} \iint \frac{dx\, dy}{(x^2 + y^2 + h^2)} \cdot \frac{h}{(x^2 + y^2 + h^2)^{\frac{1}{2}}}$$

Solution of the double intergrals in the equation above is a complicated procedure. If h is small and $\cos\theta = 1$, it is reasonable to estimate the amount of source deposited on an area xy,

vertically above the source, using $Cxy/2\pi h^2$.

Therefore, an estimate of the efficiency of evaporation is given by:-

$$\frac{Cxy}{2\pi h^2} \; / \; C \times 100\%$$

and the results of these estimates as a function of area and vertical distance are tabulated below.

Area xy in cm^2 vertical distance in cm	0.7^2	0.8^2	0.9^2	1.0^2
0.7	15.9	20.8	23.6	32.5
0.8	12.2	15.9	20.1	24.9
0.9	9.6	12.6	15.9	19.7
1.0	7.8	10.2	12.9	15.9

APPENDIX II : Calibration of Radioactivity Counting Efficiency

The radioactivity concentration of the $Na^{22}Cl$ source is 100μCi per 500μl and 1μCi = 2.22×10^6 counts per minute.

5μl of the source was syringed separately into the scintillation vials A, B, C and D, each containing 0.5ml of distilled water. 10ml of the liquid scintillation Unisolve 294 was pipetted into each of the four vials and shaken for 15 seconds. Each sample, A-D was

counted in the scintillation counter 5 times. for 2 minutes each The mean counts per minute are listed below.

Sample		Counts per minute
A	:	1.594×10^6
B	:	1.614×10^6
C	:	1.607×10^6
D	:	1.617×10^6

Therefore, mean counts for a 5µl source was 1.608×10^6 cpm.

Therefore, counting efficiency of the liquid scintillator Unisolve 294 in NaCl

$$= \frac{1.608}{2.22} \times \frac{10^6}{10^6} \times 100\%$$

$$= 72.4\%$$

APPENDIX III : Calibration of the Microtome

Theoretical Increments (µm)	Dial-Gauge Readings (µm)
10	9.0
20	19.0
30	30.0
40	41.0
50	52.6
60	63.2
70	73.6

80	85.0
90	96.4
100	107.2
110	118.8
120	129.6
130	139.8
140	150.8
150	161.4
160	170.8
170	180.2
180	191.4
190	201.6
200	211.8
210	211.8
220	231.4
230	240.2
240	248.6
250	258.0
260	266.2
270	274.4
280	282.2
290	291.2
300	300.2
310	310.0
320	319.6
330	329.4
340	338.4
350	348.2

360	357.4
370	366.6
380	376.2
390	386.2
400	396.8

APPENDIX IV : The Determination of Tracer Layer Thickness on the Specimen Surface.

The total amount of radioactivity detected in a specimen of $1cm^2$ was ~ 1.3×10^7 cpm.

The counting efficiency of the tracer is 72.4%. Thus, the actual amount of radioactivity on the surface of the specimen before diffusion

$$= 1.3 \times 10^7 \times \frac{100}{72.4} \text{ cpm}$$

$$= 1.8 \times 10^7 \text{ cpm}$$

The specific activity of the tracer solution is 200μCi/ml.

The equivalent amount of the tracer solution that corresponds to the above activity

$$= 1.8 \times 10^7/(200 \times 2.22 \times 10^6)\text{ml}$$

$$= 4.05 \times 10^{-2}\text{ml}$$

The concentration of Na^{22} is 0.70 mg/ml. Therefore the weight of

Na^{22} in the tracer layer

$$= 4.05 \times 10^{-2} \times 0.7\text{mg}$$

$$= 2.84 \times 10^{-5} \text{ gm}$$

and the weight of the $Na^{22}Cl$ tracer layer

$$= 2.84 \times 10^{-5} \text{ gm} \times (35.45 + 22)/22$$

$$= 7.41 \times 10^{-5} \text{ gm}$$

The density of NaCl is 2.165 gm/cc.

The distribution of the $Na^{22}Cl$ tracer on the surface of the specimen during evaporation is assumed to be even. Thus, the thickness of the tracer layer on the surface of the specimen

$$= 7.41 \times 10^{-5}/2.165 \text{ cm}$$

$$= 3.42 \times 10^{-5} \text{ cm}$$

$$= 0.34 \ \mu\text{m}$$

APPENDIX V : Conductivity Data

$\text{Log}_{10}\sigma T$ ($\text{ohm}^{-1}\cdot\text{cm}^{-1}\cdot\text{K}$)	$1000/T\ \text{K}^{-1}$
-1.1965	1.0460
-1.3092	1.0582
-1.5423	1.0776
-1.6600	1.0905
-1.8224	1.1099
-1.9589	1.1248
-2.0457	1.1313
-2.2455	1.1547
-2.4203	1.1723
-2.5599	1.1876
-2.7162	1.2121
-2.7665	1.2180
-2.8961	1.2407
-3.0346	1.2626
-3.1736	1.2690
-3.3226	1.3158
-3.4120	1.3441
-3.4800	1.3587
-3.5343	1.3774
-3.6336	1.4045
-3.7289	1.4265
-3.7684	1.4451
-3.8524	1.4641
-3.9425	1.4848

-4.0163	1.5049
-4.0675	1.5267
-4.2019	1.5601
-4.3557	1.5898

APPENDIX VI : Diffusion Data for Experimental Runs 1-5

Run : 1

Temperature : 374 $\pm$ 1°C

Time : 3.7098×10^6 seconds.

Ln C/Co	Penetration (μm)
-3.17	18.5
-4.07	27.8
-5.41	37.6
-6.85	46.0
-8.48	56.3
-9.24	65.6
-9.57	74.9
-9.81	85.1
-9.97	95.4
-10.08	105.5
-10.16	114.9
-10.27	124.0
-10.27	134.3
-10.36	145.2
-10.43	155.8

-10.48	165.6
-10.55	175.6
-10.53	184.1
-10.55	195.0
-10.62	205.2
-10.58	213.3
-10.62	224.4
-10.64	233.0
-10.70	243.7
-10.71	253.0
-10.77	263.3
-10.75	272.8
-10.80	282.9
-10.85	293.2
-10.83	303.5
-10.93	313.5
-10.84	323.1
-10.93	332.3
-10.92	341.6
-10.94	352.3
-11.06	361.9
-11.05	371.3
-11.14	382.3
-11.11	391.1
-11.10	400.0

Run : 2

Temperature 414 ± 1°C

Time : 1.116 x 10^6 seconds

Ln C/Co	Penetration (μm)
-3.16	19.9
-4.96	27.3
-6.45	46.9
-7.66	56.0
-8.39	65.2
-8.74	76.2
-8.99	86.4
-9.21	96.3
-9.34	105.7
-9.51	116.4
-9.67	125.9
-9.79	136.4
-9.88	146.3
-9.94	155.0
-9.99	164.8
-10.04	174.1
-10.07	183.2
-10.13	194.6
-10.18	204.9
-10.24	214.9
-10.17	223.1
-10.27	233.1
-10.33	241.8

-10.38	251.8
-10.36	259.7
-10.41	269.2
-10.41	280.0
-10.43	290.2
-10.53	299.2
-10.53	310.4
-10.59	321.1
-10.64	331.3
-10.66	340.7
-10.72	350.8
-10.78	361.2
-10.78	371.1
-10.81	383.0
-10.86	391.2
-10.89	400.3
-10.97	409.5

Run : 3

Temperature : 449 ± 1°C

Time : 5.994×10^5 seconds

Ln C/Co	Penetration (μm)
-3.17	8.2
-3.29	13.9
-3.67	20.0
-3.93	26.9
-4.45	32.4
-4.99	38.5
-5.65	44.3
-6.13	48.8
-6.90	54.8
-7.79	61.0
-8.20	67.3
-8.62	73.1
-8.93	79.1
-9.18	87.0
-9.34	92.5
-9.50	98.1
-9.66	104.1
-9.75	108.8
-9.88	114.3
-9.97	121.0
-10.06	127.3
-10.21	132.8

-10.25	138.9
-10.34	145.1
-10.43	151.0
-10.46	158.2
-10.47	164.8
-10.56	170.2
-10.56	176.2
-10.60	181.3
-10.61	187.0
-10.62	193.2
-10.65	200.3

Run : 4

Temperature : 505 ± 1°C

Time : 8.28×10^4 seconds.

Ln C/Co	Penetration (μm)
-2.84	13.2
-4.60	31.8
-6.19	42.2
-7.02	52.0
-7.84	61.6
-8.56	71.1
-9.10	81.7
-9.46	90.8
-9.84	100.9
-10.09	110.7
-10.30	120.5
-10.42	130.1
-10.48	138.6
-10.64	147.7
-10.09	156.5
-10.81	165.7
-10.91	175.4
-10.97	184.3
-10.06	194.6
-10.16	204.4
-11.25	215.3
-11.23	223.2

-11.39	234.7
-11.47	243.8
-11.50	253.4
-11.59	263.3
-11.59	272.0
-11.68	280.8
-11.81	290.8
-11.86	300.6
-11.92	311.2
-12.07	322.2
-12.11	332.7
-12.17	341.8
-12.26	353.1
-12.39	363.7
-12.44	375.5
-12.50	384.5
-12.55	393.6
-12.64	403.1

Run : 5

Temperature : 506 ± 1°C

Time : 1.98×10^4 seconds

Ln C/Co	Penetration (μm)
-2.15	6.7
-3.71	15.0
-6.62	25.1
-9.29	34.2
-10.26	44.3
-10.67	53.8
-10.93	62.8
-11.10	72.4
-11.27	81.9
-11.32	90.4
-11.41	101.5
-11.45	110.9
-11.55	120.7
-11.70	130.7
-11.73	143.3
-11.81	151.4
-11.94	161.5
-12.02	170.6
-12.04	180.7
-12.17	190.8
-12.26	201.3

-12.24	210.1
-12.38	220.8
-12.45	229.9
-12.57	239.1
-12.66	249.6
-12.69	259.3
-12.77	269.0
-12.93	280.5
-12.94	289.5
-13.11	299.6
-13.19	309.0
-13.13	318.8